TRIBHUVAN UNIVERSITY
INSTITUTE OF ENGINEERING
PULCHOWK CAMPUS

NUMERICAL SIMULATION OF HYPERSONIC FLUID-THERMAL-STRUCTURE INTERACTION ON A CLAMPED THIN PANEL

By:
Bikash Kumar Jaiswal (078BAS014)
Kripsan Shrestha (078BAS023)
Krishna Prasad Sah Sudi (078BAS024)
Yashaswi Shrestha (078BAS045)

A PROJECT REPORT SUBMITTED TO THE DEPARTMENT OF MECHANICAL AND AEROSPACE ENGINEERING IN PARTIAL FULFILLMENT OF THE REQUIREMENTS FOR THE DEGREE OF BACHELOR OF AEROSPACE ENGINEERING

DEPARTMENT OF MECHANICAL AND AEROSPACE ENGINEERING
LALITPUR, NEPAL

March, 2026

COPYRIGHT

LETTER OF APPROVAL

TRIBHUVAN UNIVERSITY

INSTITUTE OF ENGINEERING

PULCHOWK CAMPUS

DEPARTMENT OF MECHANICAL AND AEROSPACE ENGINEERING

The undersigned certify that they have read and recommended to the Institute of Engineering for acceptance, a project report entitled " Numerical Simulation of Hypersonic Fluid-Thermal-Structural-Interaction on a Clamped Thin Panel" submitted by Bikash Kumar Jaiswal, Kripsan Shrestha, Krishna Prasad Sah Sudi and Yashaswi Shrestha in partial fulfillment of the requirements for the Degree of Bachelor in Aerospace Engineering.

Supervisor Asst. Prof Sudip Bhattrai

Head of Department

Department of Mechanical and Aerospace Engineering

Supervisor Asst. Prof Durga Bastakoti

Department of Mechanical and Aerospace Engineering

External Examiner, Sandip Gewali

Department of Mechanical and Aerospace Engineering

Date: 2083/02/13

ABSTRACT

Structures operating under hypersonic flow conditions experience severe aerodynamic and thermal loads due to strong shock waves and rapid heat transfer. These effects lead to coupled interactions between fluid forces, thermal fields and structural deformation, commonly referred to as Fluid Thermal Structural Interaction (FTSI). Thin structural components such as panels are particularly vulnerable to these conditions, often undergoing large deflections, dynamic instabilities and changes in material behaviour under sustained loading. In hypersonic regimes, the combined influence of pressure and temperature gradients significantly affects the structural response, making it important to accurately predict the behaviour of such systems for reliable design. This study presents a numerical investigation of the FTSI behaviour of a clamped thin panel by extending the NASA RC-19 benchmark configuration to hypersonic environment. The primary objective is to analyse the coupled aerothermal and structural response of the panel and to evaluate its dynamic characteristics under combined aerodynamic pressure and thermal loading. Two modelling approaches are implemented to capture the system behaviour. A low fidelity model based on piston theory as well as CFD enriched PT is used for simplified analysis, while a high fidelity model is developed using OpenFOAM and CalculiX, coupled through the preCICE library to enable two way interaction between fluid and structural domains. The comparison between these approaches allows assessment of accuracy and computational efficiency. The simulations capture shock induced pressure loading and transient thermal gradients, enabling evaluation of deformation, thermal stresses and flutter like response of the panel. The findings provide insight into the aerothermoelastic behaviour of hypersonic structures and support the development of improved predictive models for high speed aerospace applications. A systematic parametric study was performed by progressively reducing the plate thickness from 12 mm to 5 mm and finally to 3 mm. Key results show that decreasing the plate thickness significantly amplifies the structural response. The maximum mid-point displacement increased from a negligible 34 μm for the 12 mm plate, 0.38 mm for 5 mm thick plate to approximately 1.75 mm for the 3 mm plate. The separation and reattachment points of the flow were found to oscillate at 119.21 Hz, which closely matches the frequency of the displacement vs time of the plate , indicating strong frequency lock-in and synchronized fluid-structure interaction. Furthermore, a clear correlation was observed between panel displacement and wall heat flux, with heat flux increasing sharply as panel deformation grew, demonstrating significant aero-thermal feedback.

Keywords: Aerothermoelasticity, CalculiX, Clamped Panel, FTSI, Hypersonic Flow, OpenFOAM, preCICE, RC-19, Thermal Loads

ACKNOWLEDGEMENT

Foremost, we would like to express our sincere gratitude to our supervisors, Dr. Sudip Bhattarai and Dr. Durga Bastakoti, for their continuous guidance, insightful suggestions, and unwavering support throughout the course of this project. Their mentorship played a crucial role in shaping our approach and strengthening the quality of our work.

We would also like to acknowledge the contributions of previous researchers, particularly the work associated with the NASA RC-19 benchmark case and studies on fluid-thermal-structure interaction (FTSI), which served as a fundamental reference for the development and validation of our numerical model.

We are deeply grateful to the Department of Mechanical and Aerospace Engineering, Pulchowk Campus, Institute of Engineering for providing us with the opportunity and necessary resources to undertake this project. This experience has allowed us to effectively apply the knowledge gained throughout our academic journey to a complex and practical engineering problem.

We would like to extend our appreciation to Er. Sandip Gewali and Er. Nishchal Poudel for their guidance and support during various phases of this project.

We are also thankful to our friends and classmates for their encouragement and support, both directly and indirectly.

Finally, we would like to express our heartfelt gratitude to our families for their constant support, patience, and motivation throughout this journey.

We welcome any suggestions or constructive feedback that may contribute to the improvement of this work.

Authors: Bikash Kumar Jaiswal (078BAS014)
Kripsan Shrestha (078BAS023)
Krishna Prasad Sah (078BAS024)
Yashaswi Shrestha (078BAS045)

TABLE OF CONTENTS

LIST OF FIGURES

LIST OF TABLES

LIST OF ABBREVIATIONS

AePW	Aeroelastic Prediction Workshop
CFD	Computational Fluid Dynamics
FEA	Finite Element Analysis
FSI	Fluid-Structure Interaction
FTSI	Fluid-Thermal-Structure Interaction
HFM	High Fidelity Model
LFM	Low Fidelity Model
MATLAB	Matrix Laboratory
OpenFOAM	Open-source Field Operation and Manipulation
preCICE	Precise Code Interaction Coupling Environment
PSP	Pressure Sensitive Paint
SBLI	Shock-Boundary Layer Interaction

LIST OF SYMBOLS

M	Mach number
ρ	Density of the fluid
u, v, w	Velocity components in Cartesian coordinates
T	Absolute temperature
P	Static pressure
q	Heat flux
κ	Thermal conductivity
E	Young's modulus of the panel material
ν	Poisson's ratio
σ	Mechanical stress
α	Coefficient of thermal expansion
t	Time
δ	Boundary layer thickness

CHAPTER ONE: INTRODUCTION

1.1 Background

Hypersonic vehicles, which travel at speeds beyond Mach 5, operate in some of the harshest and most complex environments in aerospace engineering. These conditions expose the vehicle to intense aerodynamic forces and rapid thermal loading, leading to tightly coupled interactions between the fluid, thermal, and structural domains [3]. Accurately modeling these interactions is crucial to maintaining the structural integrity and performance of critical vehicle components. To capture these effects, the study of Fluid Thermal Structure Interaction (FTSI) offers a powerful multidisciplinary approach. Unlike traditional decoupled or sequential methods, FTSI solves the flow field, thermal loading, and structural deformation in a fully integrated manner [4]. This is particularly important in hypersonic regimes, where shock waves, boundary layer interactions, and steep thermal gradients generate rapidly evolving, localized stress fields [5]. Structural components such as leading edges, nose cones, control surfaces, and thin panels are especially vulnerable in these environments. For instance, localized heating due to shock boundary layer interactions (SBLI) can cause severe thermal expansion, material degradation, and structural instabilities like flutter or buckling, ultimately affecting the vehicle's performance and safety [6]. In this work, we focus on a clamped thin panel subjected to hypersonic flow and steep thermal gradients representing a simplified but meaningful test case to understand the coupled FTSI response. Moreover, high temperatures in hypersonic environments lead to significant changes in material behavior. Properties like the elastic modulus often degrade with temperature, and effects such as thermal creep reduce the load bearing capacity and stiffness of structural elements [7]. These temperature dependent nonlinearities introduce additional complexity, making the structural response highly sensitive to both spatial and temporal variations in heat flux and aerodynamic pressure. While many past studies have used decoupled or one-way coupled methods, these approaches often overlook the mutual feedback mechanisms inherent in true FTSI problems. A strongly coupled model allows real-time interaction between the flow, temperature field, and structural deformation. Even small deflections in the structure can alter local aerodynamic loading and heat transfer behavior, making accurate predictions impossible without accounting for this feedback loop [8]. The goal of this research is to numerically simulate the hypersonic FTSI interaction on a clamped thin panel, revealing how coupled aerodynamic and thermal effects influence structural dynamics [9]. By studying this interaction in a controlled and simplified configuration, we aim to extract insights that can guide the design of more resilient thermal protection systems for future hypersonic vehicles. Ultimately, strongly coupled FTSI modeling is not just an advanced tool . It is essential for next generation hypersonic design. By capturing the full spectrum of interactions in real time, these simulations enable more accurate predictions of failure modes, support the development of robust thermal protection strategies, and help ensure safe and efficient performance in extreme flight [10, 11].The figure1.1 shows how the nacelle's bow shock hits the bottom of the vehicle, leading to a concentrated area of intense heating, while the remaining shocks are diverted and have a much smaller effect.

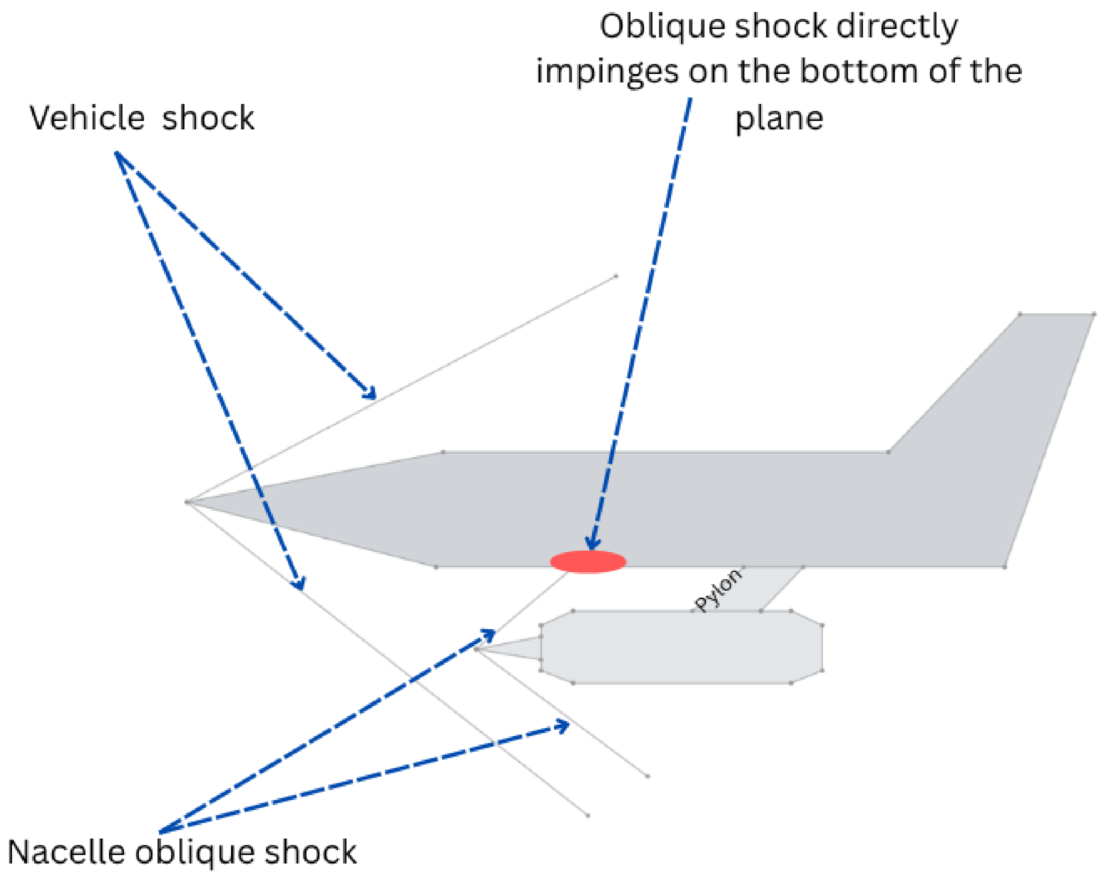

Figure 1.1: Example of Shock Impingement on body of aircraft

1.2 Problem statement

Understanding the structural response under hypersonic conditions is challenging due to the coupled interaction of aerodynamic forces, thermal effects, and structural deformation, commonly referred to as Fluid–Thermal–Structure Interaction (FTSI) [3]. Although experimental investigations provide valuable insights, they are often expensive and limited in scope [12]. Consequently, numerical simulations offer a more flexible and cost effective alternative for studying such complex phenomena [10]. This study builds upon NASA's RC-19 benchmark case from the AePW-4 workshop [4], which considers a thin panel clamped along all edges and exposed to high speed flow. The original benchmark primarily focused on supersonic conditions to investigate FTSI behavior, aiming to predict material properties and structural thickness requirements for high speed vehicles [?]. However, it does not sufficiently address hypersonic regimes, where thermal effects and material degradation become significantly more pronounced. The dynamic response of the panel, induced by pressure loads and shock interactions in both supersonic and hypersonic flows, provides critical insight into FTSI characteristics [8]. Therefore, this research extends the benchmark to hypersonic conditions by varying key parameters such as Mach number, wall temperature, material properties, panel thickness, panel length, and computational domain width. The objective is to evaluate their influence on aerothermoelastic performance [5]. To achieve this, two modeling approaches are employed: a Low-Fidelity Model (LFM) for rapid analysis with minimal computational resources [13], and a High-Fidelity Model (HFM) utilizing OpenFOAM, CalculiX, and preCICE for detailed coupled simulations [14]. By validating both models against RC-19 experimental data [12], this study aims to establish a balance between computational cost and accuracy, ensuring that simulation errors remain within an acceptable limit (ε). The findings are expected to contribute to the development of reliable simulation frameworks for hypersonic vehicle structural design.

1.3 Objectives

To study hypersonic FTSI behavior of a clamped thin panel using numerical simulations.

1.3.1 Main Objective

The main objective of this study is to use numerical simulations to investigate the behavior of a clamped thin panel subjected to combined aerodynamic loads and intense thermal effects under hypersonic conditions, with an emphasis on fluid-thermal-structural interactions.

1.3.2 Specific Objectives

i. To validate the RC-19 benchmark case under supersonic conditions and extend to hypersonic flow regime

ii. To develop a coupled Low Fidelity Modeling (LFM) approach incorporating Euler Bernoulli beam FEM, piston theory, and shock expansion theory to predict fluid-structure interaction

iii. To investigate the coupled transient behaviour of wall heat flux, structural deformation, and separation bubble dynamics through High-Fidelity FTSI simulations using URANS, CalculiX, and preCICE.

1.4 System Requirements

To successfully perform the numerical simulations, both hardware and software resources are equally important, as described in this section.

1.4.1 Hardware Requirements

The simulations carried out in this study involve coupled fluid–thermal–structural analysis, which is computationally intensive. To ensure efficient execution and reasonable simulation time, a system with adequate processing power, memory, and storage was required. The recommended hardware configuration used in this work is summarized in Table 1.1. A multi-core processor (32 cores) was utilized to handle parallel computations, particularly for CFD simulations. A minimum of 32 GB RAM was necessary to manage large mesh sizes and data exchange between solvers. Solid-state storage (512 GB SSD or higher) ensured faster read/write operations, which is crucial for handling large simulation datasets. Although not mandatory, a GPU was recommended to accelerate post-processing and improve visualization performance.

Table 1.1: Recommended Hardware for Hypersonic FTSI Simulations

Component	**Specification**
CPU	32-core processor
RAM	Minimum 32 GB
Storage	512 GB SSD
Harddisk	1TB

1.4.2 Software Requirements

A combination of open-source and commercial software tools was used to perform the simulations, modeling, and post-processing tasks. Each software played a specific role in the overall Fluid–Thermal–Structure Interaction (FTSI) framework. The complete software stack is listed in Table 1.2. OpenFOAM was used as the CFD solver to compute the fluid flow and thermal fields. CalculiX served as the structural solver to evaluate deformation and stress in the panel. The coupling between fluid and structural domains was achieved using preCICE, which enables efficient data exchange between solvers. Gmsh was employed for generating computational meshes for both fluid and solid domains. MATLAB was used to develop low-fidelity models, implement piston theory, and perform data analysis and post-processing. ParaView was utilized for visualization of flow fields, pressure distribution, and structural deformation. Additionally, Canva was used to create high-quality figures and graphical illustrations for documentation purposes.

Table 1.2: Software Stack for FTSI-Based Aerothermoelastic Modeling

Software	**Purpose**
OpenFOAM	Used to solve the fluid flow governing equations
CalculiX	Used to simulate the structural response of the solid panel
preCICE	Couples fluid and solid solvers for data exchange
Gmsh	Used to generate meshes for fluid and solid domains
MATLAB	Used for developing low-fidelity and post-processing models
ParaView	Used for visualization and analysis of simulation results
Inkscape	Used for vector graphics and figure preparation

CHAPTER TWO: LITERATURE REVIEW

In recent years, studying how fluid, heat, and structure interact at hypersonic speeds has become increasingly important. When vehicles travel faster than Mach 5, their thin panels are exposed to strong shock waves and intense thermal loads, which can cause bending, vibration, or even structural failure. Early research used simplified models to predict the onset of panel flutter under these extreme conditions [3], but such models fail to capture critical effects such as shock-boundary layer interactions and temperature-induced material softening. To overcome these limitations, recent studies employ high-fidelity methods that fully couple fluid dynamics, heat transfer, and structural response [10]. Numerous investigations have demonstrated the effectiveness of strongly coupled simulations. For example, one study evaluated a flexible panel subjected to Mach 5.8 flow using both low- and high-fidelity models [4]. The advanced simulations provided more accurate predictions of flutter and thermally driven deformations compared to older methods. Another study emphasized that thermal effects can cause panels to bend slowly due to material softening, a phenomenon often overlooked in simpler models [9]. These findings highlight the importance of accounting for the combined thermal and structural interactions. Experimental testing remains essential for validating computational models. Benchmark studies such as the NASA RC-19 experiment and the ASCEND wind tunnel tests have played a key role. In one experiment, a clamped panel was tested, and the measured vibration modes and frequencies closely matched simulation results [12]. Another investigation of panel flutter at Mach 6 revealed that thermal and gas dynamic effects significantly influence vibration characteristics, underscoring the need to incorporate these effects in numerical models [5]. More recent advancements have included air chemistry and improved turbulence models. For example, a study used a chemically reacting flow model coupled with structural interaction to study panel vibrations [8]. Another performed detailed 3D simulations of vortex-induced vibration using open-source tools and advanced coupling frameworks like preCICE [14]. Additionally, few studies in the literature showed that certain coupling strategies can drastically reduce computational cost while maintaining acceptable accuracy, making them attractive for preliminary design studies[4].
Early studies laid the foundation by examining rigid panels under shock impingement, highlighting the formation of a separation bubble, reattachment shocks and elevated local heat transfer. Willems et al. (2011) [15] conducted supersonic experiments on a flexible wall and demonstrated that even small panel deflections noticeably distort the impinging shock and modify the separation zone size. More recent experimental campaigns in short-duration hypersonic facilities (Currao et al., 2018[16]; Daub et al., 2022[17]) confirmed that compliant panels exhibit self-sustained oscillations when subjected to shock impingement, with deformation amplitudes large enough to shift the shock foot and alter the reattachment location. Despite these developments, challenges remain. Phenomena such as thermal creep

and nonlinear structural behavior are still difficult to model accurately and require further investigation.
Thermal effects further intensify the coupling. Aerodynamic heating degrades material stiffness (temperature-dependent Young's modulus) and induces thermal expansion, both of which lower the flutter boundary and increase deformation. Recent aerothermoelastic frameworks [18];[19]) highlight that two-way thermal coupling is essential for accurate prediction of long-term panel response in hypersonic environments.

2.1 Shock-Wave Boundary Layer Interaction

Shock-Wave Boundary Layer Interaction has been the focus of numerous studies for several decades as understanding SWBLI and its effects is crucial for hypersonic vehicle design. One such effect is the localized aerodynamic heating which increases with increasing Mach number that can be extremely severe [20]: one such example was seen on one of the final flights of the X-15 hypersonic vehicle in the 1960s[21]. Another serious problem in high-speed flights is the intake unstart. This problem was encountered in the Boeing X-51 scramjet during a powered flight test in 2011, also resulting in the loss of the vehicle[22]. SWBLI, being one of the contributing factors for engine unstart, must be studied and analyzed during supersonic and hypersonic intake and engine design [23]. External shock impingement into the body and flow through a compression ramp are the two most common cases used to study SWBLI in literature. [24] experimentally studied hypersonic shock-wave boundary layer interaction in hypersonic flow at freestream Mach numbers from 6.5 to 13, with Reynolds number ranging from $1*10^7$ to $1*10^8$, at the wall to freestream stagnation temperature from 0.1 to 0.4. The separated region was induced in two ways: through external oblique shockwave impingement and through compression surface. The separation region length was found to increase with increasing Reynolds number and wall-to-freestream stagnation temperature and decreasing freestream Mach number. In [16], the author investigated the SWBLI phenomenon on a rigid flat plate experimentally. When the oblique shock wave impinged on the boundary layer, the boundary layer separated upstream of the impingement location. However, the separated boundary layer is reattached again to the surface downstream of the flow. Due to the streamlined curvature at the separation and reattachment point, instability of the boundary layer occurred because of the formation of Gortler vortices, called the Gortler boundary layer instability. This instability caused the transition of the boundary layer. The transition took place within the separation region and thus boundary layer can be considered turbulent close to the reattachment point. The amplitude of the Gortler-like vortices was influenced by the motion of the plate. The downward plate deflection resulted in a larger streamlined radius at the reattachment point reducing the Gortler-like vortices amplitude. However, the spanwise wavelength appeared to be unaffected.

2.2 Low-Fidelity Modeling

Low Fidelity Method (LFM), High Fidelity Method (HFM), and Reduced Order Models (ROMs) are the modeling approaches commonly used in the literature to model individual domains followed by coupling mechanisms [25]. Due to the impracticality of wind-tunnel tests of aero-elastically and aero-thermo-elastically scaled models and high computational complexity and cost of time-accurate unsteady CFD analysis, various approximate unsteady aerodynamic theories which assume inviscid flow and neglect real gas effects like Piston Theory (PT), Van Dyke's second-order theory, Newtonian Impact (NI) theory, and unsteady Shock-Expansion (SE) theory are implemented for preliminary design and sensitivity analysis of hypersonic configurations. Moreover, the quasi-steady nature of hypersonic flow fields wake effects can be neglected, as the disturbances cannot propagate upstream) has motivated the use of various hybrid approaches which combine the steady-state CFD analysis with the unsteady aerodynamic models like the piston theory [26]

2.3 Structural Modeling

In recent studies involving shock impingement on flexible panels, various levels of structural modeling fidelity have been adopted. Currao (2018) [27] and subsequent works [16] modeled the panel as a cantilevered beam using the classical Euler-Bernoulli beam theory. This simplification assumes that plane sections remain plane and normal to the beam axis, which is reasonable when the thickness-to-length ratio is very small (on the order of 10^{-3}). In Currao's experimental and numerical study [27], the structural response was captured using a finite element formulation where the mass matrix $\mathbf{M}$ and stiffness matrix $\mathbf{K}$ were modified to include Timoshenko shear correction factors. Additionally, a Rayleigh damping model considering the first two modes was implemented to account for energy dissipation in the system. While the Euler-Bernoulli and simplified Timoshenko beam models offer computational efficiency and reasonable accuracy for slender panels under moderate deflections, they have limitations in capturing complex three-dimensional effects, thermal stresses, and large deformation behavior commonly encountered in hypersonic fluid-thermal-structural interaction (FTSI) problems. These limitations motivate the use of higher-fidelity structural models, such as full three-dimensional finite element analysis using thermo-elastic solid elements, as employed in the present study.

2.4 Research Gap

There is a significant lack of research focused on reconciling experimental observations with numerical predictions in hypersonic FTSI problems. Specifically, limited efforts have been made to establish strong agreement between test data and simulations involving clamped thin panels subjected to combined shock and thermal loading. This research aims to address that gap by performing a detailed numerical study of a modified RC-19 panel configuration. The objective is to enhance test simulation agreement in hypersonic FTSI conditions, thereby improving validation of computational tools and guiding future experimental designs.

CHAPTER THREE: THEORY

3.1 Hypersonic Flows

There is no strict definition of hypersonic flow, but it is generally identified using a simple rule: a flow is considered hypersonic when the free stream Mach number is greater than 5 ($M_\infty > 5$). Hypersonic flow differs from supersonic flow due to several important physical effects, such as the presence of a thin shock layer, an entropy layer, strong high temperature effects, and significant viscous interactions [1].

3.2 Shock-Wave Boundary Layer Interaction (SWBLI)

SWBLI occurs when a shock wave impinges on a viscous boundary layer, creating an adverse pressure gradient that can cause flow separation [28, 6]. This separation forms a recirculation region with a separation shock, while downstream reattachment produces a reattachment shock [28]. Between these points, the flow exhibits complex compression and expansion patterns [28]. SWBLI significantly affects surface pressure, shear stress, and heat transfer, making it critical in high-speed and hypersonic vehicle design [28, 6].

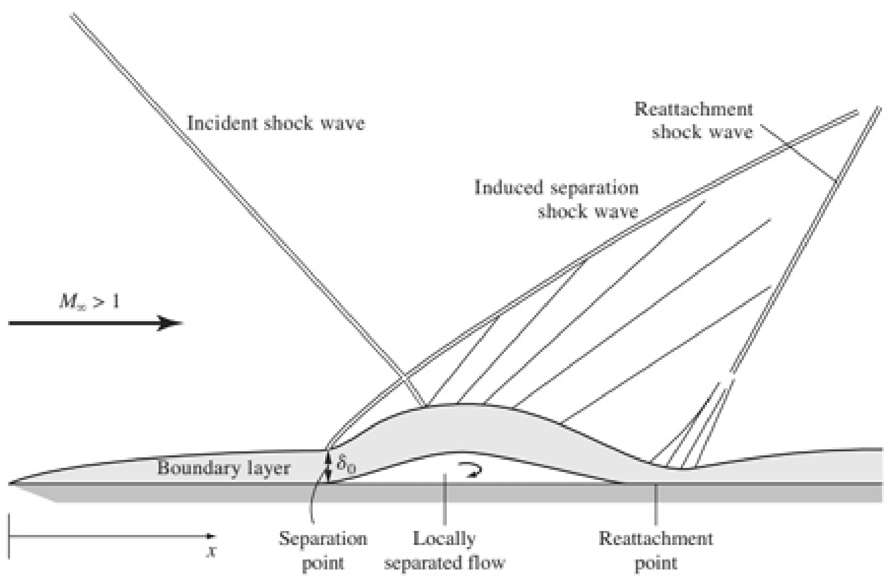

Figure 3.2: Schematic of shock wave boundary layer interaction [1]

3.3 Shock-Expansion Theory

Shock-expansion theory is a method that relates the local surface inclination(θ) to the flow properties behind oblique shocks and expansion fans. It is commonly used to compute the Mach number, pressure and other flow parameters in regions affected by shock or expansion waves [1].

3.3.1 Oblique Shock Wave Relations

The flow deflection angle θ and the shock angle β are related through the upstream Mach number M_1 as:

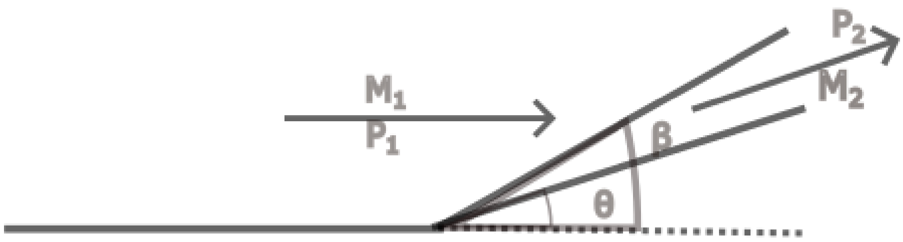

Figure 3.3: Oblique shock wave

$$\tan\theta = 2\cot\beta \frac{M_1^2 \sin^2\beta - 1}{M_1^2(\gamma + \cos 2\beta) + 2} \tag{3.1}$$

$$\frac{P_2}{P_1} = 1 + \frac{2\gamma}{\gamma+1}(M_{n,1}^2 - 1) \tag{3.2}$$

$$M_{n,2}^2 = \frac{1 + \frac{\gamma-1}{2} M_{n,1}^2}{\gamma M_{n,1}^2 - \frac{\gamma-1}{2}} \tag{3.3}$$

Here, the subscript "1" refers to conditions ahead of the shock and "2" refers to conditions behind the shock. n denotes the normal component of the Mach number:

$$M_{n,1} = M_1 \sin\beta \tag{3.4}$$

$$M_2 = \frac{M_{n,2}}{\sin(\beta - \theta)} \tag{3.5}$$

3.3.2 Expansion Wave Relations

For expansion fans, the change in flow properties is governed by the Prandtl-Meyer function $\nu(M)$:

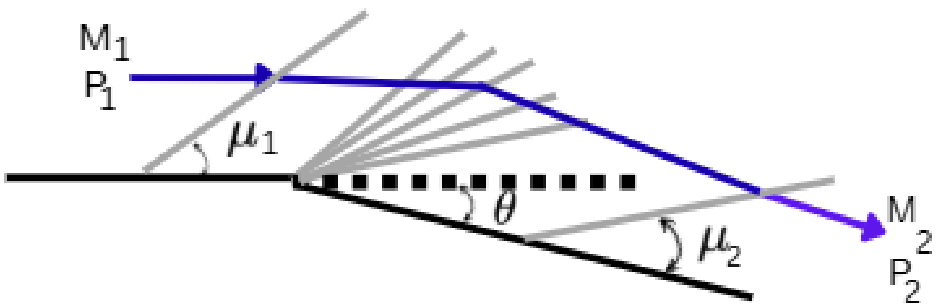

Figure 3.4: Illustration of Expansion Wave

$$\nu(M) = \sqrt{\frac{\gamma+1}{\gamma-1}}\tan^{-1}\left[\sqrt{\frac{\gamma-1}{\gamma+1}(M^2-1)}\right] - \tan^{-1}(\sqrt{M^2-1}) \tag{3.6}$$

$$\theta = \nu(M_2) - \nu(M_1) \tag{3.7}$$

Since expansion waves are isentropic, the flow relations can be expressed as:

$$\frac{p_2}{p_1} = \left(\frac{1+\frac{\gamma-1}{2}M_1^2}{1+\frac{\gamma-1}{2}M_2^2}\right)^{\frac{\gamma}{\gamma-1}} \tag{3.8}$$

$$\frac{T_2}{T_1} = \frac{1+\frac{\gamma-1}{2}M_1^2}{1+\frac{\gamma-1}{2}M_2^2} \tag{3.9}$$

These equations allow determination of flow parameters behind both shocks and expansion waves on inclined surfaces.

3.4 Piston Theory

Piston theory is an inviscid aerodynamic method used to calculate the surface pressure on bodies in high speed flow. Using the piston analogy, which assumes that a piston moves in a one-dimensional channel, the pressure on the structure's surface is determined. As shown in figure 3.2, the air molecules above the surface are thought to compress isentropically by a piston traveling at a speed equal to the structure plus the free stream velocity times the inclination angle.

3.4.1 Classical Piston Theory

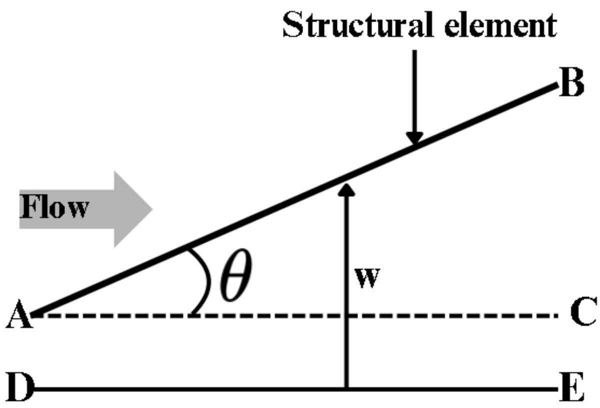

Figure 3.5: Schematic representation of Classical Piston Theory

where,

- w is the vertical displacement
- θ is the inclination of the structural element with respect to the free-stream direction

The piston speed is given by:

$$v = w + U \tag{3.10}$$

The local pressure is approximated using freestream flow quantities (pressure and Mach number).

Second-order piston theory is given by:

$$\frac{p(x,t)}{p_\infty} = (1+\frac{\gamma-1}{2}M_\infty)^{\frac{2\gamma}{\gamma-1}} \tag{3.11}$$

Similarly, third-order piston theory is given by:

$$\frac{p(x,t)}{p_\infty} = 1+\gamma M_\infty \frac{w}{U_\infty} + \frac{\gamma+1}{4}M_\infty^2\left(\frac{w}{U_\infty}\right)^2 + \frac{\gamma+1}{12}M_\infty^3\left(\frac{w}{U_\infty}\right)^3 \tag{3.12}$$

3.4.2 Local Piston Theory

Under three-dimensional flow conditions, particularly at high Mach numbers and large surface inclinations, the local pressure may be approximated in terms of the governing flow variables.

Second-order approximation:

$$p(x,t) = p_{\text{loc}}\left(1+\frac{\gamma-1}{2}M_{\text{loc}}\theta(t)\right)^{\frac{2\gamma}{\gamma-1}} \tag{3.13}$$

Third-order approximation:

$$p(x,t) = p_{\text{loc}}\left[1+\gamma M_{\text{loc}}\theta(t) + \frac{\gamma(\gamma-1)}{4}\left(M_{\text{loc}}\theta(t)\right)^2 + \frac{\gamma(\gamma-1)}{4}\left(M_{\text{loc}}\theta(t)\right)^3\right] \tag{3.14}$$

3.4.3 CFD enriched Piston Theory

CFD enriched piston theory improves the accuracy of conventional piston theory by incorporating flow variables obtained from steady state CFD simulations into the formulation. By using these refined inputs, the method provides better approximations of aerodynamic loading. However, when applied to transient phenomena such as oscillating shock waves, discrepancies may arise due to the inherently unsteady nature of the flow.

3.5 Governing Equations

3.5.1 Computational Fluid Dynamics

The rhoCentralFoam, a density-based solver in OpenFOAM, is selected as the fluid solver in this study. It solves the Navier-Stokes (NS) equations for a transient, compressible flow, which is given below in index form:

$$\frac{\partial \rho}{\partial t} + \nabla \cdot (\rho u) = 0, \tag{3.15a}$$

$$\frac{\partial (\rho u)}{\partial t} + \nabla \cdot (\rho u \times u + pI - \tau) = 0, \tag{3.15b}$$

$$\frac{\partial (\rho E)}{\partial t} + \nabla \cdot [(\rho E + p)u - \tau \cdot u + q] = 0, \tag{3.15c}$$

where

- ρ is the fluid density,
- u is the velocity vector,
- p is the static pressure,
- $E = e + \frac{1}{2}u \cdot u$ is the total energy per unit mass,
- τ is the viscous stress tensor,
- q is the heat flux vector.

The viscous stress tensor for a Newtonian fluid is given by

$$\tau = \mu \left(\nabla \mathbf{u} + (\nabla \mathbf{u})^T - \frac{2}{3}(\nabla \cdot \mathbf{u})\mathbf{I} \right), \tag{3.16}$$

and the heat flux follows Fourier's law

$$\mathbf{q} = -k \nabla T \tag{3.17}$$

with μ the dynamic viscosity (computed via Sutherland's law) and k the thermal conductivity. For two dimensional compressible,viscous flow,in indices form is given by:

$$\frac{\partial \rho}{\partial t} + \frac{\partial \rho u_i}{\partial x_i} = 0, \tag{3.18a}$$

$$\frac{D\rho u_i}{Dt} = -\frac{\partial p}{\partial x_i} + \frac{\partial \tau_{ij}}{\partial x_j}, \tag{3.18b}$$

$$\frac{D(\rho e)}{Dt} = -p\frac{\partial u_i}{\partial x_i} + \tau_{ij}\frac{\partial u_i}{\partial x_j} + \frac{\partial}{\partial x_i}\left(k\frac{\partial T}{\partial x_i}\right), \tag{3.18c}$$

where τ_{ij} denotes the viscous force term given by:

$$\tau_{ij} = \mu\left(\frac{\partial u_i}{\partial x_j} + \frac{\partial u_i}{\partial x_i} - \frac{2}{3}\frac{\partial u_k}{\partial x_k}\delta_{ij}\right), \tag{3.19}$$

The symbol $\frac{D}{Dt}$ represents the substantial derivative given by:

$$\frac{D}{Dt} = \frac{\partial}{\partial t} + u_i\frac{\partial}{\partial x_j} \tag{3.19}$$

The indices represent the 2 orthogonal directions. So that:

$$i = 1,2 \tag{3.20}$$

$$j = 1,2 \tag{3.20}$$

$$k = 1,2 \tag{3.21}$$

$$\delta_{ij} = \begin{cases} 1 & \text{if } i = j \\ 0 & \text{if } i \neq j \end{cases} \tag{3.21}$$

The system is closed by the ideal gas equation of state

$$p = \rho RT, \qquad e = c_v T, \qquad \gamma = \frac{c_p}{c_v}, \qquad R = c_p - c_v, \tag{3.22}$$

where $\gamma = 1.4$ and $R = 287.05$ J kg^{-1} K^{-1} for air. The viscosity μ is calculated using the Sutherland relation:

$$\frac{\mu}{\mu_{\text{ref}}} = \left(\frac{T}{T_{\text{ref}}}\right)^{3/2} \frac{T_{\text{ref}} + S}{T + S} \tag{3.26}$$

where $\mu_{\text{ref}} = 1.789 \times 10^{-5}\,\text{kg m}^{-1}\text{s}^{-1}$, $T_{\text{ref}} = 288\,\text{K}$, and $S = 110\,\text{K}$. The thermal conductivity is defined as:

$$k = \frac{\mu C_p}{Pr} \tag{3.27}$$

The unsteady aerodynamic pressure is approximated using local piston theory as stated in equation (1.12) and (1.13).

3.5.2 Structural Solver

The finite element method (FEM), as implemented in CalculiX, is used for discretization of the governing equation of solid. Elastic and compressible structures are governed by the following equation in CalculiX [29].

$$\rho \frac{\partial^2 \mathbf{w}}{\partial t^2} + \nabla \cdot \Sigma = 0, \tag{3.23}$$

where the Cauchy stress tensor Σ is given by the linear isotropic elastic constitutive law (Hooke's law):

$$\Sigma = 2\mu\varepsilon + \lambda\,\text{tr}(\varepsilon)\mathbf{I}, \tag{3.24}$$

and the infinitesimal strain tensor ε is defined as

$$\varepsilon = \frac{1}{2}\big((\nabla \mathbf{d})^T + \nabla \mathbf{d}\big). \tag{3.25}$$

In these equations,

- $\mathbf{w}$ is the displacement vector,

- ρ is the material density,
- (μ, λ) are the Lame parameters,
- $\mathbf{I}$ is the second-rank unit tensor (identity tensor),
- $\mathrm{tr}(\cdot)$ denotes the trace operator.

The Lamé parameters μ and λ are related to Young's modulus E and Poisson's ratio ν via

$$\mu = \frac{E}{2(1+\nu)}, \qquad \lambda = \frac{E\nu}{(1+\nu)(1-2\nu)}. \tag{3.26}$$

3.5.3 Thermal Solver

Thermal Solver is the responsible for calculating the heat conduction and temperature distribution within solid components, which is then coupled with fluid and structural solvers.Calculix is also used as thermal solver.

3.5.3.1 Heat Conduction

Temperature variation along the length is governed by Fourier's Law.The system is simplified to a one-dimensional case to reduce

$$\rho c_p \frac{\partial T}{\partial t} = k \frac{\partial^2 T}{\partial x^2} + q \tag{3.27}$$

3.5.4 Fluid Structure Interface

Fluid kinematic and dynamic coupling conditions must be satisfied at the fluid-solid interface for a two-way coupled FSI simulation. The kinematic coupling condition ensures that the fluid and structure have the same velocity as well as displacement at the interface.

$$\mathbf{x}_F = \mathbf{w}_S, \tag{3.28a}$$

$$\mathbf{v}_F = \frac{\partial \mathbf{w}_S}{\partial t}. \tag{3.28b}$$

Similarly, the dynamic coupling condition ensures the stress or force balance between the fluid and structure:

$$\sigma_F \cdot \mathbf{n}_F = -\sigma_S \cdot \mathbf{n}_S, \tag{3.29}$$

where $\mathbf{n}_F$ and $\mathbf{n}_S$ are the outward unit normals from the fluid and solid domains, respectively (usually $\mathbf{n}_S = -\mathbf{n}_F$).

Kinematic coupling conditions cannot be fully employed in inviscid FSI as the inviscid assumption uses slip boundary conditions at the wall. Coupling velocity at the interface will create a velocity gradient in the flow over the interface. This velocity gradient becomes non-physical in the absence of viscosity. As a result, velocity data is not mapped between the fluid and solid interface in inviscid FSI.

3.5.5 Fluid Thermal Structure Interface

In a two-way coupled FTSI simulation, the interface between the fluid and solid domains must satisfy kinematic, dynamic, and thermal coupling conditions. These ensure consistent transfer of momentum, deformation, and heat across the interface.

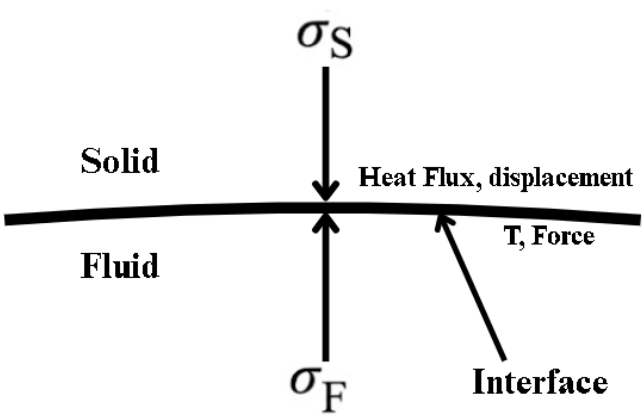

Figure 3.6: FTSI Interface

3.5.5.1 Kinematic Coupling

The kinematic coupling condition enforces the continuity of displacement and velocity at the fluid-structure interface. Physically, this implies that the fluid particles in contact with the structure follow the structural motion without separation or penetration. Mathematically, this can be expressed as:

$$\mathbf{x}_F = \mathbf{w}_S, \tag{3.30a}$$

$$\mathbf{v}_F = \frac{\partial \mathbf{w}_S}{\partial t}, \tag{3.30b}$$

where $\mathbf{x}_F$ is the position of the fluid interface, $\mathbf{w}_S$ is the structural displacement, and $\mathbf{v}_F$ is the fluid velocity at the interface.

3.5.5.2 Dynamic Coupling

The dynamic coupling condition ensures equilibrium of forces at the interface. The stresses exerted by the fluid must be balanced by the stresses within the structure. This condition is given by:

$$\sigma_F \cdot \mathbf{n}_F = -\sigma_S \cdot \mathbf{n}_S, \tag{3.31}$$

where σ_F and σ_S represent the fluid and solid stress tensors, respectively, and $\mathbf{n}_F$ and $\mathbf{n}_S$ are the outward unit normals to the fluid and solid domains. Typically, $\mathbf{n}_S = -\mathbf{n}_F$, ensuring action–reaction consistency.

3.5.5.3 Thermal Coupling

In addition to mechanical interactions, FTSI requires thermal continuity across the interface. This involves both temperature and heat flux continuity conditions:

$$T_F = T_S, \tag{3.32a}$$

$$-k_F \nabla T_F \cdot \mathbf{n}_F = -k_S \nabla T_S \cdot \mathbf{n}_S, \tag{3.32b}$$

where T_F and T_S denote the temperatures of the fluid and solid at the interface, and k_F and k_S are their respective thermal conductivities. The first condition ensures no temperature jump, while the second enforces conservation of heat flux across the interface.

3.5.5.4 Inviscid Flow Assumption in FTSI

For inviscid FTSI simulations, the absence of viscosity implies slip boundary conditions at the fluid-structure interface. Under such conditions, enforcing full kinematic coupling particularly velocity continuity can introduce nonphysical velocity gradients near the interface. Therefore, similar to inviscid FSI, velocity mapping between fluid and structure may be relaxed or modified. However, thermal coupling remains valid and essential, as heat transfer is independent of viscous effects and must still satisfy temperature and heat flux continuity.[30]

3.6 FTSI Coupling

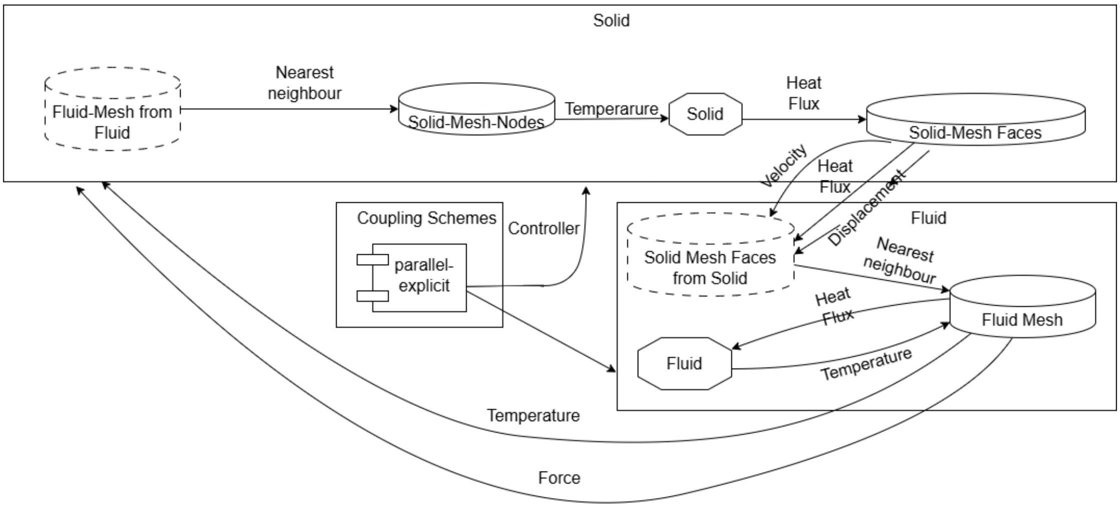

Figure 3.7: Schematic showing FTSI coupling procedure

3.6.1 Monolithinc and Partitioned approach

The monolithic approach combines the fluid, thermal, and structural physics into a single mathematical system to solve them all at once. This simultaneous calculation ensures high numerical stability and accurate energy transfer at the interfaces. However, it requires significant computational power and a specialized solver to manage the large, complex matrix.

$$A(X) = F \tag{3.33}$$

Where:
X is the global state vector for all variables.
F represents the external load vector.

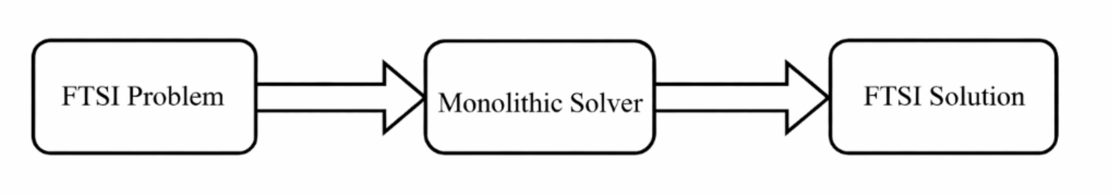

Figure 3.8: Schematic of Monolithic FTSI Approach

The partitioned approach is another coupling approach where the structure and fluid are treated as two distinct system. The information between them are exchanged between them using a coupling tool,usually preCICE.Instead of solving a single global matrix,this method uses seperate solvers for calculating pressure,displacement,temperature and heatflux.At each time step, the fluid solver calculates force and temperature and pass the information to solid solver,which then updates panel's deformation and heatflux.In this approach, the system is split into two distinct but coupled operators:

$$F(F,T) = f_f \tag{3.34}$$

$$S(q,v,y_p) = f_s \tag{3.35}$$

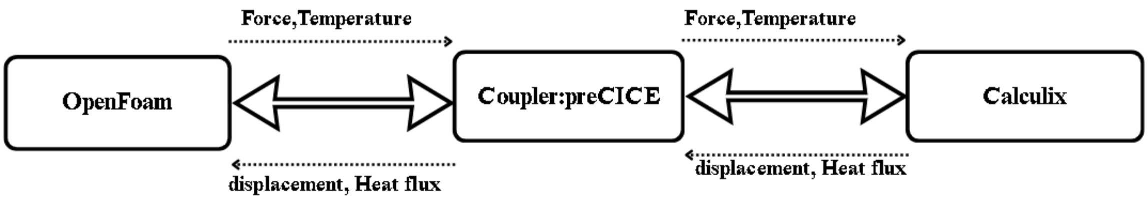

Figure 3.9: Schematic of Partitioned FTSI Approach

3.6.2 Explicit Coupling

In an explicit coupling approach, the fluid and structural solvers are advanced using a fixed number of iterations per time step, often limited to just one. As a result, full kinematic and dynamic equilibrium at the interface is not always achieved within that time step. This limitation can lead to instability, particularly in scenarios involving strong FSI where the structural response undergoes significant deformation during a single time increment. Explicit coupling strategies can be further categorized as serial or parallel, depending on how the solvers are executed. In the case of serial explicit coupling, one solver is advanced first from time level t_n to t_{n+1}. The second solver is then executed using the updated boundary information provided by the first solver as its input. Ifx_1 and x_2 represent the input variables for solvers S_1 and S_2, respectively, the solution procedure for serial explicit coupling can be expressed as follows:

$$x_2^{n+1} = {S_1}^n.x_1^n \tag{3.36}$$

$$x_1^{n+1} = S.x_2^{n+1} \tag{3.37}$$

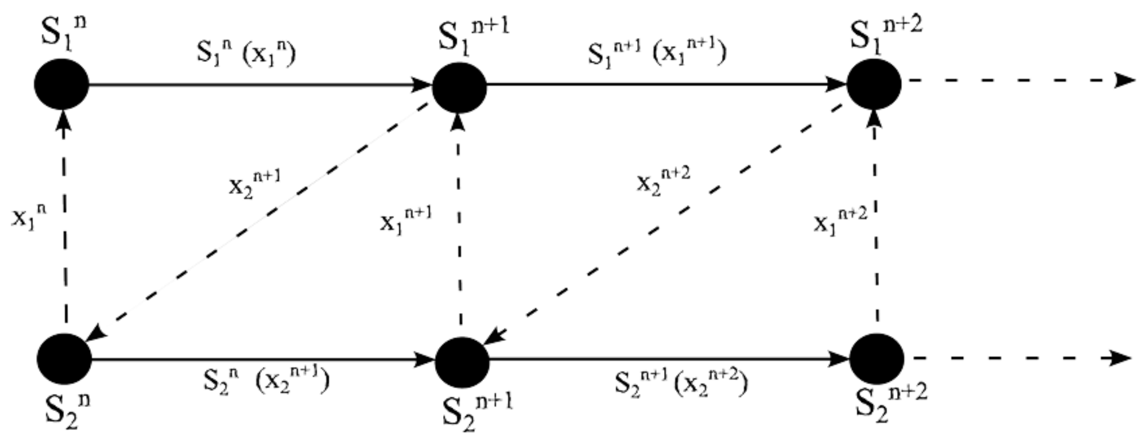

Figure 3.10: Serial Coupling Schematic

In this formulation, x_2 represents the aerodynamic forces acting on the panel, while x_1 indicates the transverse displacement of the structure. The operators S_1 and S_2 correspond to the fluid and structural solvers, respectively.

By contrast, in a parallel explicit coupling scheme, both solvers are advanced simultaneously, relying solely on the information available from the preceding time step.

$$x_2^{n+1} = {S_1}^n.x_1^n \tag{3.38}$$

$$x_1^{n+1} = S.x_2^n \tag{3.39}$$

While explicit coupling is straightforward to implement and computationally efficient, it may not perform well in cases where the interaction between fluid and structure is strong. In hypersonic applications, shock-induced loading can change rapidly, which may lead to noticeable structural response within a short time interval. Under such conditions, very small time steps are often required to maintain stability.

3.6.3 Implicit Coupling

In contrast to explicit coupling, the implicit coupling approach involves iterative information exchange between the fluid and structural solvers within each time step. The objective is to achieve better consistency at the fluid–structure interface by repeatedly updating the solution until a convergence criterion is satisfied.

For the present FTSI problem, the fluid solver computes the aerodynamic load based on the current estimate of structural displacement, while the structural solver updates the displacement using the latest fluid loading. This process is repeated within the same time step until the change between successive iterations becomes sufficiently small.

In iteration k within the time level $n+1$, the serial implicit coupling scheme can be expressed as:

$$x2_{k+1}^{n+1} = S_1{}^n.(x1_k^{n+1}) \tag{3.40}$$

$$x2_{k+1}^{n+1} = S_1{}^n.(x1_{k+1}^{n+1}) \tag{3.41}$$

In iteration k within the time level $n+1$, the parallel implicit coupling scheme can be expressed as:

$$x2_{k+1}^{n+1} = S_1{}^n.(x1_k^{n+1}) \tag{3.42}$$

$$x2_{k+1}^{n+1} = S_1{}^n.(x1_k^{n+1}) \tag{3.43}$$

The iterations continue until convergence is achieved, which can be defined in terms of displacement or load as:

$$\left| x2_{k+1}^{n+1} - x2_k^{n+1} \right| < \varepsilon \tag{3.44}$$

where ε is a predefined tolerance.

Compared to explicit coupling, the implicit approach provides improved stability and is better suited for strongly coupled problems such as hypersonic fluid–structure interaction, where rapid changes in aerodynamic loading can significantly influence structural response. However, this improved stability comes at the cost of increased computational effort due to the iterative procedure within each time step.

CHAPTER FOUR: METHODOLOGY

The flowchart below shows the methodology approach being followed for the project.

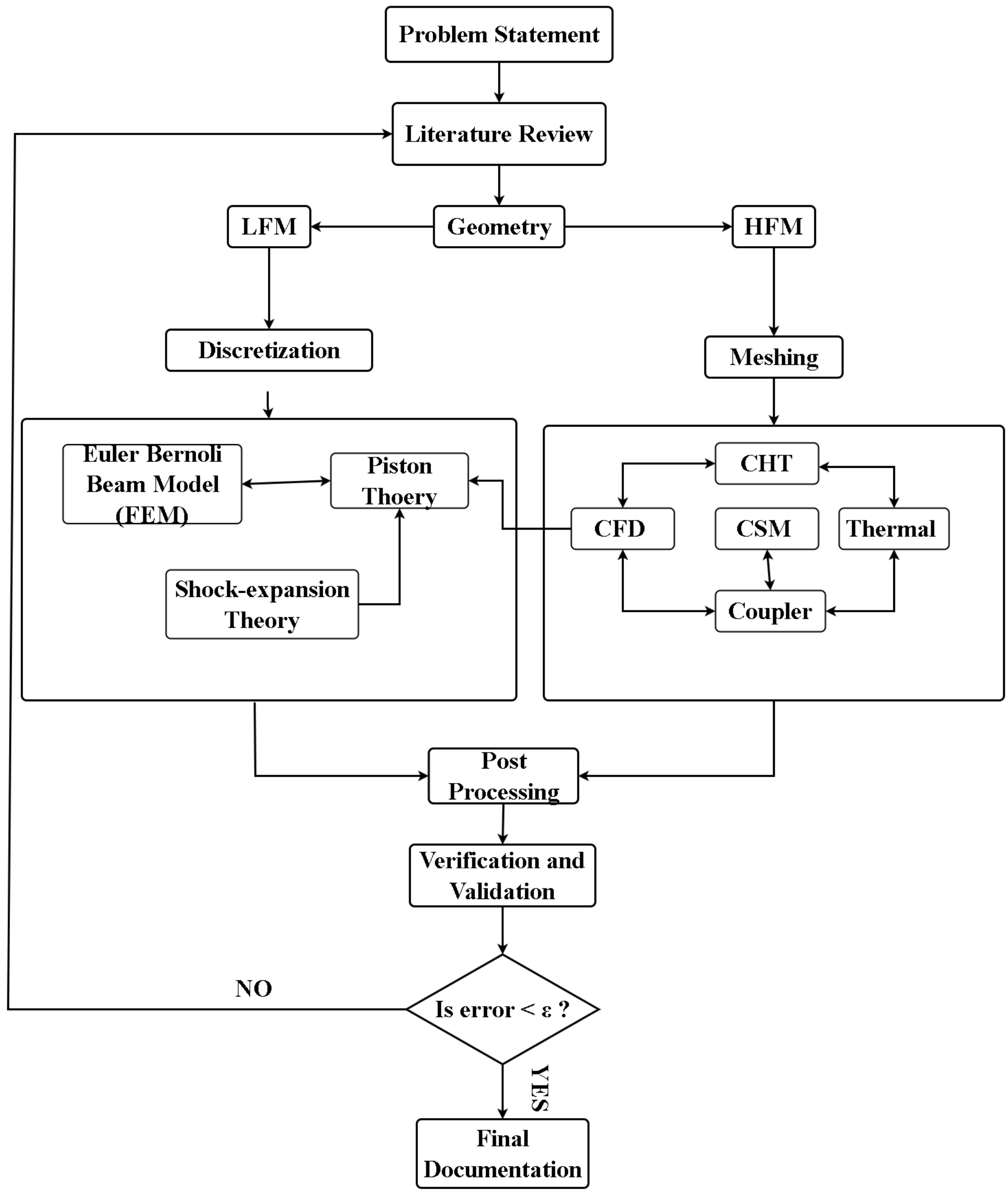

Figure 4.11: Methodology Flowchart

where,

- ε is the tolerance value

In the low-fidelity model (LFM), the plate was modeled as a two dimensional clamped clamped structure based on the Euler Bernoulli beam theory. The unsteady aerodynamic pressure distribution was approximated using analytical piston theory. The initial flow conditions required for the piston theory were determined using shock expansion theory and oblique shock relations. Then heat flux was evaluated by considering one dimensional heat conduction along the plate in conjunction with an empirical cooling effectiveness method. The resulting formulation enabled the estimation of the optimum wall temperature, which was then utilized to determine the corresponding heat flux.
High fidelity modeling methods was used for FTSI predictions in this study. Coupled fluid thermal structure interaction simulation is carried out in viscous flow using OpenFOAM, CalculiX, and coupled through preCICE.
Verification and validation served as fundamental tool in the execution of numerical simulations. These processes addressed different sources of error. The validation focused on reducing conceptual modeling errors to ensure physical accuracy. While, verification targets numerical errors to ensure correct mathematical implementation. Verification was further divided into code and calculation verification. Verification was carried out through a Grid Convergence Study to confirm mesh independent and reliable results.

4.1 Workbench Case

This study uses computational simulations to analyze the response of a thin panel exposed to high-speed airflow. The selected workbench case is the RC-19 experimental case, which was previously tested in a supersonic wind tunnel for Mach numbers ranging from 1.5 to 3. The experimental configuration is used as a reference for validating the numerical solver.

4.1.1 Geometry

In the present configuration, a Mach 2 flow is imposed at the inlet. A wedge is placed at the bottom of the domain to generate shock waves, which subsequently impinge on the panel located in the upper-right region of the test section. The panel is enclosed by a cavity chamber to maintain the required pressure and temperature conditions. The geometry of the setup is illustrated in Figure 4.12.

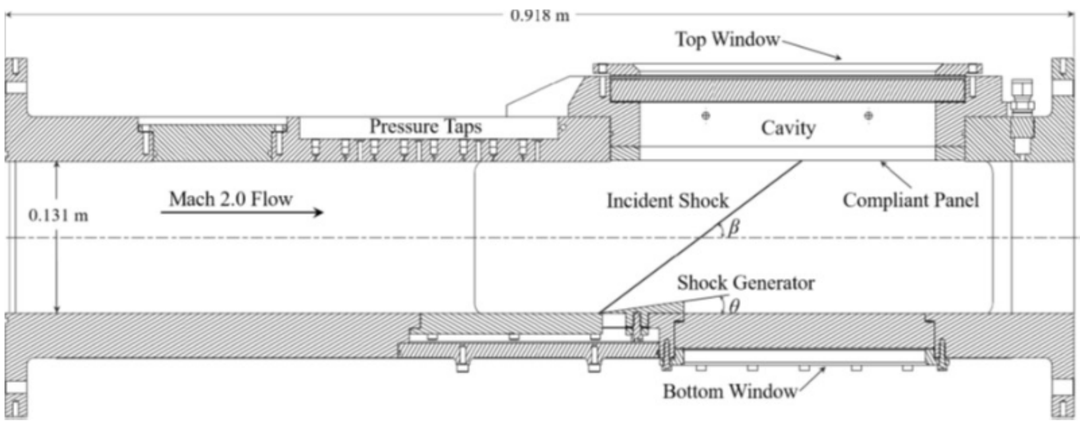

Figure 4.12: Schematic view of the RC-19 test setup [2].

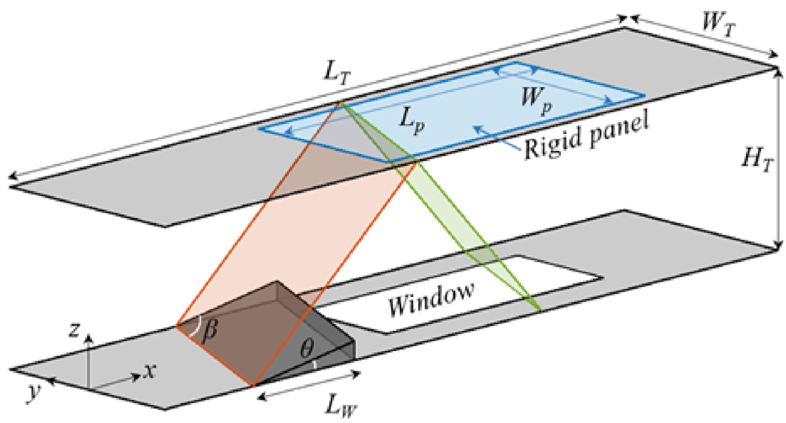

Figure 4.13: RC-19 reference geometry showing shock impingement on a thin compliant panel [2]

Table 4.3: Geometric Dimensions of RC-19 Panel

Parameter	**Value (mm)**
Test section length, L_T	918
Test section width, W_T	152
Test section height, H_T	131
Rigid panel length, L_p	254
Rigid panel width, W_p	127
Rigid panel thickness, h_p	12.7

4.1.2 Boundary Conditions

The simulation uses flow conditions based on the RC-19 benchmark. Table 4.4 shows the values used in the Supersonic case and its modification for hypersonic case. The flow duration is assumed to be 200 milliseconds with a Reynolds number unit of 7.1×10^6.

Table 4.4: Operating Conditions

Operating Condition	M_∞	P_∞(KPa)	P_0(KPa)	T_0(K)	T_∞(K)	U_∞(m/s)	γ	C_p(J/kg.K)
RC-19 Clamped Thin Pane	1.92	345	2382.92	503.73	290	655.4	1.4	1004.5
RC-19 inspired hypersonic simulation	6.00	0.62	980	580	70.73	1006.24	1.4	1005

Table 4.5: Boundary Conditions for Viscous Simulation

Patch	U	p	T
Inlet	fixedValue	zeroGradient	fixedValue
Plate	noSlip (movingWallVelocity for FSI)	zeroGradient	fixedValue
Wedge	noSlip	zeroGradient	fixedValue
Wall	noSlip	zeroGradient	inletOutlet
Outlet	inletOutlet	waveTransmissive	inletOutlet

Table 4.6: Boundary Conditions for Inviscid Simulation

Patch	U	p	T
Inlet	fixedValue	zeroGradient	fixedValue
Plate	Slip (movingWallVelocity for FSI)	zeroGradient	fixedValue
Wedge	Slip	zeroGradient	fixedValue
Wall	Slip	zeroGradient	inletOutlet
Outlet	inletOutlet	waveTransmissive	inletOutlet

4.1.3 Discretization

The model was discretized in time using the Euler scheme. This scheme is implicit and first-order accurate in time.

$$\frac{\partial \phi}{\partial t} = \frac{\phi - \phi_o}{\Delta t} \tag{4.45}$$

rhoCentralFoam is based on the central upwind scheme of Kurganov and Tadmor. Kurganov was used as the flux scheme [?]. This scheme is second-order accurate. Likewise, the gradient terms were discretized using the cellLimited Gauss linear scheme to ensure that the face values obtained by extrapolating the cell value to the cell faces using the gradient are bounded by the neighboring cell's minimum and maximum limit. This scheme is first-order accurate. Laplacian terms in the governing equations were discretized using Gauss linear limited scheme. Here, the limited is used for explicit non-orthogonal correction of a surface normal gradient that is required to evaluate the laplacian term. This scheme is firstorder accurate. Gauss linear was used for divergence term discretization. Likewise, the linear scheme 38 was used as the default for the interpolation of variables. This scheme is first-order accurate. TVD schemes must be used for interpolation of reconstructed variables in rhoCentralFoam to reduce numerical oscillations [31]. Of various TVD schemes, MinMod and VanAlbada schemes were found to work well in inviscid and viscous simulation respectively. TVD schemes are second-order accurate in space.

Table 4.7: Discretization schemes used and order of accuracy

Discretization Scheme	**Scheme**	**Order of Accuracy**
Temporal	Euler Implicit	First
Flux	Kurganov	Second
Gradient	cellLimited Gauss linear	First
Laplacian	Gauss linear limited	First
Interpolation	MinMod (Inviscid) vanAlbada (Viscous)	Second Second

4.1.4 Solution Methods and Controls

The flux variables of the governing equations (*rho*, *rhoU*, *rhoE*) were first computed explicitly using the diagonal solver. Then the velocity vectors and energy variables were computed using the smoothSolver. The absolute and relative convergence tolerances for smoothSolver were set to 1e-10 and 0 respectively. Adjustable time stepping was used with a maximum courant number of 0.5. Cell displacement of the fluid mesh also needs to be solved for FSI simulation. This was done using a GAMG solver with absolute and relative tolerance measures of 1e-6 and 1e-4 respectively.

4.1.5 Mesh

The mesh was generated using `blockMesh`. The medium mesh consists of 69,576 cells, with a first cell height of 5×10^{-6} m and a corresponding y^+ value of approximately 1. The mesh is refined near the wall to accurately capture the boundary layer and is gradually coarsened toward the middle of the domain. To reduce the computational cost of the simulation, the domain beyond the wedge and downstream of the panel was removed, and a coded boundary condition was applied at the new inlet. This approach significantly reduces the total number of mesh cells and, consequently, the overall computational cost.

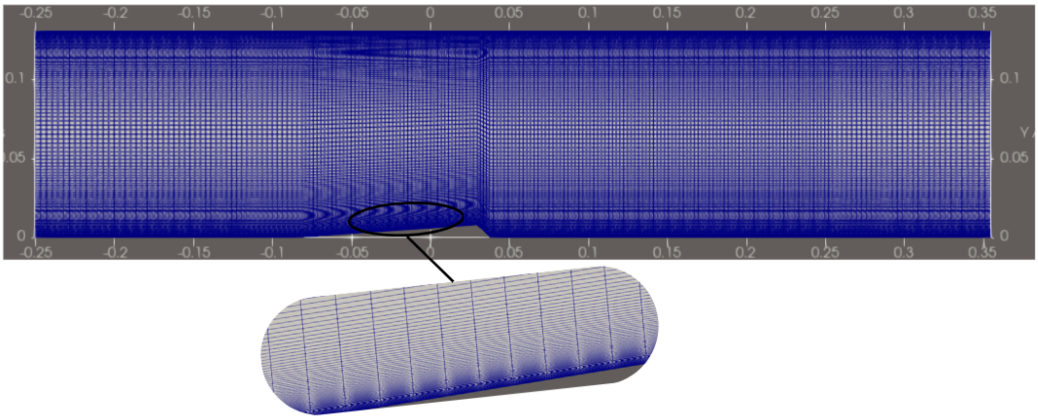

Figure 4.14: Mesh for supersonic Case Validation

4.1.6 GCI

GCI study is carried out in every simulation to ensure that the numerical results are not influenced by grid resolution. It is also performed to identify a mesh that balances accuracy and computational cost. Four different mesh sizes 15,912, 34,540, 69,080, 138,160 were used for coarse, medium, fine, and very fine meshes, respectively, to validate the RC-19 case. The grid refinement factor was defined by h, commonly used for two-dimensional simulations [18]. The shock impingement distance from the leading edge of the plate (xip, mm) was chosen as the representative convergence parameter. The shock impingement locations for the coarse, medium, fine, and very fine meshes were 0.135096, 0.133009, 0.129191, and 0.128710, respectively. Using the Grid Convergence Index (GCI) method proposed by Roache [32] the apparent order of convergence (p) was calculated iteratively and found to be 2.988707, indicating a nearly quadratic rate of convergence. The extrapolated shock impingement distance at infinite grid resolution was xip = 0.128641 mm. The asymptotic ratio of convergence (ARoC) was 0.996277, confirming that the solution lies within the asymptotic convergence range and that the mesh refinement was sufficient to achieve grid-independent results confirmed from 5.9. From the GCI study, the discretization error for the medium mesh in calculating relative shock impingement was below 0.53896

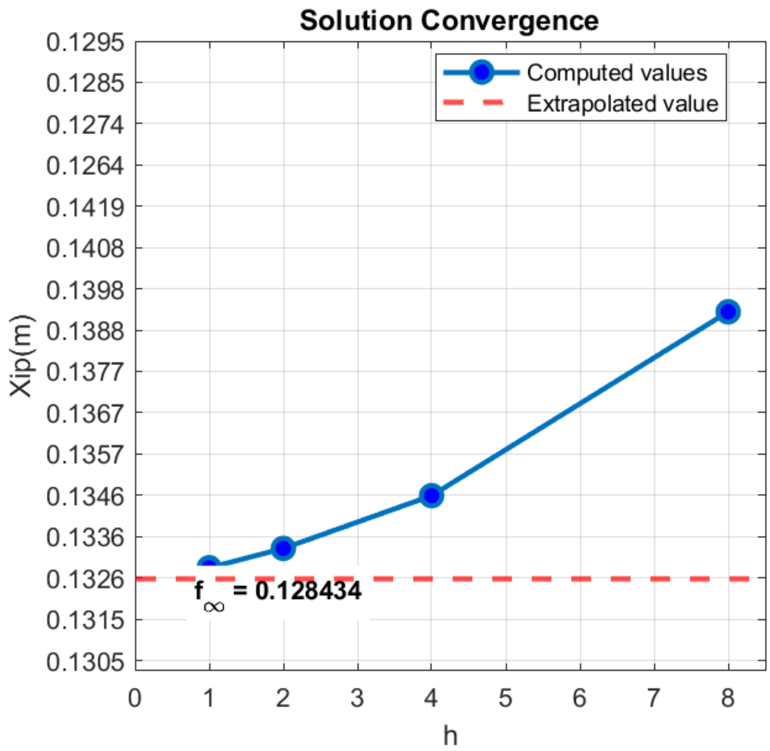

Figure 4.15: Variation of shock impingement distance (x_{ip}) with Grid Refinement Factor (h)

Table 4.8: Mesh Independence Study for RC-19 Benchmark Case

Mesh	**No. of Elements**	x_{ip}	**Relative error** ($\eta\%$)	**GCI** ($\%$)
Coarse	15912	0.135096	5.0181	0.2827
Medium	34540	0.130509	3.395	0.5325
Fine	69080	0.129191	0.4278	0.0673
Very Fine	138160	0.128710	0.0539	-

4.1.7 Verification and Validation

In the RC-19 benchmark test, an oblique shock generated by a wedge impinges on the panel under supersonic flow conditions. Two wedge angles, namely 4° and 8°, were considered in the study. The standard baseline for validation was established using the P/P_∞ versus x/L_p distribution, as shown in Figure 4.16 and Figure 4.18. These distributions served as the primary reference for assessing the accuracy of the numerical model. By comparing the computed results with the experimental data, the `rhoCentralFoam` solver was successfully validated, showing good agreement with the reference results. The error between the CFD and experimental results was found to be 4.65% for the 4° wedge case, while an deviation of 6.1% was observed for the 8° wedge case.

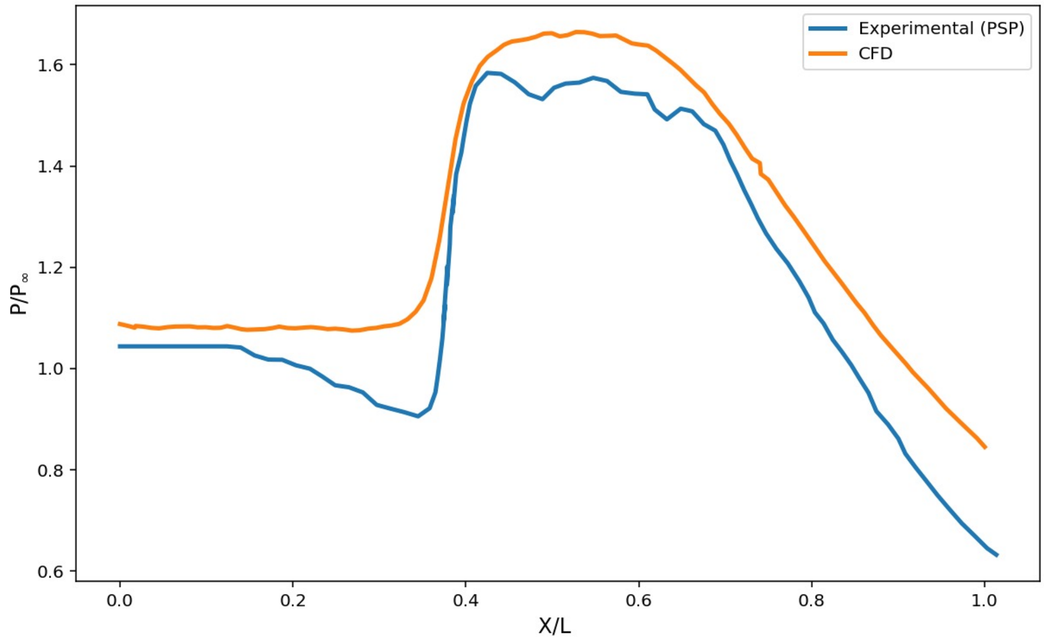

Figure 4.16: Normalized pressure P/P_∞ distribution over the clamped plate for 4° wedge

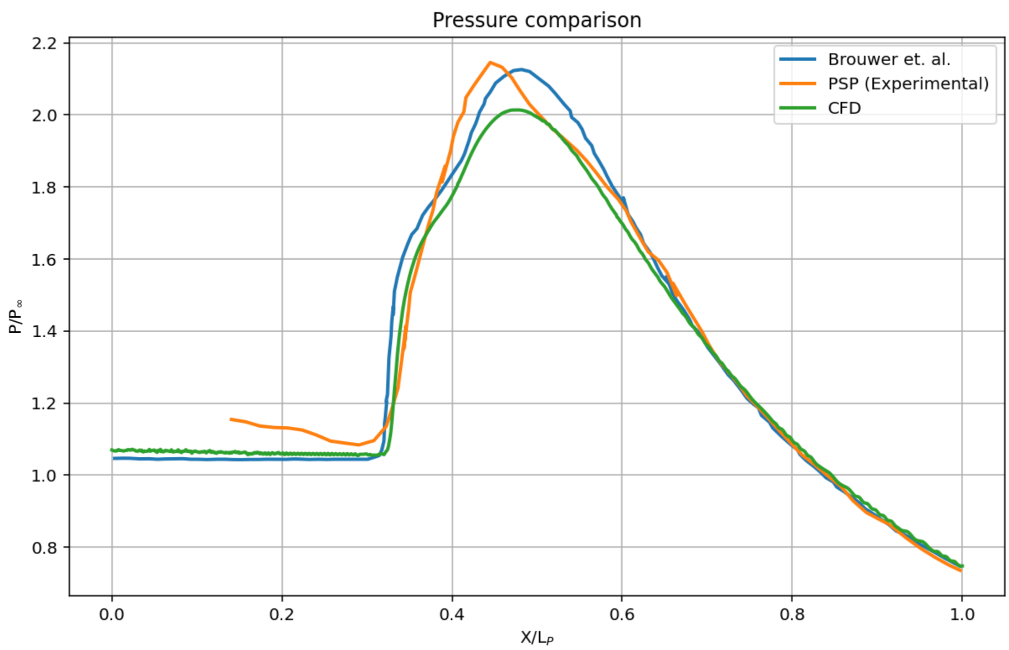

Figure 4.17: Normalized pressure P/P_∞ distribution over the clamped plate for 8° wedge

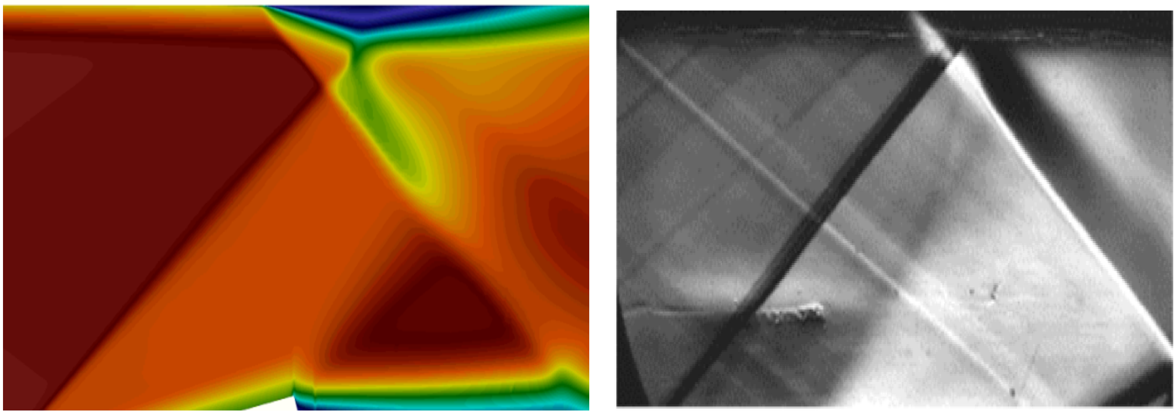

(a) Supersonic CFD　　(b) Schlieren plot at 8° wedge

Figure 4.18: Comparison of the contour with experimental schlierene image

A comparison between the CFD results and Schlieren images was carried out to validate the CFD result.The values are shown in Table 4.9 The incident shock angle from CFD 40.55 is slightly higher than the Schlieren value 37.91, giving a difference of about 2.6. For the separation shock, the CFD result 41.68 is very close to the Schlieren measurement 40.68, with a difference of around 1. Overall, the agreement is quite good, showing that the CFD model is able to capture the shock behavior reliably. The small differences can be explained by factors such as grid resolution, numerical methods, and limitations in experimental measurements.

Table 4.9: Comparison of Simulation and Experiment Angles for RC-19

Parameters	**Simulation**	**Experiment**
Incident Shock	40.55	37.91
Separation Shock	41.68	40.68

4.1.7.1 Contour for Supersonic Case

The Mach number contours for the 8° and 4° wedge cases are presented in Figure 4.19 and Figure 4.20, respectively. Additional contour plots are provided in the appendix to maintain the conciseness of the main report.

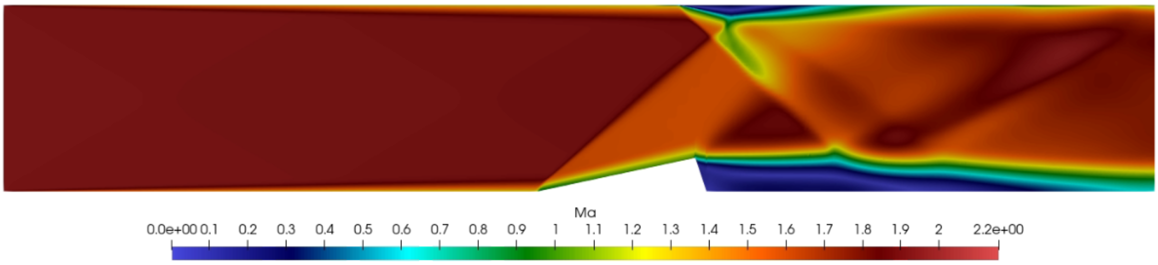

Figure 4.19: Mach Contour at 8° wedge

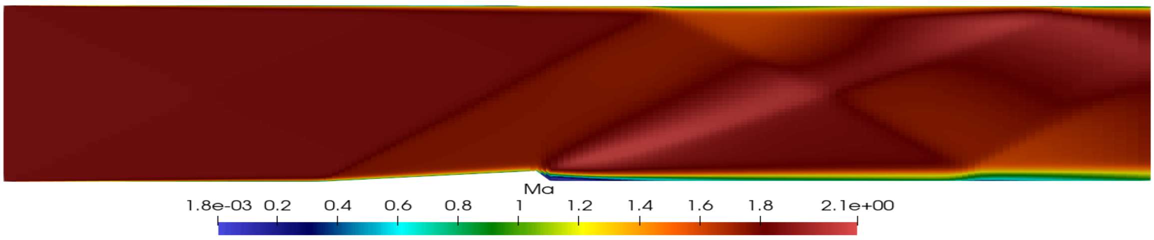

Figure 4.20: Mach contour at 4° wedge

4.2 Hypersonic Case

In order to fulfill the specific objectives of this study and address the identified research gap, the original workbench case setup is not sufficient for hypersonic FTSI analysis. Therefore, the case is modified by adjusting the boundary conditions, panel length, wedge angle, cavity pressure, and cavity temperature to ensure effective interaction among the fluid, thermal, and structural domains of the thin panel subjected to hypersonic flow.

4.2.1 Geometry

The geometry was modified by incorporating a wedge angle of 14 degree to align the shock wave with the midpoint of the plate.The 14° wedge angle was specifically chosen to produce a shock-boundary layer interaction (SBLI) for the FTSI study. While lower angles were avoided because the oblique shocks often get buried in the boundary layer, higher angles were also excluded to prevent massive flow separation and numerical crashes during the explicit coupling. At this 14° threshold, a well-defined separation bubble and a localized region of negative wall shear stress are generated, which provides a solid, repeatable case for observing structural responses. Essentially, this angle was selected to find a balance between complex physics and the stability of the simulation, which is in details explained in Wedge angle selection section. All other geometry dimensions are mentioned in Table 4.10

Table 4.10: Geometric Dimensions of modified RC-19 case

Parameter	**Value (mm)**
Test section length, L_T	918
Test section width, W_T	152
Test section height, H_T	131
Rigid panel length, L_p	400
Rigid panel width, W_p	127
Rigid panel thickness, h_p	12.7,5,3

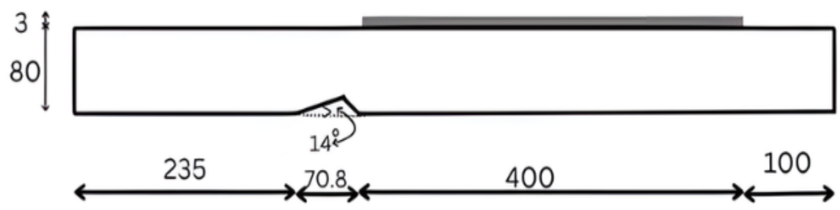

Figure 4.21: Geometry for hypersonic condition

4.2.2 Wedge anlge selection

In hypersonic flow,low angle wedge are usually avoided due to complex shock boundary layer interaction. At a low angle wedge the oblique shock generated are very close to the surface because of this the shock can lie partially or completely within the boundary layer. This violates our assumption that shock and boundary layer are treated separately. The resulting shock-boundary layer interaction creates complex flow behavior that cannot be predicted using standard analytical methods. As shock interacts with the boundary layer, former weakens considerably. Because the low-momentum fluid inside the boundary layer absorbs and diffuses the shock compression, reducing the shock intensity and weakening the pressure rise across it.As a result, viscous inviscid interaction becomes dominant, and classical inviscid oblique shock relations lose accuracy. The weakened shock also limits the ability to produce controlled shock boundary layer interactions, which are important in hypersonic aerodynamic and structural studies.

Similarly, high angle wedge is also generally avoided due to the boundary layer separation. As the wedge angle is increased pressure and temperature is increased due to strong oblique shock wave. When this strong shock impinges on the surface of the plate, the flow downstream of the shock experiences a significant adverse pressure gradient. The fluid near surface inside the boundary layer will have low momentum and when high pressure shock strike , the pressure rise is sudden. As a result, boundary layer separation occur and a shock bubble forms. This causes the flow to strike different region according to shape and size of the shock bubble.

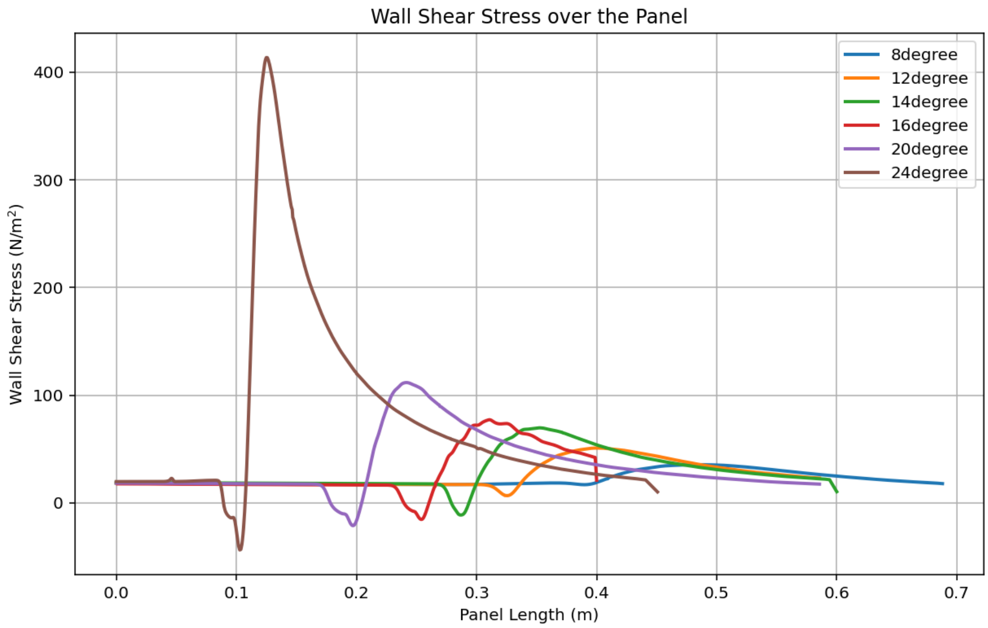

Figure 4.22: Variation of Wall Shear Stress with shock impingement location x_{ip}

Figure 4.22 shows the corresponding wall shear stress (τ_w) distribution. Negative shear stress indicates flow reversal within the separation bubble induced by the adverse pressure gradient from the impinging shock. For 8° to 12°, the shear stress remains close to zero or mildly negative, suggesting limited separation. At 14°, a clear and moderate separation region appears with a distinct negative peak, indicating the onset of significant but manageable SBLI. For 16°-20°, the separation bubble becomes substantially larger and deeper, which would result in highly nonlinear structural response and increased risk of convergence difficulties while FTSI coupling.

Upstream of separation, the wall shear stress is positive, indicating attached flow. At the separation point, the wall shear stress decreases and approaches zero. Downstream of this point, the shear stress may become negative due to flow seperation.By considering these flow characteristic in high speed flow 14° wedge angle is selected for FTSI case.

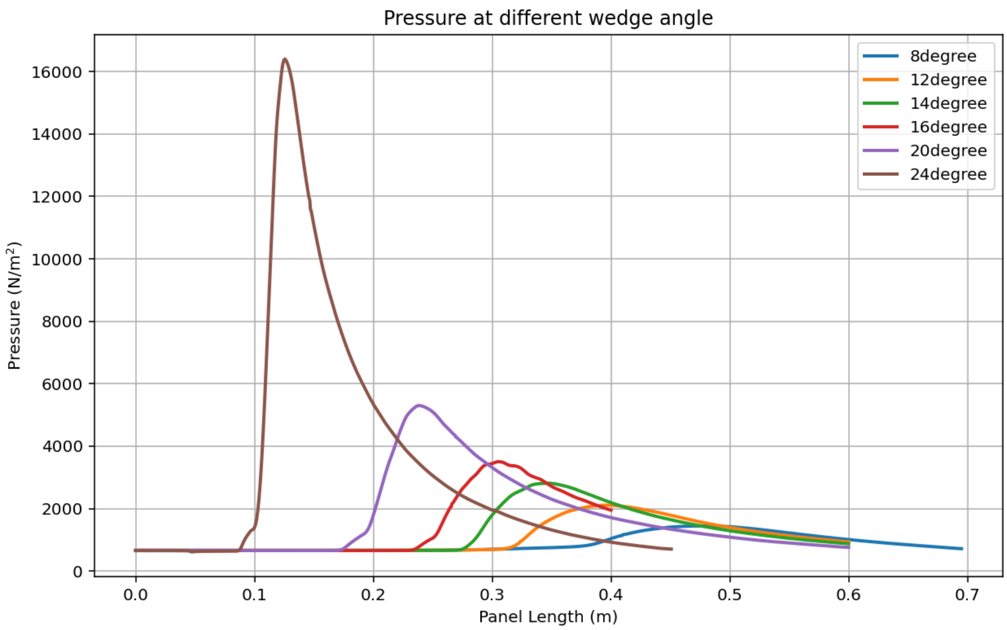

Figure 4.23: Variation of Pressure(Pa) with shock impingement location x_{ip}

Figure 4.23 presents the wall pressure distribution versus normalized streamwise distance x. The pressure profiles exhibit a characteristic peak corresponding to the shock impingement location, followed by a gradual decay in the post-shock expansion region. For smaller deflection angles (8° and 12°), the pressure rise remains moderate (peak values $\approx 1.5 - 2$ KPa), indicating relatively weak SWBLI. As the angle increases to 14°, a significantly stronger pressure peak emerges ($\approx$ 3 KPa), reflecting a more pronounced shock reflection and compression. Figure 4.23, also captures the effect of SWBLI. The pressure increases first around the separation region due to the separation shock, then a pressure plateau is formed in the recirculation region and a slight dip in pressure is observed due to the expansion fan when the flow reattaches. Finally, the pressure rises again at the reattachment point due to the reattachment shock and another pressure plateau is formed. This pressure profile is in accordance with the expected pressure distribution . At 16° and beyond the peak pressure continues to rise sharply, reaching values that would impose very high structural loading and potentially lead to numerical stiffness or instability in the coupled FSI simulation.

4.2.3 Boundary Conditions

The boundary condition for hypersonic case is obtained by modification of supersonic rc 19 case so that flow condition meets real flow condition of hypersonic aircraft shown in Table 4.4. The flow duration is assumed to be 100 milliseconds with a Reynolds number unit of 6.347×10^6 m^{-1}.

4.2.4 Meshing

The mesh shown in Figure 4.24 was generated using `blockMesh`, with a first layer thickness of 1×10^{-5} m, ensuring a near-wall resolution of $y^+ \approx 1$. Wall boundaries were applied at both the top and bottom surfaces to accurately capture the boundary layer effects. The central region of the domain was meshed more coarsely to reduce the overall cell count while maintaining computational efficiency. The mesh presented in Figure 4.24 corresponds to a medium resolution grid, consisting of approximately 112,700 cells.

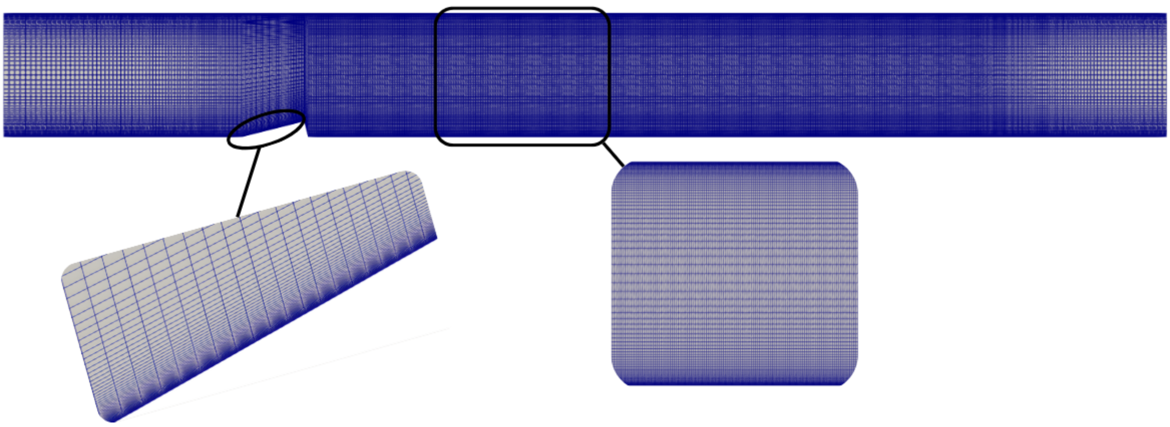

Figure 4.24: Hypersonic mesh

4.2.5 GCI

To validate the hypersonic case, three different mesh sizes:56,712, 112,700, and 225,400 elements, were utilized for the coarse, medium, and fine meshes, respectively. A constant grid refinement ratio of $r = 2.0$ was maintained between the consecutive grid levels. The shock impingement distance from the leading edge of the plate (x_{ip}, mm) was chosen as the representative convergence parameter. The calculated shock impingement locations for the coarse, medium, and fine meshes were 0.300000, 0.289000, and 0.287000 mm, respectively. Using the Grid Convergence Index (GCI) method proposed by Roache [32], the apparent order of convergence (p) was calculated iteratively and found to be 2.459431. The extrapolated shock impingement distance at an infinite grid resolution was $x_{ip} = 0.286556$ mm. The asymptotic ratio of convergence was evaluated to be 0.993080. Since this value is very close to 1.0, it confirms that the solutions lie well within the asymptotic convergence range and that the applied mesh refinement is sufficient to achieve grid independent results[4.25]. From the GCI study, the discretization error between the medium and coarse mesh was 1.057286%[4.11], while the error between the fine and medium mesh dropped to just 0.193573%[4.11]. Since the medium mesh already provides excellent accuracy while saving significant computational time compared to the fine mesh, the medium mesh consisting of 112,700 elements was selected for all further simulations.

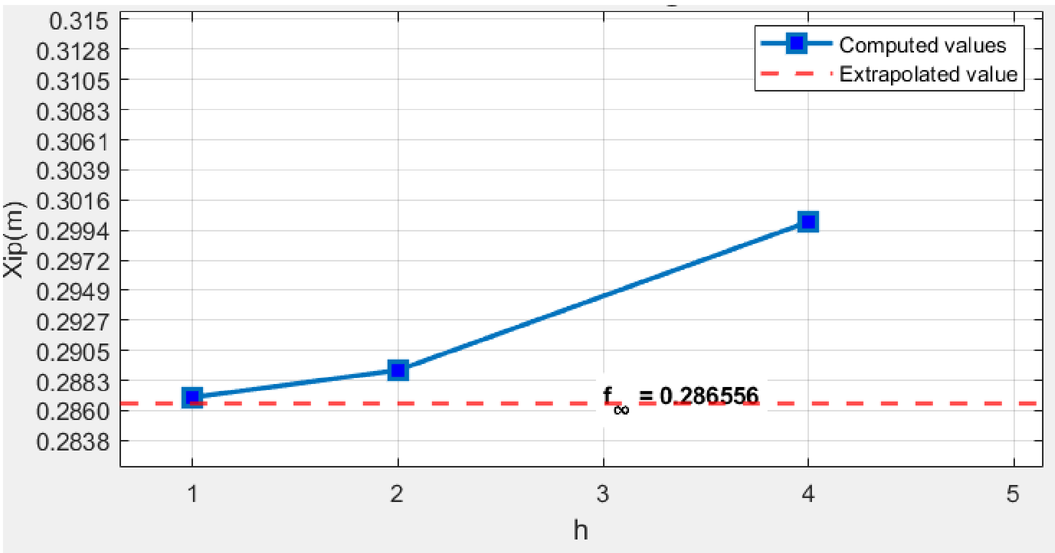

Figure 4.25: Variation of shock impingement distance (x_{ip}) with Grid refinement Factor (h)

Table 4.11: Mesh Independence Study for RC-19 Benchmark Case

Mesh	**No. of Elements**	x_{ip}	**Relative error** (η%)	**GCI** (%)
Coarse	56712	0.300	4.69	1.06
Medium	112700	0.289	0.85	0.19
Fine	225400	0.287	0.16	–

4.3 Low Fidelity Modeling

In Low Fidelity Modeling, the solver developed by previous researchers was modified to account for the transient pressure on top of the plate. The existing solver had already been verified for the HyFoil experiment. The plate is represented as a clamped clamped beam using the Euler–Bernoulli beam model.

The pressure on the upper surface of the plate is fixed as cavity pressure, assuming a flat plate geometry. The pressure on the lower surface of the plate is assumed to be equal to the freestream pressure, which is 620.7 Pa.

The deflection of the plate is calculated by solving the governing differential equation using the `ode45` function in MATLAB. In addition, the pressure on the top surface of the deflected plate is obtained by applying piston theory.

4.3.1 Shock Expansion Theory

The time varying pressure on the top surface of the plate, caused by the oscillating shock generator, was obtained using shock-expansion theory. The pressure acting on the plate surface was calculated for the undeformed plate using the θ-β-Mach relation. The geometry of the expansion fan was determined using the Prandtl-Meyer equation. The plate was divided into three regions based on the interaction of the shock wave and expansion fan. Region 1 has pressure equal to the freestream pressure (620.7Pa). Region 2 is characterized by the pressure after the reflected shock. Region 3 is the region where expansion fan and shock wave interaction occurs. The pressure distribution was estimated by dividing the flat plate into 250 equal segments along its length.

Comparison of Pressure Distribution The time-varying pressure distribution along the plate length was determined using shock-expansion theory. The predicted pressure distribution was compared with the results obtained from inviscid FSI simulations to analyze discrepancies between analytical and numerical approaches.

4.3.2 Finite Element Method

The second order ordinary differential equation governing the structural dynamics was converted into a first order state-space form. The equation was then solved using MATLAB's `ode45` solver to determine the displacement of the finite element nodes along the plate.

4.3.3 Piston Theory

The pressure distribution on the upper surface of the flat plate after deformation was calculated using second-order piston theory.This theory was applied at every time step except the initial step, where the plate was considered undeformed.The input parameters used in piston theory include local pressure, local Mach number over the flat plate element, and inclination angle of the element.The output of the piston theory calculation is the updated pressure acting on each plate element after deformation. This updated pressure is then used to compute the displacement in the next iteration.

4.3.4 CFD Enriched Piston Theory

To enhance the accuracy of the low-fidelity model, a CFD-enriched piston theory approach was implemented. In this method, initial flow parameters such as temperature (T), pressure (P), velocity (U), and spatial coordinates (X) were obtained from high-fidelity CFD simulations and imported in the form of a CSV file. The pressure and Mach number distributions were extracted specifically from the lower surface of the plate. To ensure a stable and representative input for the model, the pressure data was spatially averaged over 26 discrete elements along the plate. These averaged pressure values were then coupled with the structural displacement obtained from the structural solver. Using piston theory, the aerodynamic pressure on the deformed plate was recalculated based on this updated geometry. The newly computed pressure distribution was subsequently used to determine the structural response (displacement) for the next iteration. This iterative coupling process continues until a converged solution is achieved, thereby improving the overall prediction accuracy compared to the conventional piston theory approach.

4.4 High Fidelity Modeling

For more accurate results, we used an HFM, where the simulation is broken down into specialized parts that work together. The components include:

(i) **Fluid Solver:** `rhoCentralFoam` in OpenFOAM solves compressible flow using Navier Stokes, energy, and continuity equations.

(ii) **Thermo structural Solver:** Coupled thermomechanical analysis is achieved via the coupled temperature-displacement step in `CalculiX`, which simultaneously solves the non-linear dynamics of displacements and temperature.

(iii) **Coupling Interface:** `preCICE` allows the solvers to exchange data such as pressure, temperature, and displacement during the simulation.

(iv) **Meshing Tools:** `blockMesh` and `snappyHexMesh` are used for the fluid region, while `Gmsh` creates the mesh for the structural domain. The mesh adjusts dynamically using the `displacementLaplacian` solver.

4.5 Case Setup

Open source platforms were preferred instead of commercial software because they are freely available and provide greater flexibility through modifiable features. Access to their publicly available source code also allows users to better understand the working of the software.

4.5.1 Fluid Thermal Case Setup

OpenFOAM includes a structural solver that is based on the Finite Volume Method (FVM). However, for structural simulations, the Finite Element Method (FEM) is generally considered to provide higher accuracy than FVM. In partitioned fluid thermal structure interaction (FTSI) frameworks, it is a common approach to use FVM for fluid computations and FEM for structural analysis. For this reason, a structural solver based on FEM from CalculiX was adopted.

CalculiX is an open-source Finite Element Analysis (FEA) tool developed for structural mechanics applications. It can also be employed in FTSI simulations by coupling its structural solver with a fluid dynamics solver. The software is three-dimensional in nature and supports both linear as well as nonlinear analyses. Moreover, it can be integrated with OpenFOAM solvers without significant difficulty for partitioned FSI problems. Therefore, CalculiX was selected as the structural solver in this work.

4.5.1.1 Solution Methods and Tolerences

In the inviscid case, the conserved quantities (ρ,ρU, and ρE) were calculated explicitly using a diagonal solver. The velocity field along with the energy equation was solved using the smoothSolver, with Gauss Seidel used as the smoothing technique to reach the specified convergence criteria. The mesh motion (cell displacement) was resolved using the GAMG approach. A tolerance of 1×10^{-9} with a relative tolerance of zero was imposed for both velocity and energy, whereas for cell displacement the tolerance was fixed at 1×10^{-8} with a relative tolerance of zero.

A similar strategy was followed for the viscous case, where ρ,ρU, and ρE were again computed explicitly via a diagonal solver. The velocity and energy fields were obtained using smoothSolver with Gauss–Seidel smoothing to satisfy the convergence criteria. However, for mesh motion, smoothSolver combined with a symmetric Gauss–Seidel smoother was employed. The convergence settings were tightened for the viscous solution: 1×10^{-11} (with zero relative tolerance) for velocity, 1×10^{-10} (with zero relative tolerance) for energy, and 1×10^{-8} with a relative tolerance of 1×10^{-4} for cell displacement.

4.5.1.2 Dynamic Mesh

Dynamic mesh control remained one of the major challenges in FTSI simulations. During the simulation, the interface mesh needed to deform smoothly without excessive distortion, as poor mesh quality could degrade solver performance or even lead to failure. The dynamic mesh configuration was defined in the dynamicMeshDict file within the fluid case, where both the mesh motion solver and mesh diffusivity were specified. The motion solver handled the cell movement based on prescribed boundary motion, while the diffusivity controlled how mesh points were redistributed at each time step.

OpenFOAM provided several mesh motion solvers, but only displacement-based solvers were compatible with preCICE coupling in this study. Therefore, the displacementLaplacian solver was selected, which determined mesh motion by solving a Laplacian equation for displacement.

$$\nabla \cdot (\lambda_{dm} \nabla) = 0 \tag{4.46}$$

$$\lambda \propto \frac{1}{l^2} \tag{4.47}$$

The diffusivity was defined as a quadratic inverse function of the distance from the plate, meaning it decreased rapidly away from the plate. In simple terms, outer cells underwent more deformation, while cells near the plate remained nearly rigid. This approach helped preserve the fine boundary layer mesh and prevented issues such as mesh distortion or negative cell volumes.

4.5.2 Solid Case Setup

OpenFOAM has its own structural solver based on the Finite Volume Method (FVM). However, the Finite Element Method (FEM) is generally regarded as more accurate for structural simulations. In partitioned fluid structure interaction (FSI) approaches, it is common practice to apply FVM for fluid analysis and FEM for structural analysis. Therefore, an FEM based solver from CalculiX was used.

CalculiX is an open source Finite Element Analysis (FEA) software designed for structural mechanics simulations, and it can also be applied to FSI problems by coupling its structural solver with a fluid dynamics solver.It is also capable of incorporating temperature effect in structure, converting FSI setup to FTSI setup. It is a three dimensional code capable of handling both linear and nonlinear analyses. Additionally, this solver can be readily coupled with OpenFOAM solvers for partitioned FTSI simulations. Hence, CalculiX was chosen as the structural solver for this study.

4.5.2.1 Discretization

A quadrilateral mesh of size 1 mm was generated using Gmsh software.

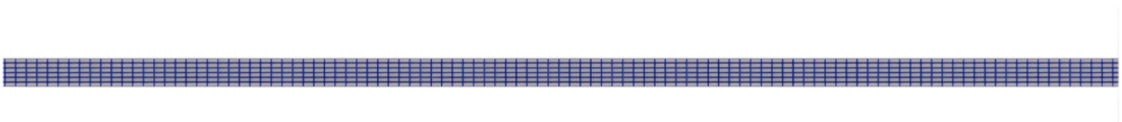

Figure 4.26: Discretizations of Solid

4.5.2.2 Material Properties and Boundary Conditions

All boundary conditions and input parameters were defined in the CalculiX .inp file. A fixed support was applied at both the end of the plate to make it clamped clamped case by restricting motion in all degrees of freedom at those nodes. The remaining nodes were free to move, except in the z-direction, since the problem was treated as a 2D case.

Table 4.12: Material Properties of Structure

Material Properties	**Value**
Density	2670 kg/m^3
Young's Modulus	5.27 GPa
Poisson's Ratio	0.33
Rayleigh Damping Coefficients	$\alpha = 3.7065,\ \beta = 1.851 \times 10^{-6}$

4.5.2.3 Modal Analysis

Modal analysis was performed to extract the first two natural frequencies and mode shapes of the clamped-clamped panel of length=400mm,width=127mm and thickness=3mm, which are needed to compute the Rayleigh damping coefficients. As shown in Figure 4.27, the first mode, f = 90.71 Hz, takes on a smooth symmetric bow shape with both ends held fixed, while the second mode, f = 250.04 Hz, shows an antisymmetric shape with one interior crossing point. The third mode, f = 490.19 Hz, exhibits a more complex shape with two interior nodes and alternating positive and negative deflection regions across the panel. These mode shapes behave exactly as expected for a clamped-clamped panel, confirming the validity of the finite element model.

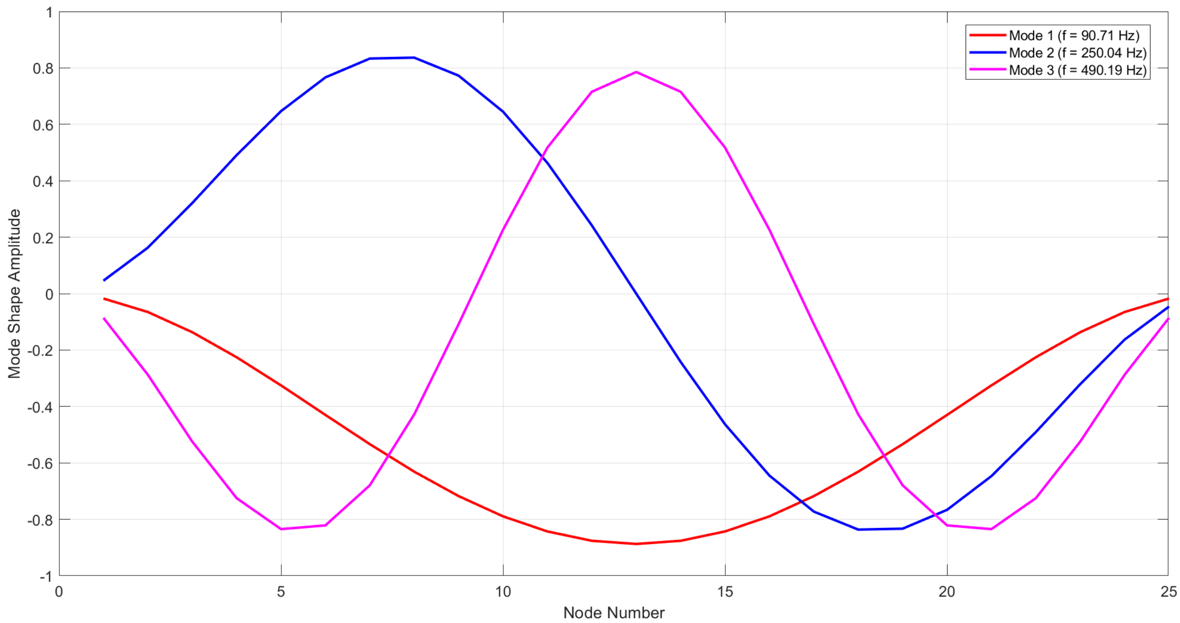

Figure 4.27: 1^{st}, 2^{nd}, and 3^{rd} Mode of Vibration

4.5.2.4 Discretization and solution Method

Spatial discretization in the CalculiX linear solver was carried out using the Finite Element Method (FEM), while the time domain was discretized into small increments using an explicit time integration scheme. After this discretization process, the resulting equations were solved using the Spooles solver.

4.5.3 FTSI Coupling Setup

The coupling numerics were specified in the precice-config.xml file. A serial explicit coupling scheme was used with fluid as the first participant and solid as the second participant. For the FTSI cases, the coupling time was set to 0.002 ms to mitigate mesh distortion and negative cell volume by ensuring smaller deformations and temperature gradients at each step. Before starting the FTSI simulation, a steady state solution for fluid flow was obtained through fluid-only simulation to serve as the initial condition. During the FTSI simulation, the fluid solver runs until the coupling time and then maps both the force and heat flux data to the nodes of the structure mesh using the nearest-neighbor mapping algorithm. Now, the CalculiX solver calculates the displacement and temperature distribution of nodes and then maps the displacements and temperatures back to the fluid mesh using the same mapping algorithm. This continues until all the coupling steps are completed.

CHAPTER FIVE: RESULTS AND DISCUSSIONS

The aerothermoelastic results from both low fidelity and high fidelity models are discussed in this section. The results include mid-point displacement history, peak pressure evolution as well as the dynamic nature of SWBLI region.

5.1 Supersonic Case Results

5.1.1 Plate mid-point displacement

Figure 5.28 shows the deflection of the compliant panel due to the shock impingement on it over the time. The plate undergoes oscillatory motion with the displacement reaching a maximum value of approximately 35 μm. These oscillations have exhibited a gradual decay in amplitude, which suggests the presence of damping within the system.

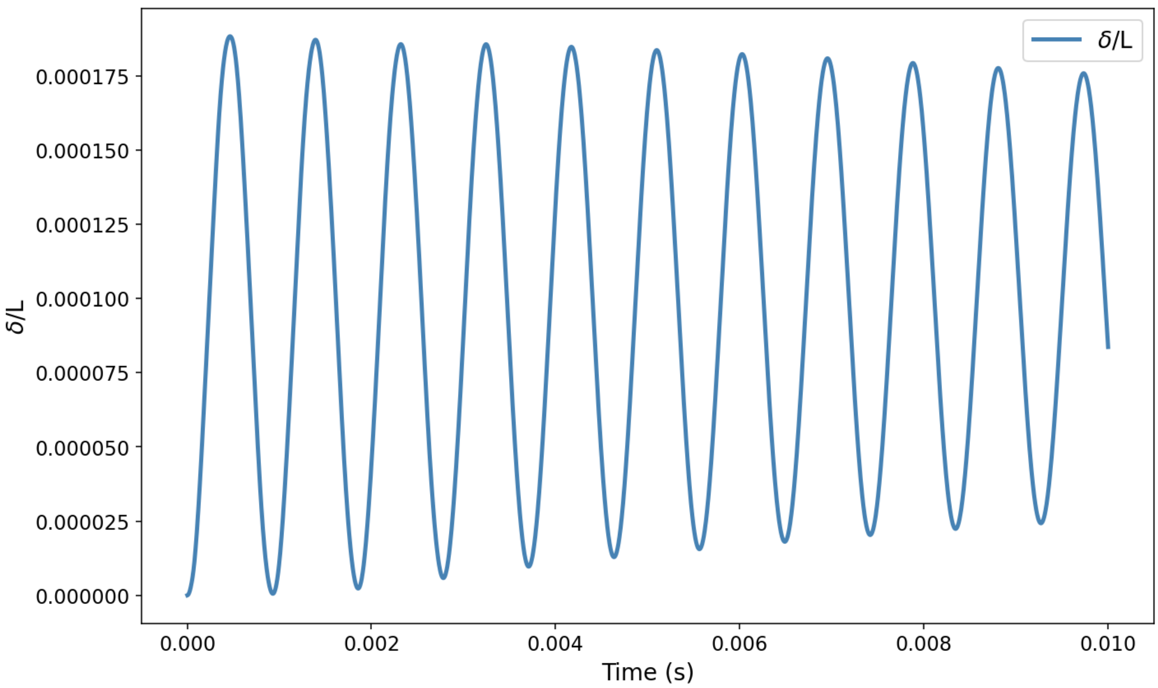

Figure 5.28: Plate mid-point displacement over the time

5.2 High Fidelity Modeling (HFM)

In this section, the results of the hypersonic fluid-thermal-structure interaction (FTSI) simulations are presented. A comparative analysis between inviscid and viscous flows, as well as laminar and turbulent models, is also carried out. A serial explicit coupling scheme is employed for the simulations, as the mean plate deflection differs by only 1.36% compared to the serial implicit approach. However, the explicit coupling method offers significantly better computational efficiency, requiring approximately 2.6 times less computational time [29].

5.2.1 Shock Wave Boundary Layer Interaction Effects on Panel

Figure 5.29 and Figure 5.30 clearly illustrate the Shock Wave Boundary Layer Interaction (SWBLI) in both hypersonic and supersonic flows. In a perfect, inviscid supersonic flow, disturbances cannot travel backward against the flow. However, real-world flows have viscosity. Because the fluid must stick to the wall (the no-slip condition), there is always a thin layer of slow, subsonic flow right next to the panel's surface. When a shock wave hits this boundary layer, it creates a sudden and severe rise in pressure (an adverse pressure gradient). Because the fluid near the wall is subsonic, this high pressure can actually travel upstream against the flow. The slow moving fluid near the wall does not have enough energy to push through this sudden high pressure. As a result, it slows down, stops, and peels away from the panel, creating a pocket of trapped, swirling air known as a recirculation bubble. This separated bubble acts like a physical ramp on the surface of the panel. When the incoming high speed air hits this 'aerodynamic ramp', it is deflected outward. This sudden outward turn creates a new shock wave, called the Separation Shock, which forms well before the original shock wave actually hits the surface. As the flow travels over the top of the recirculation bubble, the original incident shock interacts with the separated flow. Eventually, the flow is forced to bend back downward toward the panel. When the flow hits the surface and reattaches, it has to abruptly straighten out to run parallel to the wall again. This sharp turn generates another shock wave, known as the Reattachment Shock. Finally, after passing through this complex system of shocks (incident, separation, and reattachment) and the resulting expansion waves, the flow finds a favorable pressure gradient and flattens out into a normal boundary layer once again [5.29, 5.30]. The exact locations of where the flow separates and reattaches can be pinpointed by looking at the wall shear stress (Figure 5.31). In the highlighted recirculation region, the shear stress briefly drops below zero, indicating that the flow is moving backward inside the bubble. Because the separated region in this specific case is relatively small, its detailed impact is somewhat smoothed out in the overall pressure distribution plot (Figure 5.32). However, the general trend follows expected aerodynamic behavior: the pressure begins to climb near the separation point due to the separation shock. It then temporarily levels out (forming a plateau) over the recirculation zone. As the flow turns back and reattaches, there is a minor dip in pressure caused by expansion waves, followed by a final, sharp pressure spike caused by the reattachment shock.

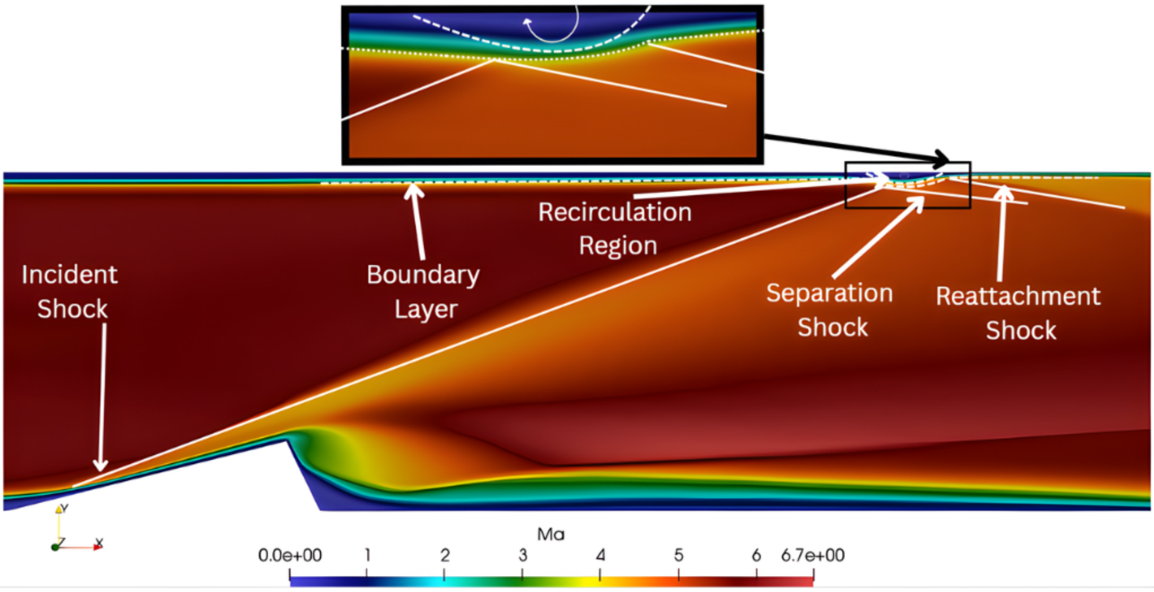

Figure 5.29: Mach Contour for Hypersonic Case

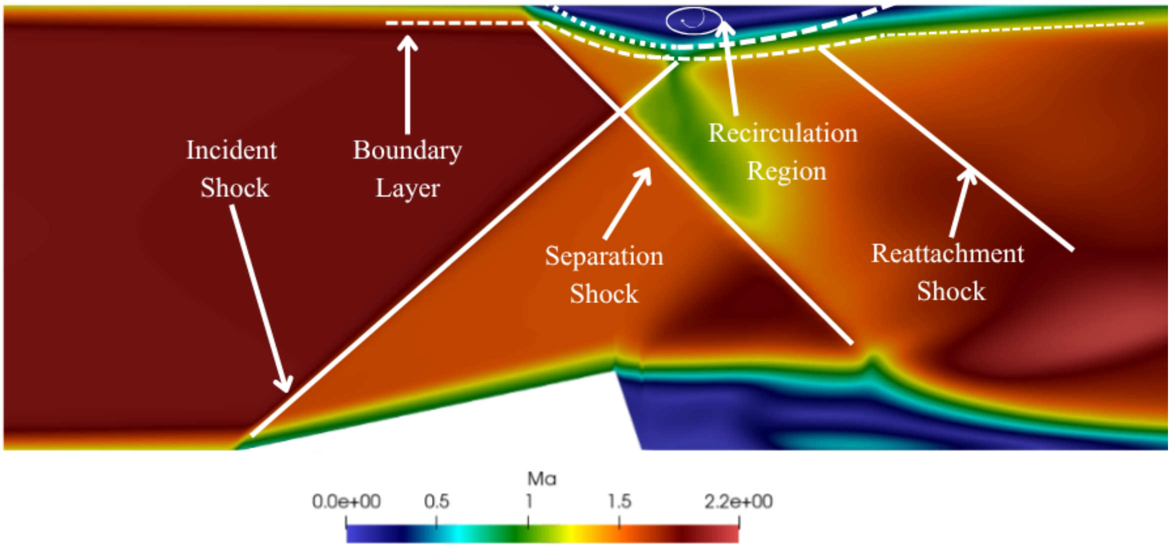

Figure 5.30: Mach Contour for Supersonic Case at wedge angle 8°

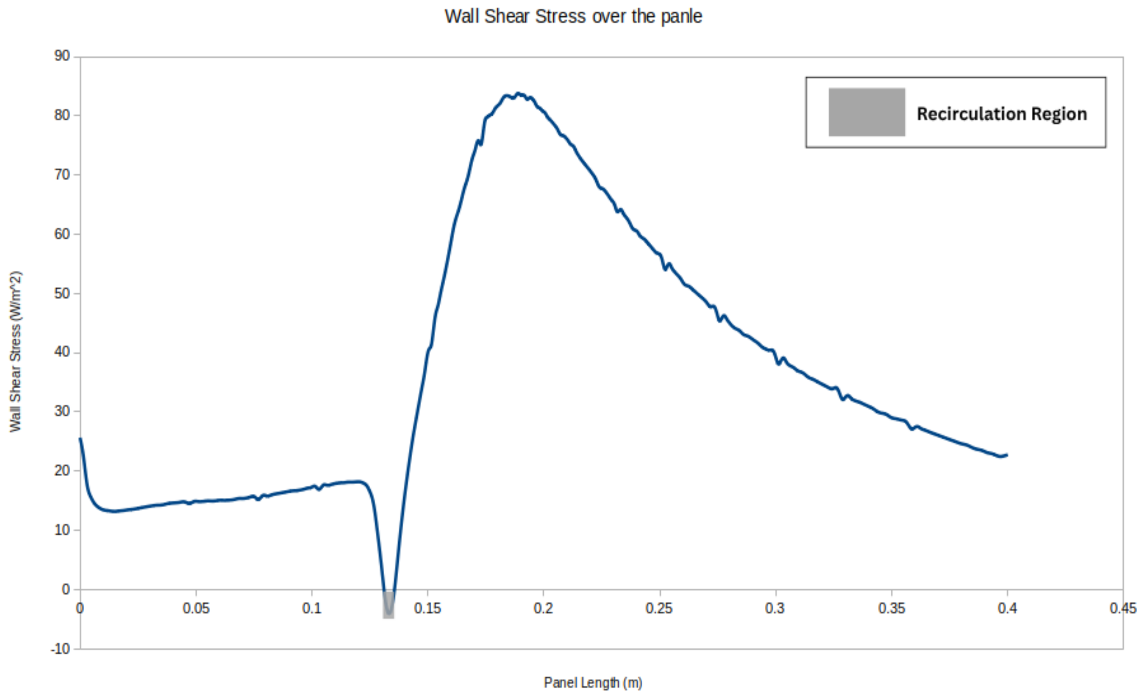

Figure 5.31: Shear Stress Profile indicating flow separation (time = ms)

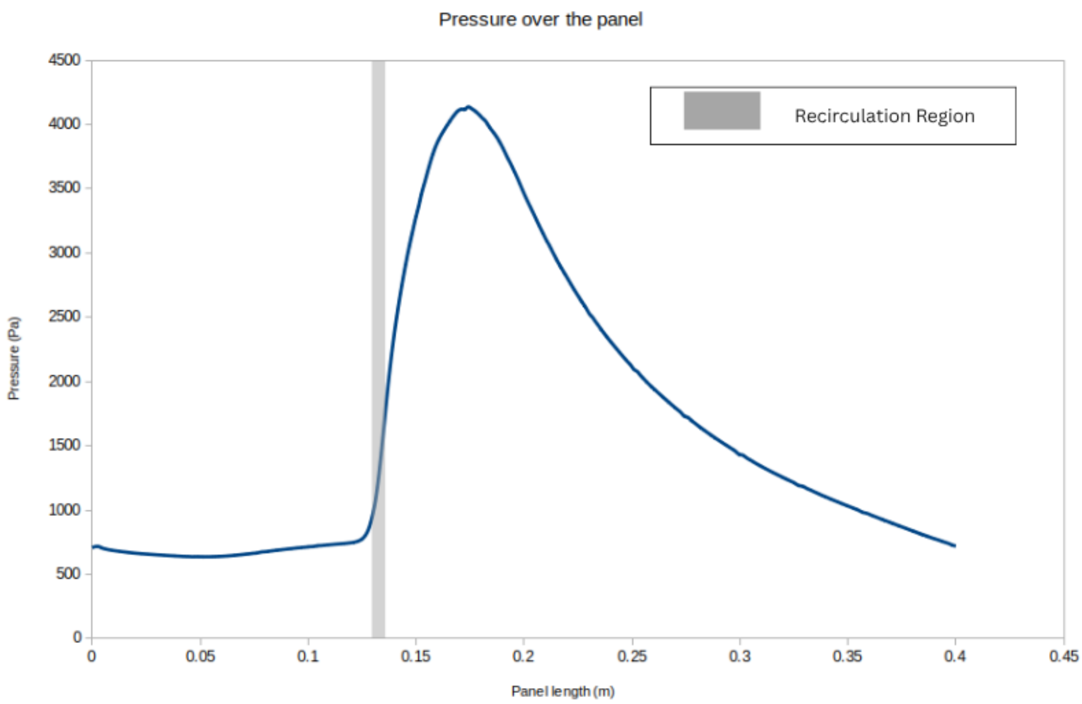

Figure 5.32: Pressure Distribution Over Clamped-Clamped Panel (time = ms)

5.2.2 Viscous FTSI

Viscous FTSI plays vital role in studying the complex boundary layer phenomenon such as surface shear stresses and aerodynamic heating due to skin friction and shock wave impingements

5.2.2.1 Displacement Analysis

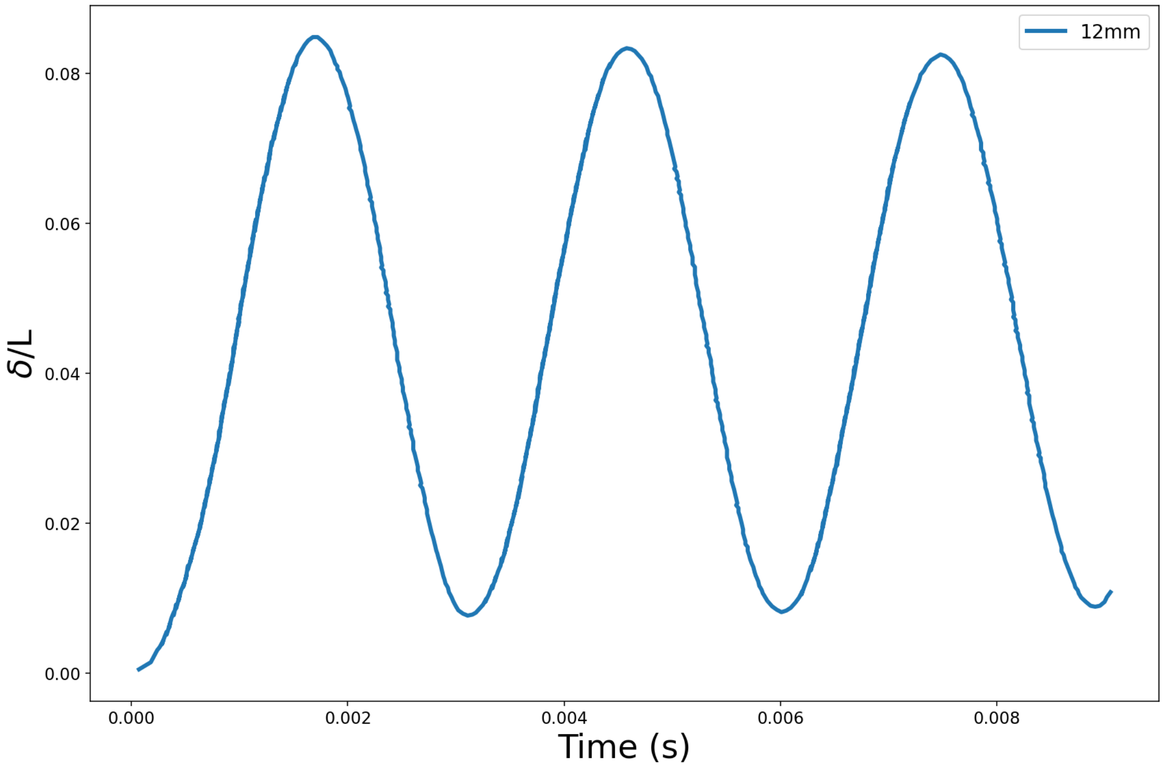

Figure 5.33: Mid-point Displacement for the palate of 12 mm thick

Figure 5.33 shows the time history of displacement at the mid-point of the 12 mm thick plate under shock impingement. The plate undergoes oscillatory motion, with the displacement reaching a maximum value of approximately 34 μm. Although the plate clearly responds to the aerodynamic loading, this amplitude is extremely small. Such a tiny deflection makes it very difficult to observe meaningful changes in the plate's structural behavior, thermal response, or the interaction between the shock wave and the boundary layer. Because the deformation is so limited, important physical phenomena such as the growth of the separation bubble, changes in shock impingement location, and the resulting variation in heat transfer remain almost undetectable. To overcome this limitation and generate a stronger fluid-structure-thermal interaction, the plate thickness was reduced in subsequent simulations. A thinner plate is more flexible, allowing larger displacements and more pronounced vibrations. This enables us to clearly study how the shock affects the plate's deformation, its material properties, the dynamic behavior of the separation bubble, and the resulting heat transfer characteristics.

After analyzing the 12 mm thick plate, which exhibited very small displacement, the plate thickness was reduced to 5 mm to amplify the structural response and enable a stronger fluid-structure-thermal interaction. Figure 5.34 presents the time history of displacement at the mid-point of the 5 mm thick plate. It can be clearly observed that the thinner plate undergoes significantly larger oscillations compared to the 12 mm case. The displacement amplitude reaches approximately 0.4 mm (about 15 times larger than the 12 mm plate), and the motion shows a sustained periodic oscillation throughout the simulation time. This substantial increase in displacement amplitude indicates that reducing the plate thickness makes the structure much more flexible, allowing it to respond more vigorously to the aerodynamic pressure loading caused by the shock impingement. The larger deformation alters the local flow field more noticeably, which is expected to influence the shock-boundary layer interaction, the size and dynamics of the separation bubble and the resulting heat transfer distribution over the panel surface. The oscillatory behavior also suggests that the plate is vibrating predominantly in its fundamental mode.

A characteristic decaying oscillatory behavior is observed, which indicates damping effect arise from either structural or fluid-induced sources. Within the 0.065 s duration, approximately eleven full cycles are recorded, through which a consistent fundamental frequency is maintained. A gradual reduction in peak displacement amplitude is noted, with the initial value of 0.001 decreasing to approximately 0.0008 by the final cycle. It is therefore confirmed that while the oscillation remains sustained, the energy within the first mode of deformation is slowly dissipated over time.

Although the 5 mm thick plate showed significantly larger displacement compared to the 12 mm case, the maximum deformation was still limited to approximately 1 mm. This level of deflection was found to be insufficient to produce strong fluid-structure interaction effects. In particular, the changes in the local flow field remained relatively small, resulting in limited variation in the separation and reattachment points of the flow. Consequently, the dynamic behavior of the separation bubble and its interaction with the moving shock could not be studied in detail. To further amplify the structural response and generate more pronounced aero-thermo-elastic coupling, the plate thickness was reduced to 3 mm. Figure 5.35 shows the time history of displacement at the mid-point of the 3 mm thick plate. It can be observed

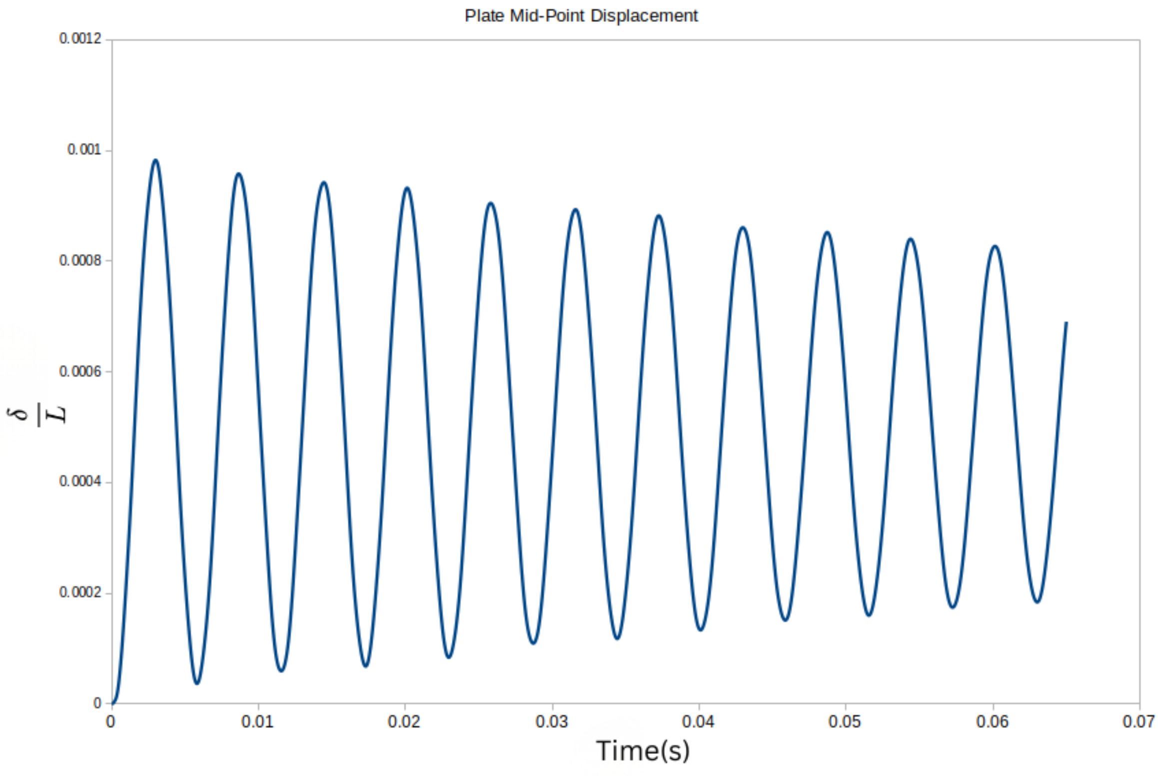

Figure 5.34: Mid-point Displacement for the plate of 5mm thick

that the thinner plate exhibits even larger oscillations, with the displacement amplitude reaching nearly 1.75 mm. The plate now vibrates with a clear periodic motion, indicating a much stronger response to the aerodynamic loading induced by the shock impingement. This increased flexibility allows the panel to interact more significantly with the surrounding flow. Larger deformations are expected to cause noticeable movement of the shock impingement location, substantial changes in the size and dynamics of the separation bubble, and stronger variations in wall heat flux and pressure distribution over the panel surface. These effects are essential for understanding the coupled behavior in hypersonic fluid-thermal-structural interaction problems. As shown in the Figure 5.35, a clear oscillating pattern was observed, where the δ/L initially reached a peak of approximately 0.004. Over time, these oscillations have exhibited a gradual decay in amplitude, which suggests the presence of damping within the system. This behavior was recorded to ensure the stability of the panel under the simulated conditions.

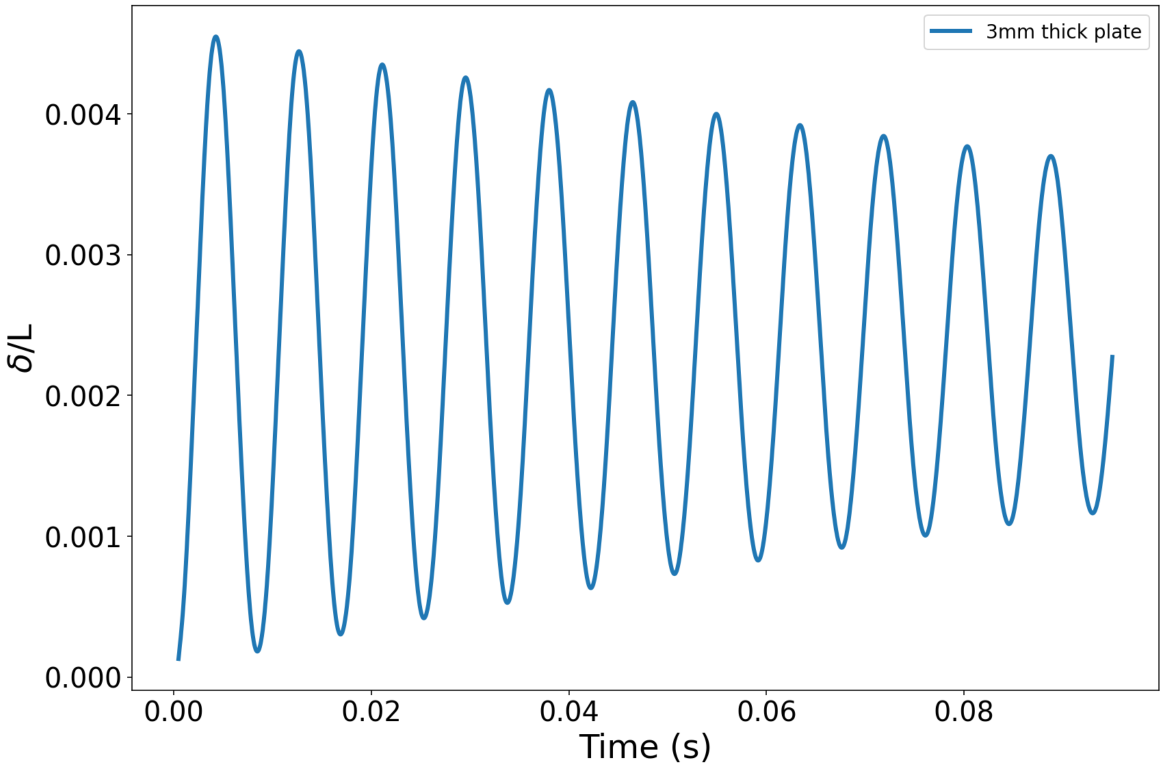

Figure 5.35: Mid-point Displacement for 3 mm thick plate

5.2.2.2 Velocity Analysis

Figure 5.36 presents the of the y-velocity (transverse velocity) at the mid-point of the panel at which the plate vibrates during the coupled Fluid-Thermal-Structure Interaction simulation. The plot reveals a highly periodic oscillatory behavior with a dominant frequency corresponding to the first natural mode of the panel. The y-velocity oscillates between approximately +0.65 m/s and -0.65 m/s, showing a nearly sinusoidal pattern with gradual amplitude decay over time. This decay is attributed to structural damping (Rayleigh damping) and energy dissipation through aerodynamic loading and thermal effects. The maximum velocity magnitude occurs near the instants of zero displacement (when the panel is moving fastest), which is consistent with simple harmonic motion characteristics. The periodic nature of the y-velocity confirms that the panel is undergoing limit cycle oscillation (LCO) dominated by its first bending mode. The close agreement between the observed oscillation frequency and the natural frequency of the plate (as reported in previous sections) indicates strong fluid-structure coupling, where aerodynamic forces sustain the oscillation while structural and thermal effects provide damping. This velocity response is critical because it directly influences the rate of change of panel displacement, which in turn affects the local shock

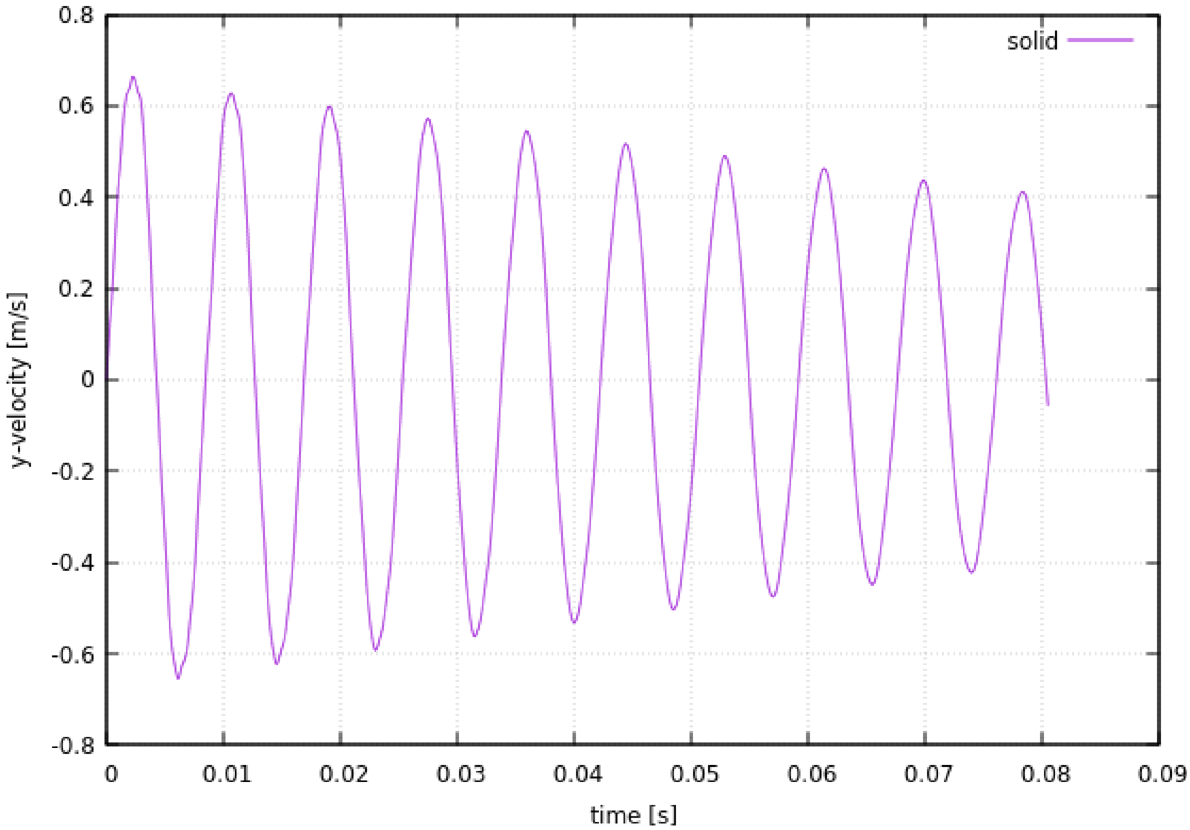

Figure 5.36: Mid-point vertical velocity of 3 mm thick plate

impingement location, separation bubble dynamics, and the resulting aerodynamic heat flux and pressure loading on the panel. The FFT of mid-point deflection of 3mm plate with time is shown in Figure 5.37. The Fast Fourier Transform (FFT) of the mid-point deflection over time is presented in Figure 5.37 , where the Power Spectral Density (PSD) is plotted against frequency. A dominant peak is observed at 118.28 Hz, which signifies the primary frequency of oscillation for the plate under the given conditions. This peak frequency is identified as being significantly higher than the natural frequency of 90.71 Hz, which is indicated by the red dashed line. Such a shift suggests that the oscillation is influenced by external flow conditions or fluid structure interaction effects beyond simple free vibration. Furthermore, the broad, lower intensity spectral distribution across higher frequencies is noted, representing secondary noise or minor turbulent fluctuations in the system.

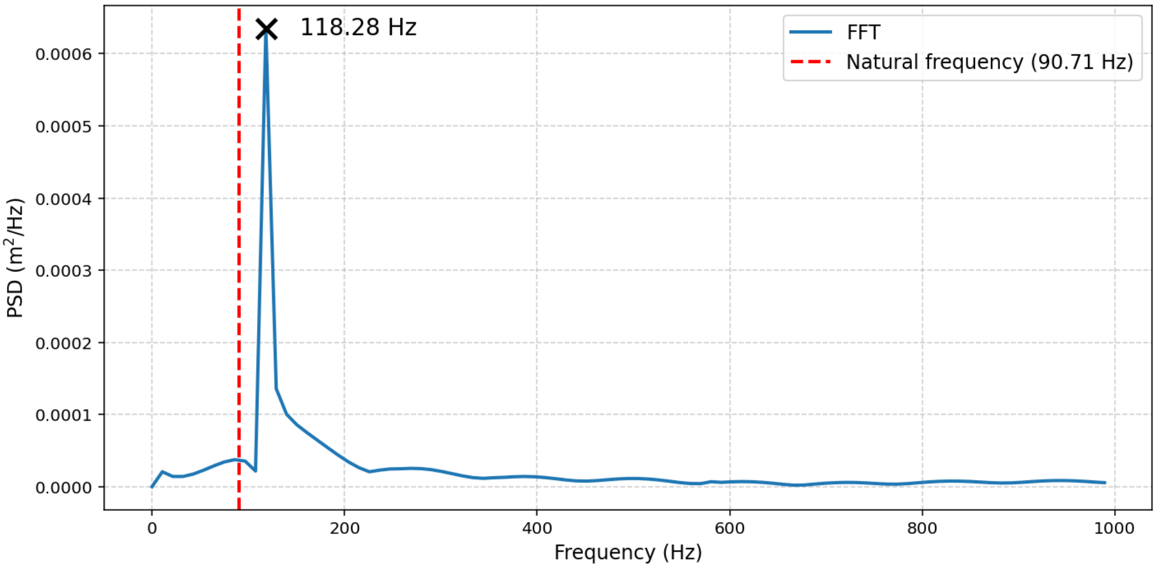

Figure 5.37: FFT of Mid-Point Deflection with Time

5.2.2.3 Peak Pressure Analysis

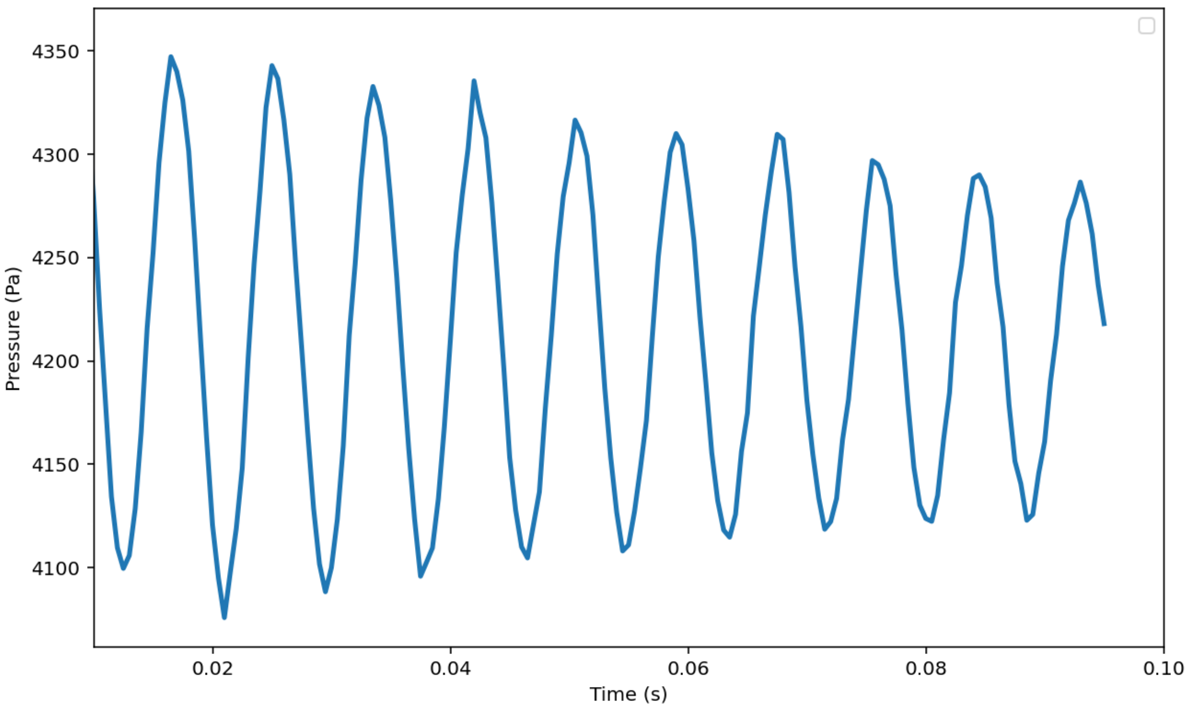

Figure 5.38: Peak Pressure Evolution with Time (Viscous)

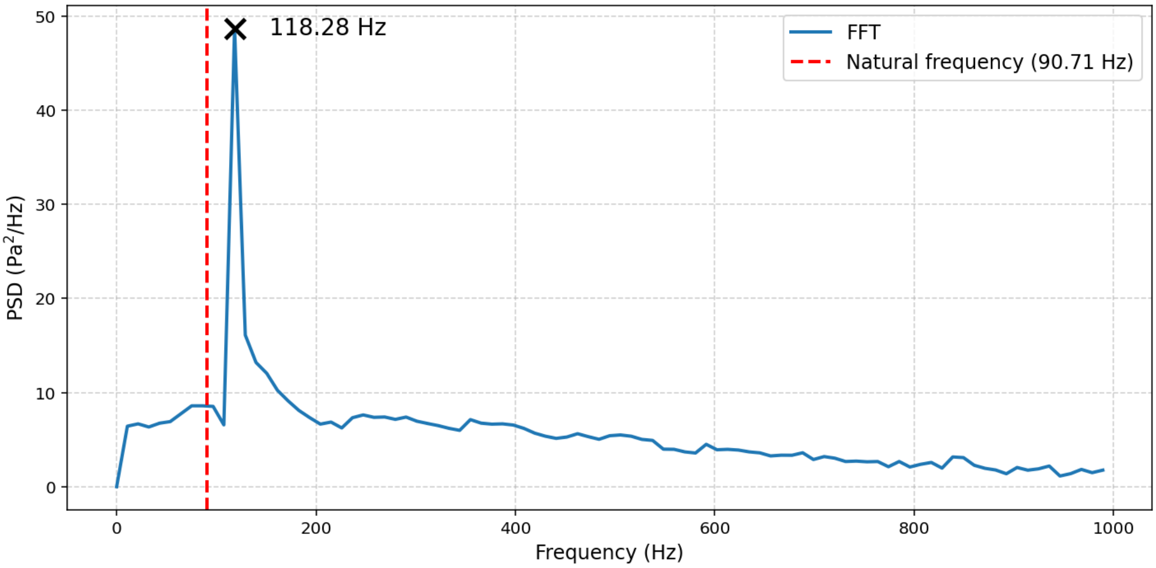

Figure 5.39: FFT of Mid-Point pressure with Time

Figure 5.38 shows the time history of peak pressure result given by the two-way viscous FTSI simulation. A single distinct modes can be clearly seen in the oscillation of peak pressure with time. The Fast Fourier Transform (FFT) of peak pressure history shown in Figure 5.39 indicates that the first peak occurs around the plate's first mode. The maximum displacement of the mid-point of the plate is 1.75 mm for a 3 mm thick pate with an oscillation frequency of 118.28 Hz. The oscillation frequency is 30.31% higher than the natural frequency of the plate deformation. Thus the oscillation is dominated mainly by the natural frequency of the plate deformation.

5.2.2.4 Thermal Response of the Plate

Figure 5.40 illustrates the evolution of the aerodynamic heat flux at the mid-point of the panel during the coupled Fluid-Thermal-Structure Interaction (FTSI) simulation. The heat flux exhibits highly dynamic behavior, characterized by an initial sharp spike followed by sustained high-amplitude oscillations. After the initial transient ($t < 0.005$ s), the heat flux stabilizes into a periodic pattern with a nearly constant mean value of approximately 27,000 W/m² and peak-to-peak oscillations of around 2,000 W/m². The periodic nature of the heat flux is directly linked to the oscillatory motion of the panel. As the panel deforms and vibrates, it continuously alters the local shock impingement location and the size of the separation bubble, resulting in fluctuating heating rates. This feedback mechanism where structural deformation influences the flow field, which in turn modifies the thermal loading, which is a critical phenomenon in hypersonic vehicles and can significantly affect the panel's

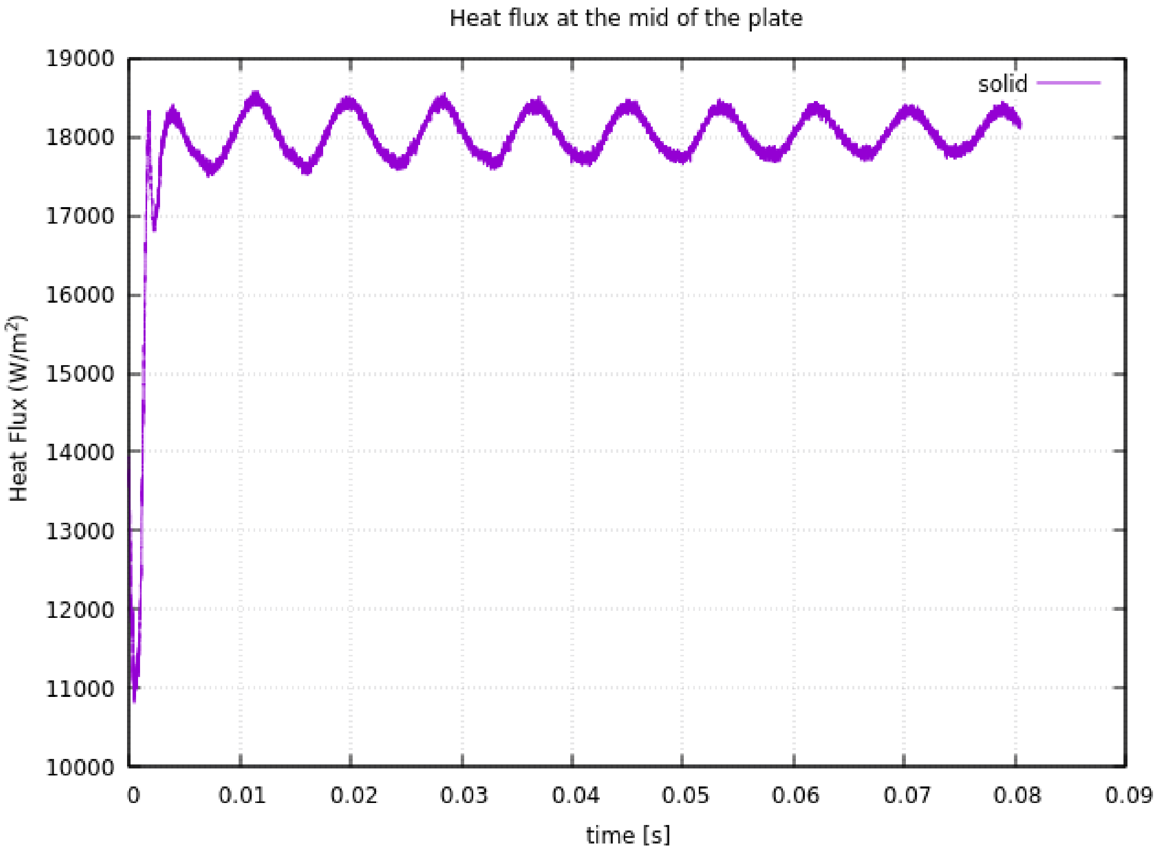

Figure 5.40: Heat Flux at the mid-point of the plate

fatigue life, thermal protection requirements, and aeroelastic stability.

Figure 5.41 presents the relationship between the local aerodynamic heat flux and the out-of-plane displacement at the mid-point of the panel during the coupled Fluid-Thermal-Structure Interaction (FTSI) simulation. The plot reveals a strong nonlinear dependence of the heat flux on the panel deformation. At very small displacements (below 0.2 mm), the heat flux remains relatively moderate. However, as the panel displaces further into the flow (between 0.2 mm and 0.6 mm), a sharp increase in heat flux is observed, rising from approximately 14,000 W/m² to nearly 27000 W/m². Beyond a displacement of around 0.6 mm, the heat flux tends to plateau, indicating a saturation effect in the shock impingement and boundary layer interaction. A distinct hysteresis loop is also visible, demonstrating that the heat flux is path-dependent, the heating experienced during the outward motion of the panel differs from that during the return motion. This behavior highlights the strong aero-thermal-structural coupling present in the system. The deformation of the panel significantly alters the local flow field, including the position of shock impingement and the size of the separation bubble, which in turn intensifies the localized aerodynamic heating. Such feedback is critical in

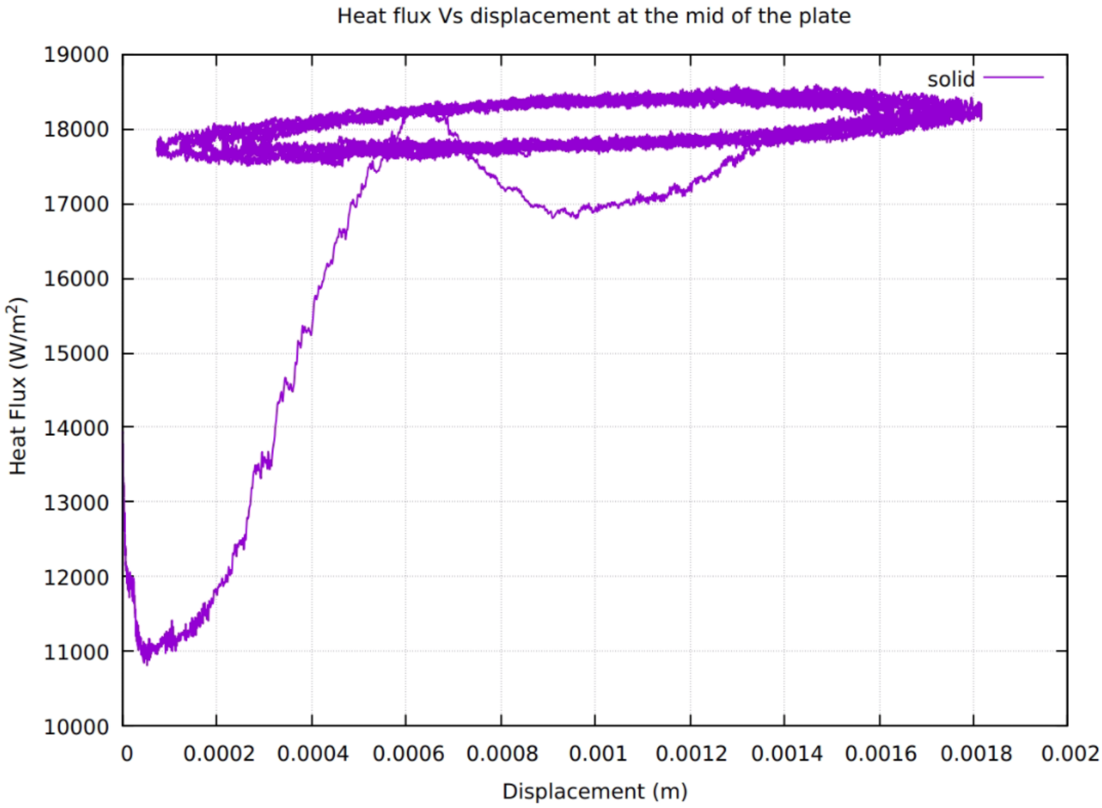

Figure 5.41: Heat Flux Vs Displacement at the mid-point of the plate

hypersonic applications as it can influence thermal protection system design, panel fatigue life and the onset of aerothermoelastic instabilities such as flutter or thermal buckling.

When the panel deforms outward (positive displacement), the heat flux at the mid-point slightly decreases due to the local flow field modification and the movement of the shock impingement point. Conversely, when the panel returns to its initial (undeformed) position, the heat flux increases again, reaching higher values. Figure 5.42 shows the spatial distribution of the wall heat flux and wall shear stress along the length of the panel at two characteristic instants: maximum and minimum panel displacement. The wall shear stress (left y-axis) exhibits a typical shock-boundary layer interaction pattern. It starts with a high value near the leading edge, drops significantly in the separation region ($x \approx 0.13$–0.14 m) and then rises sharply to a peak value of approximately 85 Pa near x = 0.19 m, corresponding to the reattachment zone. After reattachment, the shear stress gradually decreases toward the trailing edge. The shear stress profiles at maximum and minimum displacement are quite similar in shape, with only minor differences in peak magnitude. In contrast, the wall heat flux (right y-axis) shows a strong dependence on panel displacement. At the location of maximum displacement, the heat flux reaches a significantly higher peak value (33,000 W/m²) compared to the minimum displacement case (31,000 W/m²). The heat flux distribution also

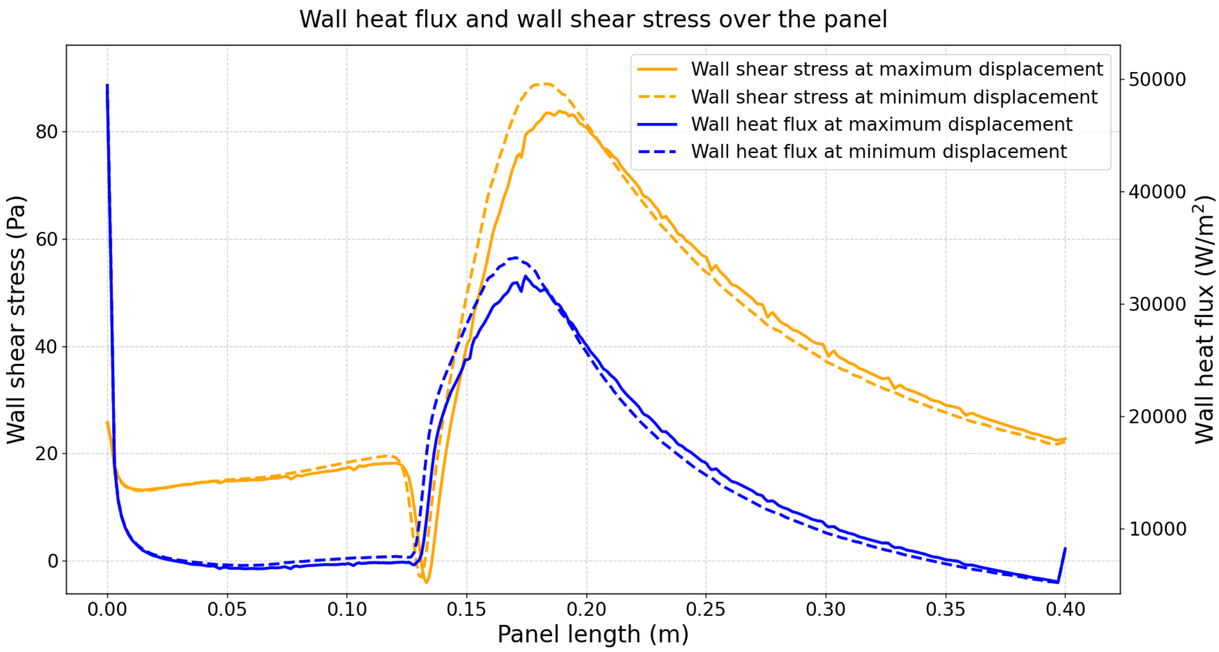

Figure 5.42: Comparison of Heat flux and Wall Shear Stress over the Panel Length at maximum and minimum displacement

reveals a pronounced peak in the reattachment region, followed by a gradual decay toward the trailing edge. The relationship between wall shear stress and wall heat flux along the panel reveals strong but complex aero-thermal coupling. While both quantities peak in the reattachment region, wall heat flux shows significantly higher sensitivity to panel deformation compared to wall shear stress. At the instant of maximum panel displacement, the peak heat flux increases notably (reaching approximately 33,000 W/m²), whereas the peak wall shear stress exhibits only marginal variation. This behavior indicates that panel deflection modifies the shock impingement location and the size of the separation bubble more strongly than the near-wall velocity gradient. Consequently, aerodynamic heating is amplified due to enhanced turbulent mixing and flow impingement at reattachment, even when changes in skin friction remain moderate. Such disproportionate response of heat flux to structural motion highlights the importance of fully coupled Fluid-Thermal-Structure Interaction (FTSI) simulations for accurate prediction of thermal loads on hypersonic panels.

5.2.2.5 Separation Bubble Dynamics

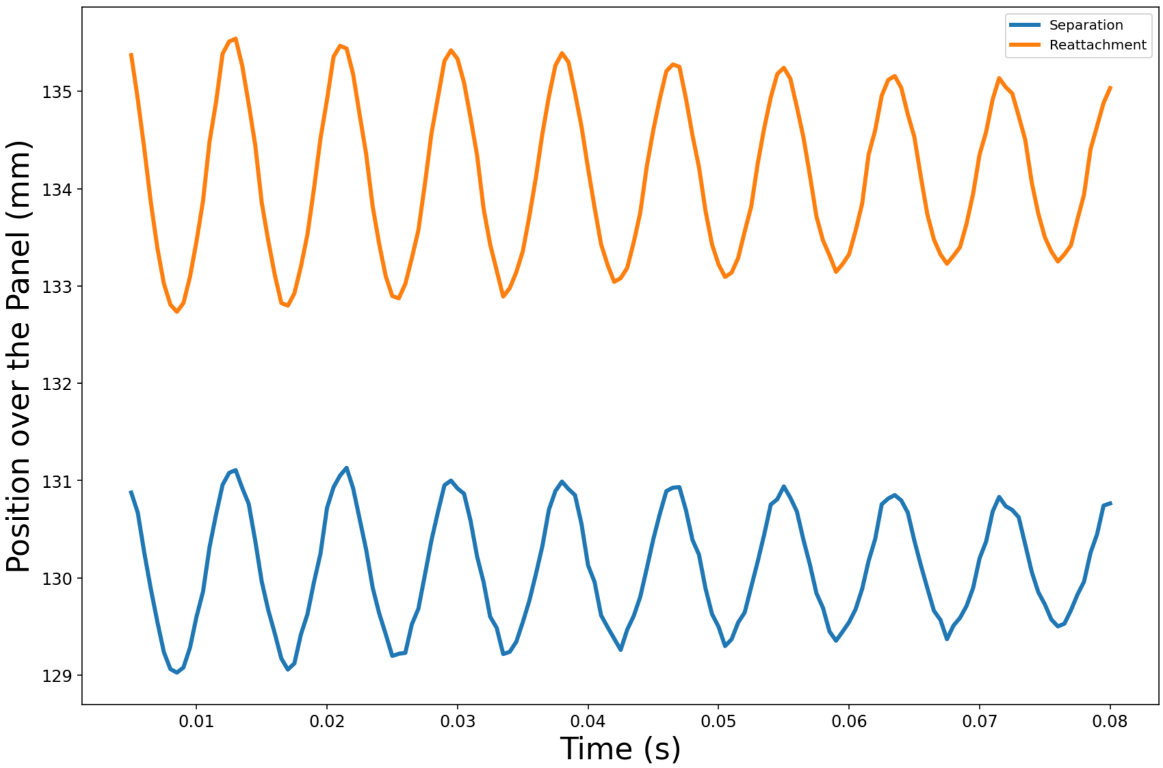

Figure 5.43: Transient movement of separation and reattachment points over time

Figure 5.43 illustrates the dynamic nature of the separation and reattachment points along the panel surface during the coupled FTSI simulation. The separation point (blue line) and reattachment point (orange line) exhibit periodic oscillatory motion synchronized with the panel vibration. The separation point oscillates between approximately 129 mm and 131 mm, while the reattachment point oscillates between 132.8 mm and 135.5 mm. This results in a separation bubble length varying roughly between 2 mm and 6 mm. Both points show a dominant frequency that closely matches the first natural mode of the panel, confirming strong fluid-structure coupling. It is observed that the reattachment point exhibits larger amplitude of oscillation compared to the separation point. This indicates that the downstream part of the separation bubble (reattachment zone) is more sensitive to panel motion. The periodic shifting of these points demonstrates how the panel deformation continuously modulates the shock-boundary layer interaction region. As the panel moves upward, the separation bubble tends to shrink or shift, and as it moves downward, the bubble enlarges or moves downstream. This dynamic behavior of the separation bubble is a key mechanism driving the strong coupling between structural deformation and aerodynamic heating observed in previous figures. The continuous movement of the reattachment point is particularly important, as it directly influences the location and magnitude of peak heat flux on the panel.

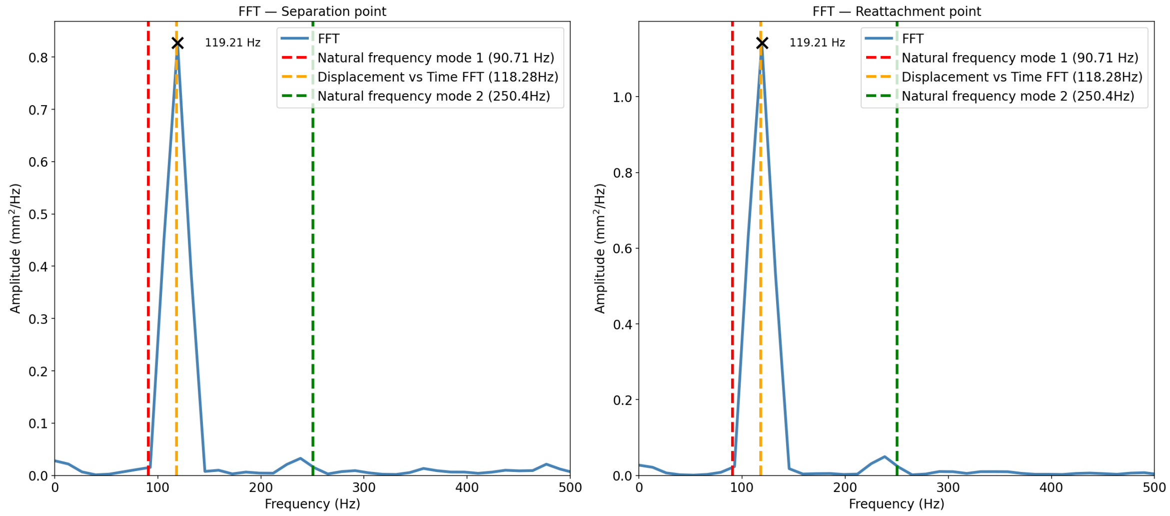

Figure 5.44: Fast Fourier Transform of the separation point and reattachment point movements compared with the natural frequencies of the plate and the dominant frequency obtained from displacement vs time.

Figure 5.44 presents the Fast Fourier Transform (FFT) analysis of the separation and reattachment points of the flow along the panel surface. The left plot shows the frequency content of the separation point movement, while the right plot corresponds to the reattachment point. Both plots reveal a dominant frequency peak at 119.21 Hz. This frequency is remarkably close to the frequency of the plate (118.28 Hz), which was observed in the FFT of the mid-point displacement time history. The strong alignment between the dominant frequency of the separation/reattachment points (119.21 Hz) and the plate's displacement frequency (118.28 Hz) indicates that the motion of the separation bubble is perfectly synchronized with the structural deflection of the panel. In other words, the separation and reattachment locations oscillate in phase with the plate's vibration. This result demonstrates a clear and strong fluid-structure coupling. The deformation of the panel directly influences the shock-boundary layer interaction, causing the separation bubble to periodically grow and shrink at the same frequency as the plate oscillation. Such synchronized behavior is highly significant in hypersonic flows, as it can lead to enhanced heat transfer fluctuations and potential aero-thermo-elastic instabilities.

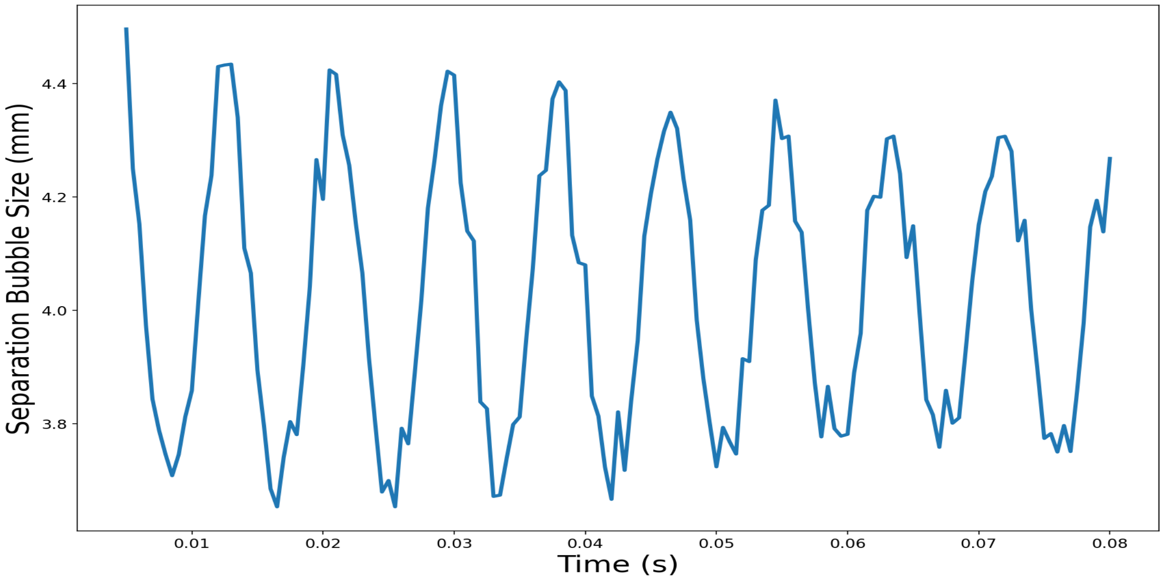

Figure 5.45: Time variation of the size of the recirculation region(Transient Nature of Separation bubble)

Figure 5.45 shows the variation of the separation bubble size over the time due to the fluctuation of the plate. This plot shows that the size of the bubble changes from ≈4.5 mm at the normal position of the plate to ≈3.7 mm at the fully deflected position.

5.2.2.6 Comparison of Inviscid and Viscous FSI

In Figure 5.46, the displacement at the mid-point of the plot is compared for both viscous and inviscid FTSI for panel thickness of 5 mm. The peak displacement at the mid-point of the panel for viscous simulation is differed by 20.9 %. As seen from Figure 5.46, the deformation of the panel is damped for viscous but not damping for inviscid simulation.

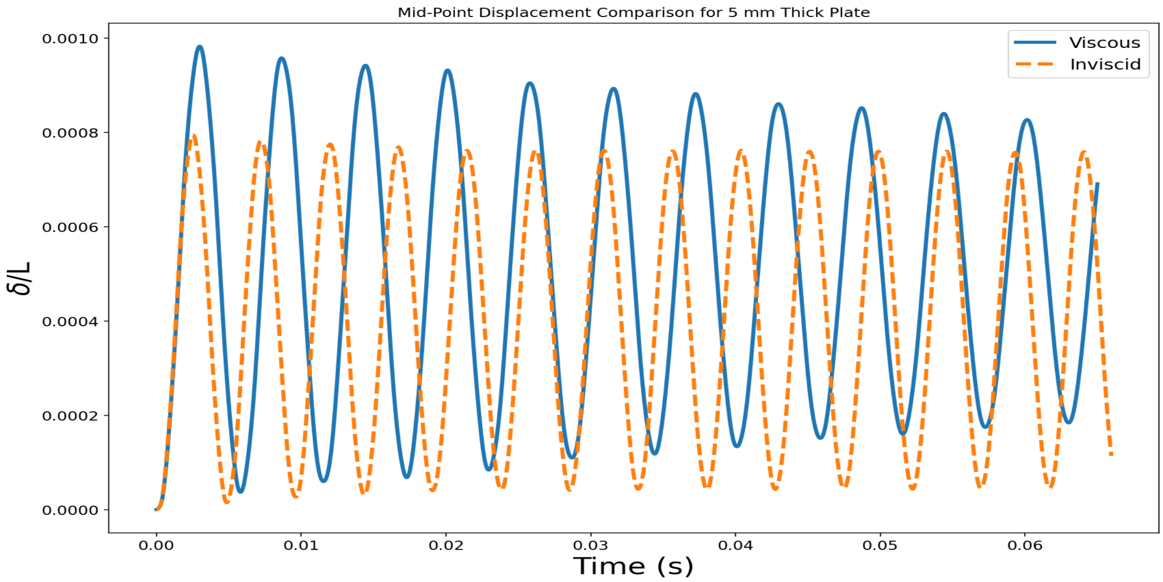

Figure 5.46: Comparison of the displacement of the mid-point of the panel for Viscous FTSI and Inviscid FSI

5.3 Low Fidelity Modeling(LFM)

The Low Fidelity Model is a quick and cheaper way to get a reasonable idea of how the panel behaves, without the time and resource demands that come with running full CFD simulations. Thus, making it particularly useful.Many different conditions can easily be tested or get early estimates during the design phase. It uses analytical tools like shock expansion theory, piston theory, and the euler-bernoulli beam model to approximate the key aerodynamic and structural behaviors. This model doesnot need mesh or long waiting hours for a solver to converge. The downside of this model is it simply cannot reproduce what happens when viscosity, flow separation, or shock boundary layer interactions come into play.Which are exactly the kinds of effects that matter most in hypersonic flight.

5.3.1 Piston Theory

This section presents the dynamic response of the clamped panel through the Low Fidelity Model, where the shock expansion theory is first used to determine how the pressure is distributed across the plate by dividing it into three distinct aerodynamic regions. As the panel begins to deform under this loading, piston theory steps in at each time step to recalculate the aerodynamic pressure based on how much the panel has tilted, while the Euler Bernoulli beam model handles the structural side of things accounting for how the panel heats up, loses stiffness, and vibrates over time. To make sense of the results, the midpoint displacement is tracked throughout the simulation since it is where the panel deflects the most, and an FFT is applied to reveal the dominant vibration frequency and show how much the fluid-structure interaction has shifted it away from the panel's natural frequency.

5.3.1.1 Midpoint Displacement Analysis

The non dimensionalized midpoint displacement ($\frac{\delta}{L}$) versus time for the 3 mm thick panel is presented in Figure 5.47.

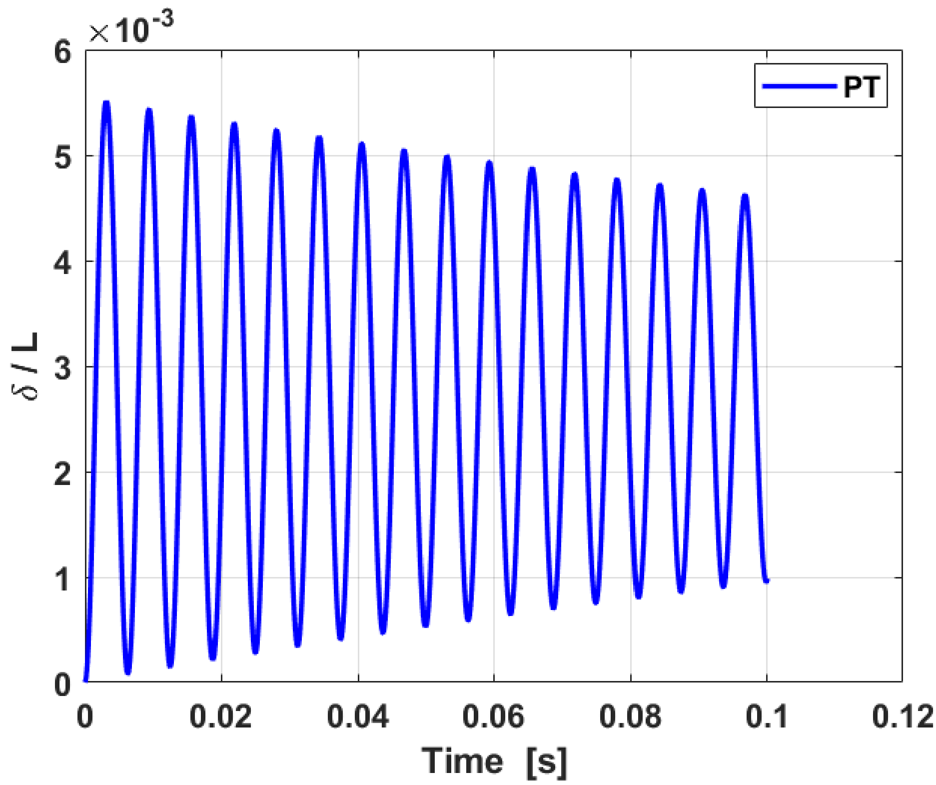

Figure 5.47: Mid-Point Displacement(PT)

An under damped vibration is clearly shown in the time history of the panel displacement over a duration of 0.1 s. This behavior is observed because vibrational energy is gradually lost by the panel over time. An initial peak displacement is observed at 0.0055, which is reduced to 0.0045 at the end of the 0.1 s interval. The influence of damping on the movement of the system is clearly indicated by this trend.From figure 5.47, it can be seen that the oscillation is not centered on the zero baseline. Instead, a certain offset is observed throughout the run. This shift suggests that the plate not only vibrates but is also held in a slightly deformed state by a constant underlying load or fluid pressure.

5.3.1.2 Fast Fourier Transform

In the Fast Fourier Transform plot shown in Figure 5.32, a dominant peak is observed at 92.5 Hz. This frequency is found to be in close agreement with the first natural mode of the plate, identified in 90.7 Hz given by dotted line. The frequency of the displacement is differed from 1st mode natural frequency of the plate by 1.97%. This suggests that mid point displacement is governed by its natural frequency.

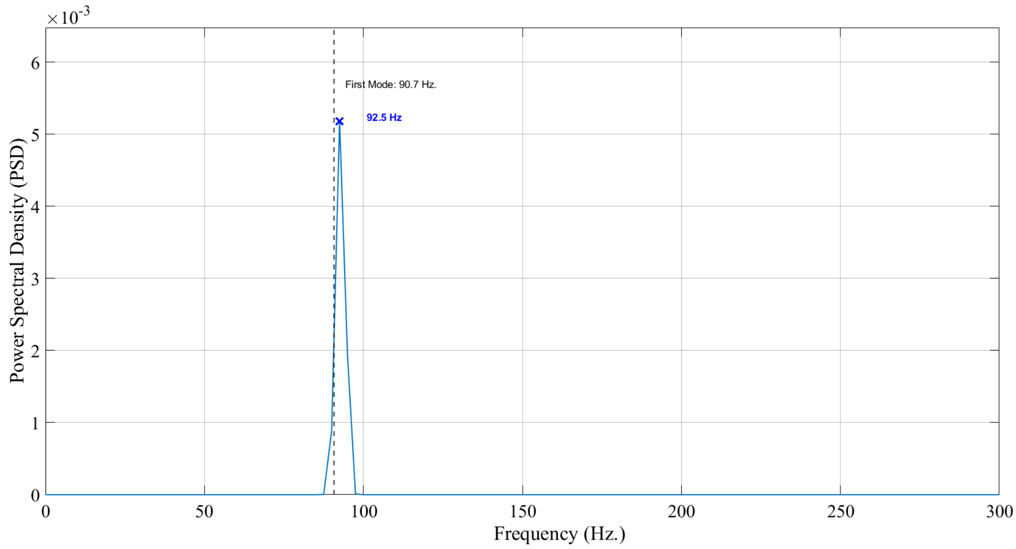

Figure 5.48: PSD of Mid-Point Displacement(PT)

Figure 5.49 illustrates how the panel deflects transversely at different points in time, starting from rest and progressing through to the end of the simulation. Both ends stay firmly at zero displacement throughout, which is exactly what we would expect from a clamped-clamped panel, and the largest deflection consistently occurs around the middle of the panel. Looking at the curves from t=10 % through to t=final, it is clear that the panel bends progressively deeper over time, eventually reaching a peak downward deflection of around -5.5×10^3 m at the center. This gradual buildup in deformation reflects how the panel responds and accumulates displacement under the aerodynamic pressure loading acting on it.

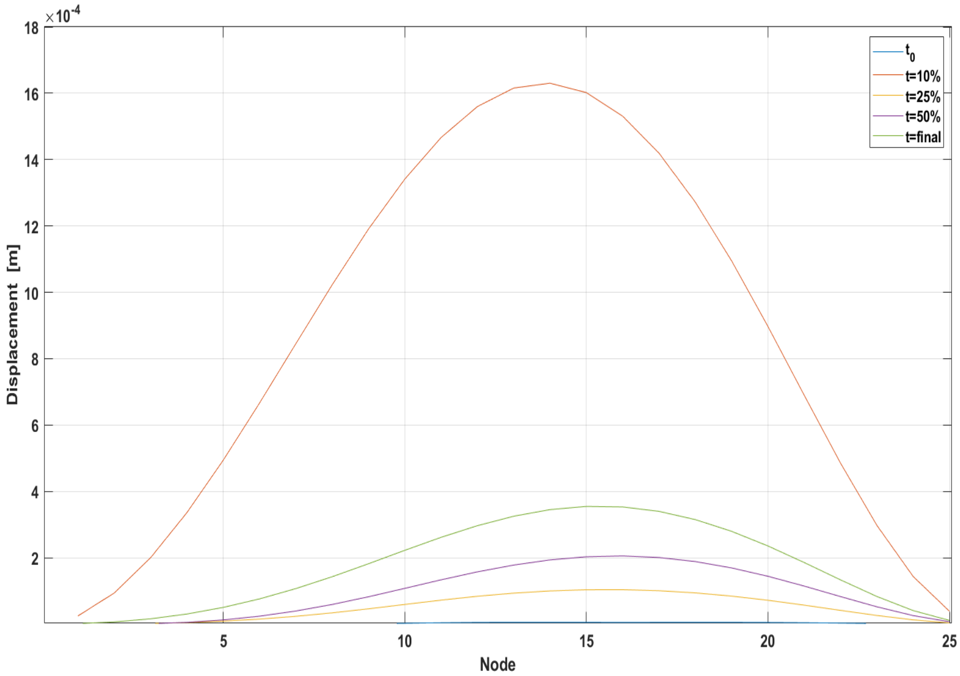

Figure 5.49: Plate State at various time period

5.3.2 CFD-Enriched Piston Theory

5.3.2.1 Displacement Based Analysis

Figure 5.50 shows the time history of the normalized mid point displacement ($\frac{\delta}{L}$) of the plate across 100 ms. The plate oscillates in a fairly regular pattern, with peak normalized displacement sitting at around 0.0048. The peak amplitude does appear to drop off gradually over time, pointing towards some degree of aerodynamic damping on the structure.However, a gradual reduction in peak amplitude is observable over time, particularly in the later stages of the simulation, which is indicative of aerodynamic damping progressively dissipating the structural oscillation energy. This damping effect highlights the role of fluid structure coupling in moderating the panel's dynamic response, as the interplay between the evolving flow field and structural deformation acts to attenuate displacement amplitudes over time

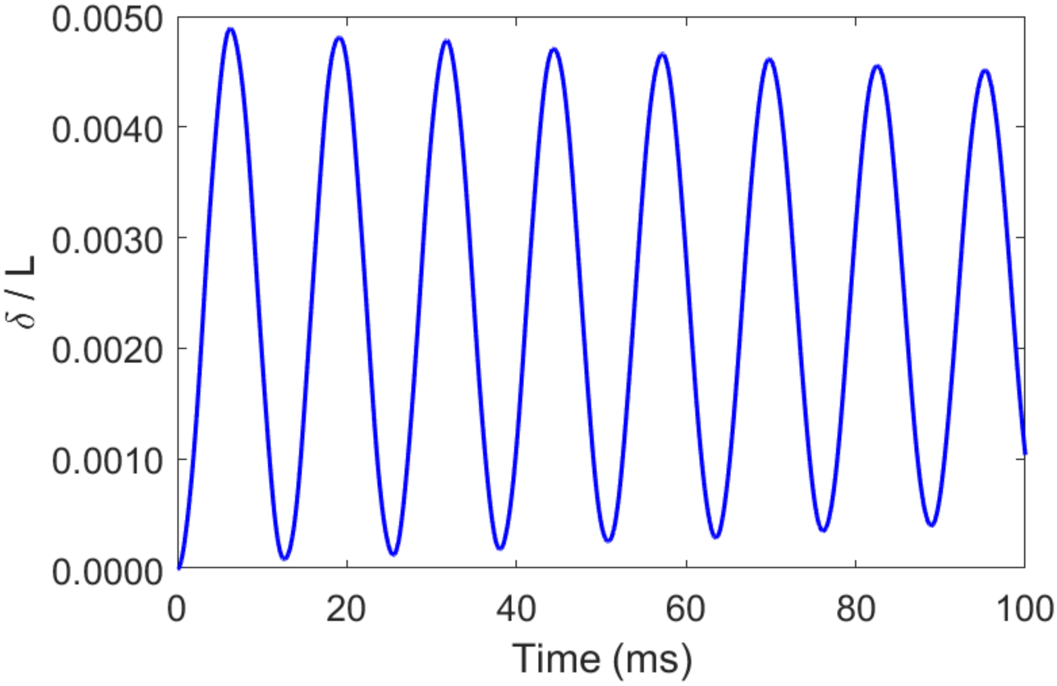

Figure 5.50: Mid Point Displacement (CFD Enriched PT)

5.3.2.2 Mid Point Pressure Measurement // Figure 5.51 presents the peak pressure history on the plate over 100 ms. The pressure keeps oscillating in a reasonably consistent manner, sitting between about 4225 Pa on the lower end and close to 4423 Pa on the upper end, putting the total pressure swing at somewhere around 200 Pa. There is a slight settling tendency in the oscillation amplitude as time progresses, where the first few cycles tend to hit somewhat higher peaks before things even out toward the latter half of the record.This is not dramatic, but it is consistent with the idea that the coupled system is still adjusting in the opening milliseconds before the flow and structural response lock into a more stable rhythm. By the latter half of the simulation, the oscillations look considerably more uniform, suggesting the system has largely found its equilibrium and the pressure response is now tracking the panel motion in a more settled and predictable way.

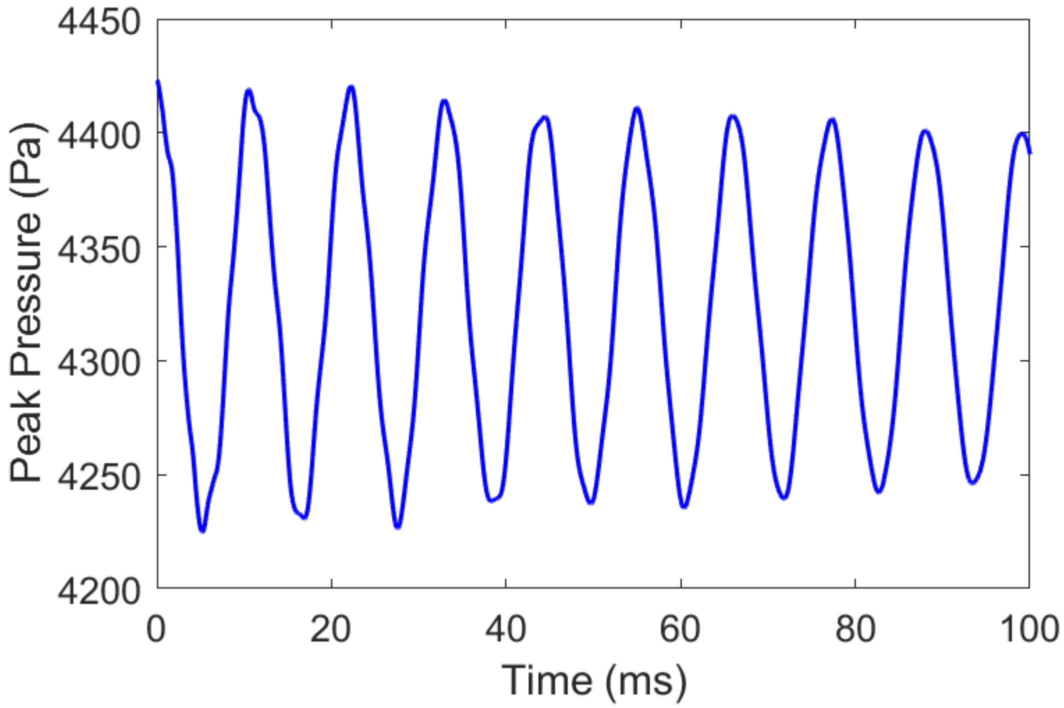

Figure 5.51: Peak Pressure Evolution with Time(CFD Enriched PT)

5.4 Comparison between LFM and HFM

Figure 5.52 shows the time history of the non-dimensional mid-point displacement (δ/L) of the panel for three different modeling approaches: Low Fidelity Model (PT-Piston Theory), High Fidelity Model (HFM-Full FTSI), and CFD Enriched Piston Theory.

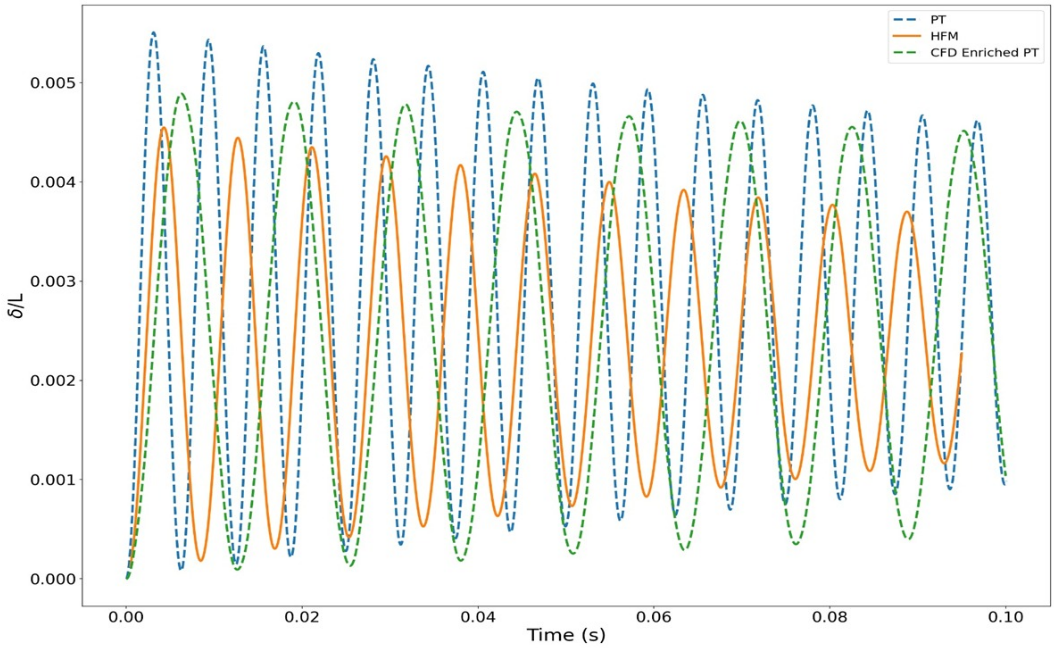

Figure 5.52: Mid-Point displacement comparison for 3 mm thick plate

The plot revealed several important characteristics of the panel response under shock impingement. A periodic oscillatory motion of the panel was predicted by all three models, confirming the presence of sustained aeroelastic vibrations. Among them, the HFM, represented by the solid orange line, was observed to exhibit the most physically consistent and balanced response, as both the oscillation amplitude and the gradual decay due to damping over time were accurately captured. In contrast, the CFD Enriched Piston Theory (blue dashed line) was found to show slightly higher frequency oscillations compared to the HFM and to moderately overpredict the displacement amplitude during the initial cycles. The classical Piston Theory (PT), represented by the green dashed line, was observed to predict the highest displacement amplitudes among the three approaches. Although the general oscillatory behavior was captured, the peak displacements were significantly overestimated, particularly during the early stages of the simulation. A notable observation was that, despite differences in amplitude, the frequency of oscillation remained nearly similar across all three models. This indicated that the dominant oscillation frequency was primarily governed by the structural properties of the panel rather than the aerodynamic modeling approach. The trade-off between computational cost and accuracy across different fidelity levels was highlighted by this comparison. The PT was found to offer high computational efficiency but at the expense of accuracy in amplitude prediction. The High Fidelity Model (HFM) was observed to provide the most reliable results by capturing the complex fluid–thermal–structure interactions. The CFD Enriched Piston Theory was identified as an intermediate approach, offering improved accuracy over classical piston theory while remaining less computationally demanding than the full high fidelity simulation. These results demonstrated that as modeling fidelity increased, more damped and physically realistic predictions of panel response were obtained, which are essential for accurate assessment of aerothermoelastic behavior in hypersonic environments.

CHAPTER SIX: LIMITATIONS, WORK SCHEDULING AND BUDGET ANALYSIS

6.1 Limitations

Although the project was carefully planned and executed, the study was limited by computational resources and simulation time. The simulation was conducted only up to 20 ms(for thermal effect), which restricted complete visualization of the thermal response and maximum temperature rise of the panel.

6.2 Work Scheduling

The work division for the project is done by separating the tasks into parts, and the estimated work scheduling is provided in Table 6.13 and gantt chart in Figure 7.60

Table 6.13: Work Schedule

Task	**Start Date**	**End Date**	**Duration (days)**
Preliminary Research	01-May-2025	15-Jun-2025	46
Literature Review	15-Jun-2025	25-Mar-2026	284
Mathematical Modeling	15-Jun-2025	15-Aug-2025	62
Geometry and Meshing	15-Jul-2025	15-Sep-2025	62
Simulation Execution	01-Aug-2025	31-Oct-2025	92
Coupled FTSI Simulation	01-Dec-2025	15-Mar-2026	105
Post Processing	01-Aug-2025	25-Mar-2026	237
Documentation and Reporting	1-May-2025	26-Mar-2026	330

6.3 Gantt Chart

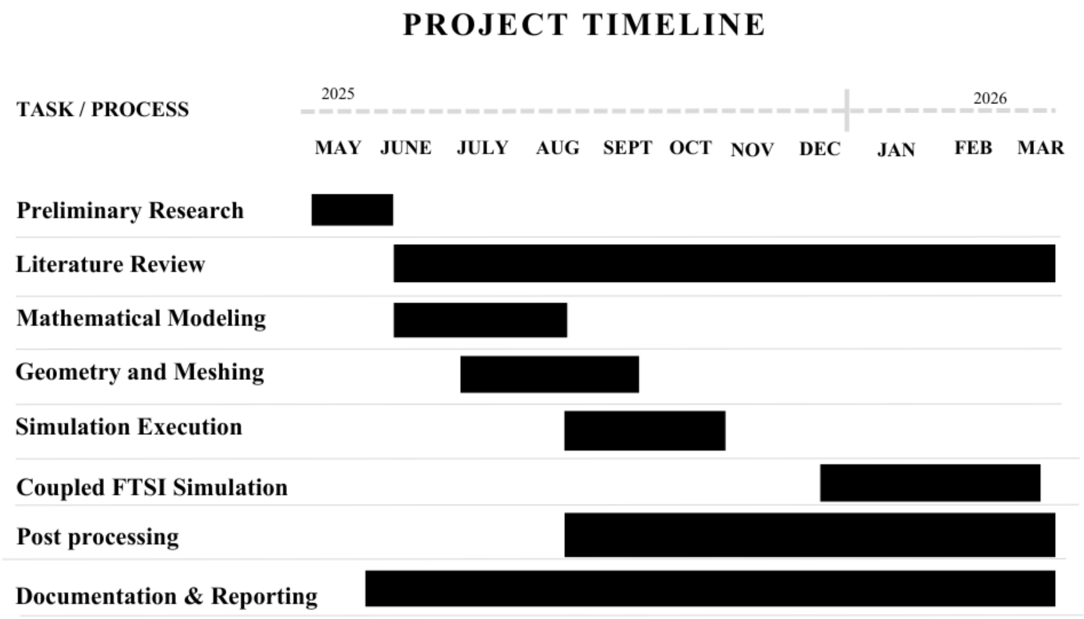

Figure 6.53: Project Gantt Chart

6.4 Budget Analysis

The computational cost is estimated using Amazon Web Services (CFD Direct from the Cloud) for a virtual machine configuration (c5.4xlarge) with 16 CPU cores and 32 GB RAM, costing approximately Rs.130 per hour [7]. A total simulation time of around 288 hours (about 12 days) was considered, which worth is NRs. 37440 for completion of total simulation[6.14]. Total budget estimated after including documentation cost is NRs.42,440[6.15]. Since this is a final year academic project and all resources are provided by the campus, the entire budget is internal and no external funding is required.

Table 6.14: Computational Cost

S.N.	Model	Time (Hours/min)	Cost (Rs.)
1	Inviscid FTSI	60 hr	7,800
2	Viscous FTSI 12 mm	18 hr	2,340
3	Viscous FTSI 5 mm	60 hr	7,800
4	Viscous FTSI 3 mm	82 hr	10,660
5	Viscous (laminar) FTSI	20 hr	2600
6	Supersonic FTSI	48 hr	6,240
	Total	288	37,440

Table 6.15: Budget Estimation

S.N.	Name of Particulars	Cost (Rs.)
1	Documentation	5,000
2	Computational Cost	37,440
	Total	42,440

CHAPTER 7: CONCLUSION AND SCOPE FOR FUTURE ENHANCEMENT

7.1 Conclusion

This study presented a comprehensive numerical investigation of hypersonic Fluid-Thermal-Structural Interaction (FTSI) on a flexible metallic panel under shock impingement. The RC-19 supersonic clamped thin panel case was selected as the benchmark configuration. The supersonic case was first successfully validated against available experimental and numerical data, demonstrating good agreement in flow features, pressure distribution, and panel response. Building upon this validated framework, the study was systematically extended to hypersonic conditions to explore stronger aero-thermo-elastic coupling effects. A partitioned coupling approach was employed, combining OpenFOAM (rhoCentralFoam) for the compressible turbulent flow field, CalculiX for the thermo-elastic structural response, and preCICE as the coupling interface. A parametric study was conducted by progressively reducing the plate thickness from 12 mm to 5 mm and finally to 3 mm. Results showed that decreasing the plate thickness significantly amplifies the structural deformation - from a negligible maximum displacement of approximately 34 μm for 12 mm plate, 0.38 mm for 5mm plate and 1.75 mm for 3 mm plate. Key observations include a strong frequency synchronization between the panel vibration and the motion of the separation and reattachment points (dominant frequency $\approx$ 119 Hz, closely matching the plate's displacement vs time frequency). This synchronized behavior led to substantial changes in the separation bubble dynamics, shock impingement location, and localized heat flux. The study clearly demonstrated that larger panel deflections enhance aero-thermal feedback, resulting in noticeable variations in wall heat flux and pressure loading. The present work successfully captured the complex nonlinear interactions between aerodynamic forces, structural deformation, and aerodynamic heating in a hypersonic environment. It highlights the importance of fully coupled FTSI simulations for accurate prediction of panel behaviour under severe shock impingement conditions. Future research should focus on three-dimensional simulations, incorporation of high temperature material degradation models, and detailed investigation of aero-thermo-elastic instabilities such as panel flutter. Experimental validation in hypersonic facilities would further strengthen the reliability of the numerical predictions. In conclusion, this study provides valuable insights into the coupled physics of hypersonic panel flow and demonstrates the effectiveness of the OpenFOAM–CalculiX–preCICE framework for high-fidelity aerothermoelastic simulations.

7.2 Scope for Future Enhancement

i. To extend the study to 3D-simulation for more realistic flow and structural behavior, although the present two-dimensional approach was considered sufficient based on the dominant coupling effects and target deformation characteristics.

ii. To include real gas behavior, reactions, and dissociation.

iii. To incorporate fully temperature-dependent thermal material properties, including thermal conductivity, specific heat, and thermal expansion coefficients, for improved thermo-structural accuracy.

iv. To apply optimization techniques, including surrogate modeling or machine learning, for efficient design exploration under extreme conditions.

REFERENCES

[1] J. D. Anderson, *Hypersonic and High-Temperature Gas Dynamics*, 2nd ed. AIAA, 2020.

[2] B. Stanford and P. Chwalowski, "Nasa larc contribution to the aepw high speed working group test case — rc 19," Presentation at NESC Academy Workshop AePW4, 2024. [Online]. Available: https://nescacademy.nasa.gov/workshops/AePW4/public/wg/high_speed

[3] E. H. Dowell, *A Modern Course in Aeroelasticity*, 6th ed. Springer, 2022.

[4] N. Poudel, S. Sahani, S. Pudasaini, and S. Bhattrai, "Numerical study of hypersonic fluid structure interaction on a cantilevered plate with shock impingement," in *AIAA AVIATION Forum and ASCEND*, 2024.

[5] T. J. Whalen *et al.*, "Hypersonic fluid structure interactions in compression corner shock wave boundary layer interaction," *AIAA Journal*, vol. 58, no. 9, pp. 4090–4105, 2020.

[6] J. C. Lin and R. D. Mehta, "Shock boundary layer interactions," NASA, Technical Memorandum NASA TM-108790, 1995.

[7] D. L. Whitmore and M. A. Holden, "Thermal response and structural performance of tps materials in hypersonic flow," NASA, Technical Report NASA/TP-2008-214341, 2008.

[8] H. Ganti, L. Bravo, A. Ghoshal, and P. Khare, "Fluid structure interactions of flexible panels in hypersonic flow," in *AIAA AVIATION Forum*, 2025, submitted.

[9] S. Gewali, A. Pandey, N. Poudel, S. Adhikari, and S. Bhattrai, "Influence of aerothermoelasticity on performance of oblique detonation wave engines," in *AIAA SciTech Forum*, 2025.

[10] D. R. Carlson and A. M. Sartor, "Aerothermoelastic simulation of a flexible panel in hypersonic flow," in *AIAA SciTech Forum*, 2017, p. 1010.

[11] D. D. Knight, "Theoretical and experimental study of hypersonic boundary layer transition," *Progress in Aerospace Sciences*, vol. 34, no. 6, pp. 231–307, 1998.

[12] P. B. Vasconcelos, L. P. McQuellin, T. Krishna, and A. Neely, "Experimental study of hypersonic fluid structure interactions on an inclined clamped panel," in *ASCEND*, 2021, p. 4232.

[13] E. H. Dowell and D. B. Bliss, “New look at unsteady supersonic potential flow aerodynamics and piston theory,” *AIAA Journal*, vol. 51, no. 9, pp. 2278–2281, 2013.

[14] T. Salmon, C. Altmann, A. Bungartz, and B. Uekermann, “High fidelity coupled fsi simulation of vortex induced vibration using precice,” in *Computational Methods in Applied Sciences*. Springer, 2021, vol. 53, pp. 317–340.

[15] S. Willems, A. Gülhan, and B. Esser, “Shock induced fluid structure interaction on a flexible wall in supersonic turbulent flow,” in *EUCASS*, 2011.

[16] G. Currao, A. Neely, C. Kennell, S. Gai, and D. Buttsworth, “Hypersonic fluid–structure interaction on a cantilevered plate with shock impingement,” *AIAA Journal*, vol. 57, 2019.

[17] D. Daub, S. Willems, and A. Gülhan, “Experiments on aerothermoelastic fluid-structure interaction in hypersonic flow,” *Journal of Sound and Vibration*, vol. 531, 2022.

[18] D. Huang and P. P. Friedmann, “An aerothermoelastic analysis framework with reduced-order modeling applied to composite panels in hypersonic flows,” *Journal of Fluids and Structures*, vol. 94, p. 102927, 2020.

[19] M. Freydin and E. H. Dowell, “Fully coupled nonlinear aerothermoelastic computational model of a plate in hypersonic flow,” *AIAA Journal*, vol. 59, no. 7, pp. 2725–2736, 2021.

[20] J. D. Anderson, *Hypersonic and High Temperature Gas Dynamics*. AIAA, 2000.

[21] R. Neumann, “Special topics in hypersonic flow, aerodynamic problems of hypersonic vehicles,” AGARD, Tech. Rep. LS-42-Vol.1, Jul. 1972.

[22] “X-51A waverider,” https://www.af.mil/About-Us/Fact-Sheets/Display/Article/104467/x-51a-waverider/, 2023, [Accessed: 23 February 2023].

[23] H. Babinsky and J. K. Harvey, *Shock Wave-Boundary-Layer Interactions*. Cambridge University Press, 2011, vol. 32.

[24] M. S. Holden, “Shock wave-turbulent boundary layer interaction in hypersonic flow,” in *10th Aerospace Sciences Meeting*, 1977, p. 74.

[25] J. J. McNamara, A. R. Crowell, P. P. Friedmann, B. Glaz, and A. Gogulapati, “Approximate modeling of unsteady aerodynamics for hypersonic aeroelasticity,” *Journal of Aircraft*, vol. 47, no. 6, pp. 1932–1945, 2010.

[26] J. J. McNamara and P. P. Friedmann, "Aeroelastic and aerothermoelastic analysis in hypersonic flow: Past, present, and future," *AIAA Journal*, vol. 49, no. 6, pp. 1089–1122, 2011.

[27] G. Currao, "Experimental study of hypersonic fluid structure interaction with shock impingement on a cantilevered plate," Ph.D. dissertation, UNSW Sydney, 2018.

[28] H. Babinsky and J. K. Harvey, *Shock Wave-Boundary-Layer Interactions*, ser. Cambridge Aerospace Series. Cambridge University Press, 2011.

[29] N. Poudel, S. Sahani, S. Pudasaini, S. Bhattrai, K. Darlami, and K. M. Talluru, "Numerical study of hypersonic fluid-structure interaction on a cantilevered plate with shock impingement using low and high-fidelity numerical methods," *AIAA AVIATION Forum*, July 2024.

[30] S. Scholl, B. Janssens, and T. Verstraete, "Stability of static conjugate heat transfer coupling approaches using robin interface conditions," *Computers & Fluids*, vol. 172, pp. 209–225, 2018.

[31] H. K. Versteeg and W. Malalasekera, *An Introduction to Computational Fluid Dynamics: The Finite Volume Method*, 2nd ed. Pearson Education, 2007.

[32] A. Neely, G. Currao, and L. P. McQuellin, "Using radiative heating to perform fluid thermal structural interaction experiments in a short duration hypersonic wind tunnel," in *21st Australasian Fluid Mechanics Conference*, Adelaide, Australia, December 2018.

APPENDIX

7.3 Hypersonic

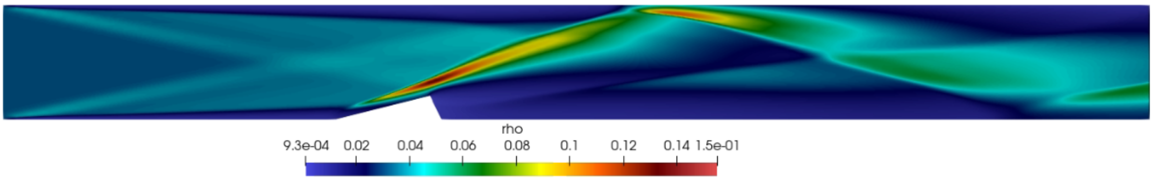

Figure 7.54: Density Contour

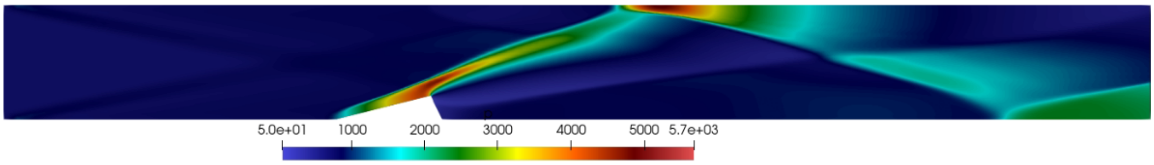

Figure 7.55: Pressure Contour

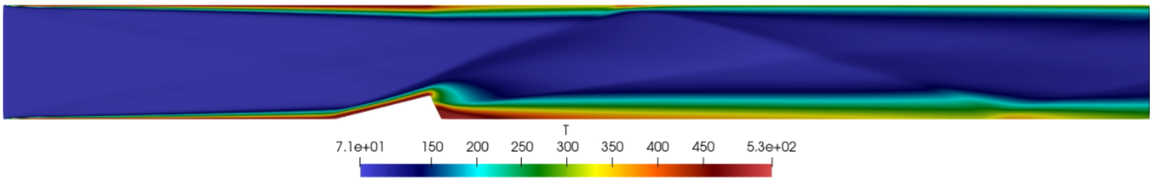

Figure 7.56: Temperature Contour

7.4 Supersonic Contours

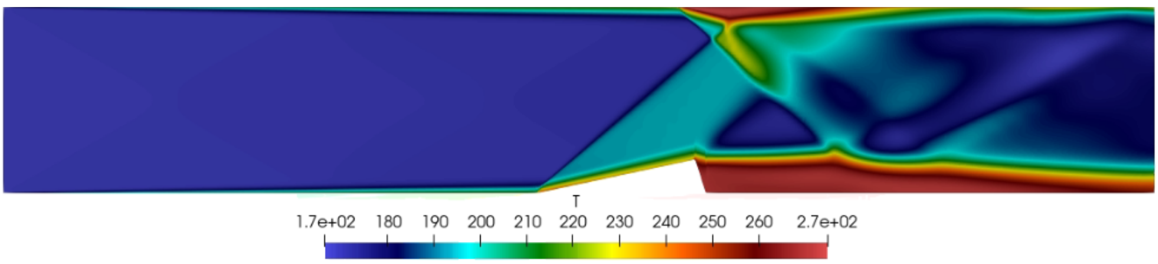

Figure 7.57: Temperature Contour

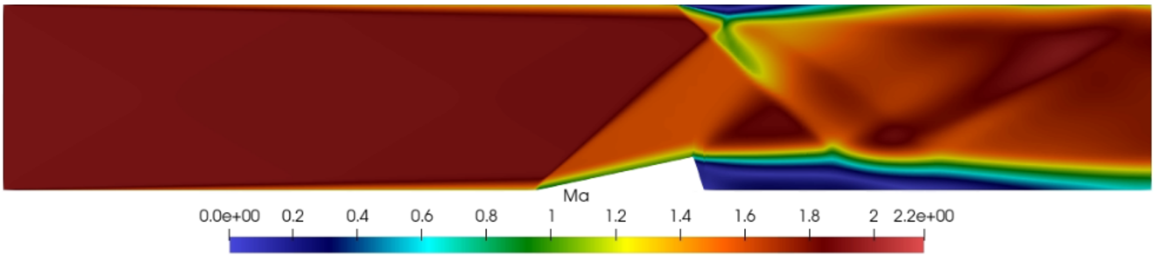

Figure 7.58: Mach Contour

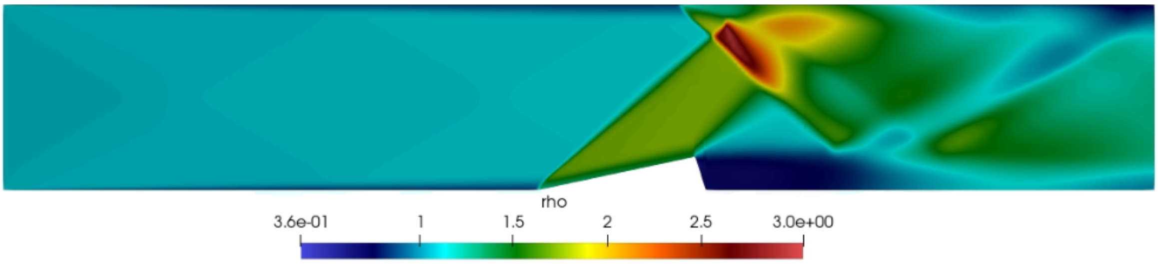

Figure 7.59: Density Contour

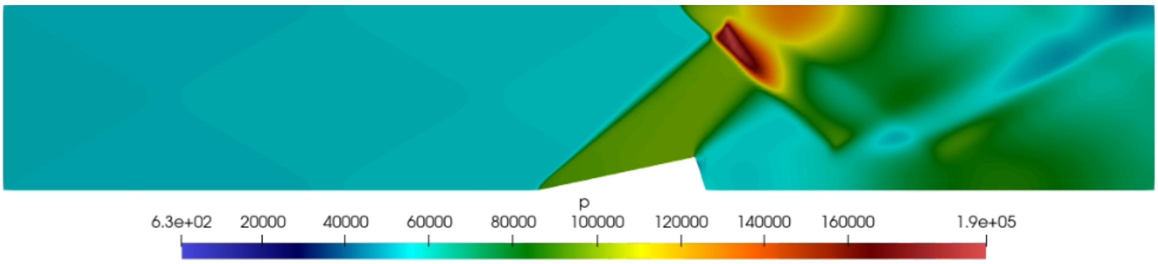

Figure 7.60: Pressure Contour